How Non-Uniform Temperatures Influence the Performance and Ageing of Lithium-Ion Batteries

Zur Erlangung des akademischen Grades einer
Doktorin der Ingenieurwissenschaften (Dr.-Ing.)

von der KIT-Fakultät für Chemieingenieurwesen und Verfahrenstechnik
des Karlsruher Instituts für Technologie (KIT)
genehmigte

DISSERTATION

von
M.Sc. Sabine Paarmann
aus Stuttgart

Tag der mündlichen Prüfung: 07.09.2021

Erstgutachter: Prof. Dr.-Ing. Thomas Wetzel
Zweitgutachterin: Prof. Dr.-Ing. Ulrike Krewer

Kurzfassung

Lithium-Ionen Batterien (LIB) finden aufgrund ihrer Vorteile hinsichtlich Energie- und Leistungsdichte sowie ihrer Zuverlässigkeit verbreitete Anwendung als elektrochemische Energiespeicher. Sie spielen im Rahmen des Klimawandels und der dadurch bedingten Energiewende eine zentrale Rolle in der Elektrifizierung der Mobilität.

In LIB laufen eine Vielzahl komplexer multi-physikalischer Prozesse und elektrochemischer Reaktionen zeitgleich und in enger Wechselwirkung miteinander ab. Neben vielen anderen Faktoren hat die Temperatur wesentlichen Einfluss auf diese und folglich auf das resultierende Leistungs- und Alterungsverhalten der Batteriezelle. Während des Betriebs einer Zelle liegt ihr „Wohlfühlbereich“ bei etwa 25 °C. Bei höheren Temperaturen steigt zwar die Leistungsfähigkeit, aber es intensivieren sich auch parasitäre Nebenreaktionen und die Degradation der Zelle. Bei niedrigeren Temperaturen hingegen verlangsamen sich die Prozesse, es kommt zu erhöhten Überspannungen und die Leistungsfähigkeit nimmt ab. Hinzu kommt die Gefahr von Lithium-Plating, was ebenfalls zu einer beschleunigten Alterung führt. Durch die im Betrieb ablaufenden Verlustprozesse kommt es zusätzlich zu einer Erwärmung. Um diese interne Wärmeentwicklung auszugleichen, werden bei größeren Batteriepacks Temperiersysteme eingesetzt. Diese wiederum induzieren einen Temperaturgradienten sowohl im Modul als auch in jeder einzelnen Batteriezelle.

Wie sich solche Temperaturgradienten auf das elektrochemische Verhalten auswirken, wird im Rahmen dieser Dissertation zunächst integral anhand von Spannungsverläufen und elektrochemischen Impedanzspektren untersucht. Bisher wurden Impedanzspektren an Zellen mit aufgeprägtem Temperaturgradienten mit dem Ziel aufgenommen, diese Methode als schnelles Diagnosewerkzeug für Batteriemanagementsysteme zu nutzen. Die Ergebnisse zeigen bei Temperaturgradienten auf niedrigem Temperaturniveau eine Verschiebung

des Zellverhaltens in Richtung des Verhaltens der Zelle bei einer höheren Temperatur. Damit hat der wärmere Teil gegenüber dem kälteren Teil der Zelle einen etwas größeren Einfluss auf das Gesamtverhalten. Bei höheren Temperaturen und höheren Strömen zeigt sich dieses Verhalten nicht, da die Stromdichte lokal ähnlich ist bzw. auch im Bereich hoher Temperaturen Überspannugen auftreten und die Stromdichte begrenzen. Der Einfluss von Temperaturgradienten auf das integrale Batterieverhalten ist damit weniger stark ausgeprägt als die weit verbreitete Restriktion bezüglich des maximalen Temperaturunterschiedes von 5 K vermuten lässt. Weiterhin werden diese Zusammenhänge über die temperaturabhängige Stromverteilung in der Zelle vertiefend analysiert. Um diese zuverlässig zu quantifizieren, wird ein neuartiger Versuchsablauf entwickelt und implementiert. Er bietet Vorteile gegenüber bisher durchgeführten Methoden, welche auf instrumentierten Multitabzellen oder auf Parallelverschaltung mehrerer Zellen basieren. Die entwickelte Methode ermöglicht die Messung der Stromverteilung an einer Einzelzelle und ist damit unabhängig von Variationen zwischen den Zellen und dem Messaufbau. Validiert wird diese mit einer parallelen Verschaltung von Zellen desselben Zelltyps mit individueller Temperierung.

Zusätzlich wird das Alterungsverhalten unter definierten thermischen Inhomogenitäten untersucht. Neben dem Kapazitätsverlust und Impedanzanstieg mit zunehmender Zyklenzahl wird die Temperaturabhängigkeit über eine äquivalente Alterungstemperatur quantifiziert und die auftretenden Alterungsmodi mit Hilfe der „Differential Voltage Analysis“ betrachtet. Um die Alterungsursachen und die lokalen Mechanismen zu identifizieren, werden ausgewählte repräsentative Zellen geöffnet und die Elektroden individuell über Halbzellmessungen charakterisiert. Zusätzlich wird die Elektrodendicke gemessen, Bilder der Oberfläche mit dem Rasterelektronenmikroskop aufgenommen und Messungen mittels Röntgenphotoelektronenspektroskopie durchgeführt. Die Kristallstruktur wird über Röntgenbeugung analysiert und die Konzentration der Übergangsmetalle, Lithium und Phosphor an der Anode mit Hilfe der optischen Emissionsspektrometrie mit induktiv gekoppeltem Plasma gemessen. Die auftretenden Veränderungen werden anschließend mit den Randbedingungen korreliert. Die Messungen zeigen eine starke Inhomogenität der Alterungs-

mechanismen, während das integrale Alterungsverhalten durch Temperaturgradienten nicht signifikant verändert wird. Zeitliche Temperaturänderungen hingegen induzieren eine ausgeprägte Alterung.

Mit diesen Ergebnissen ergibt sich ein umfassendes Bild, wie sich thermische Inhomogenitäten auf die Batteriezelle, ihr elektrochemisches Verhalten und die Alterung auswirken.

Abstract

Lithium-ion batteries (LIB) are widely used as electrochemical energy storage devices due to their advantages in terms of energy and power density as well as their reliability. They play a central role in the electrification of mobility in the context of climate change and the "Energiewende".

In LIB, numerous complex multi-physical processes and electrochemical reactions occur simultaneously and in close interaction. Among many other factors, temperature has a significant influence on these processes and consequently on the resulting performance and the cells ageing behaviour. During the operation of a cell, its "comfort zone" is around 25 °C. At higher temperatures, the performance capability increases, but parasitic side reactions also intensify. At lower temperatures, on the other hand, processes slow down, overvoltages increase and thus, performance decreases. Additionally, the risk of lithium plating is higher, which also leads to accelerated ageing. Besides temperature-dependent ageing effects, heat is generated during operation due to dissipation. For larger battery packs, temperature control systems are implemented to compensate for this internal heat generation. These, in turn, induce a temperature gradient both in the module and in each battery cell.

The effect of such temperature gradients on electrochemical behaviour is first investigated based on voltage characteristics and electrochemical impedance spectra. Up to now, impedance spectra with imposed temperature gradients have been measured to develop a fast diagnostic tool in applications without actually exploring the origin of the effects. The results show that temperature gradients at a low temperature level shift the cell behaviour towards the cell behaviour at a higher temperature. Thus, the warmer part has a slightly larger influence on the overall behaviour than the colder part of the cell. However, this behaviour is not evident at higher temperatures and higher currents since the current density is locally similar, or overvoltages occur in the high temperature range and limit the current density there as well.

The influence of temperature gradients on the overall battery behaviour is thus less pronounced than the common restriction regarding the maximum temperature difference of 5 K would suggest. Furthermore, these relationships are analysed in more detail via the temperature-dependent current distribution in the cell. To quantify these reliably, a novel experimental procedure is developed and implemented. It is advantageous compared to existing methods based on instrumented multi-tab cells or the parallel connection of several cells. The developed method allows the measurement of the current distribution at a single cell and is therefore independent of cell-to-cell variations and the measurement set-up. It is validated with a parallel connection of cells of the same cell type with individual temperature control.

Furthermore, the ageing behaviour under defined thermal inhomogeneities is investigated. Besides the capacity loss and impedance increase with increasing cycle number, the temperature dependency is quantified via an equivalent ageing temperature, and the occurring degradation modes are examined applying differential methods. To identify the ageing origins and local mechanisms, selected representative cells are opened, and the electrodes are individually characterised via half-cell measurements. In addition, the electrode thickness is determined, images with a scanning electron microscope captured, and measurements of the surface chemistry are performed via X-ray photoelectron spectroscopy. X-ray diffraction analyses the crystal structure of the cathode, and the concentration of transition metals, lithium and phosphorus at the anode is measured by inductively coupled plasma atomic emission spectroscopy. The changes that occur are then correlated with the boundary conditions. These measurements reveal a strong inhomogeneity in ageing mechanisms, while the overall ageing behaviour is not significantly altered by temperature gradients. Temporal temperature changes, on the other hand, induce a distinct degradation.

With these results, a comprehensive understanding of how thermal inhomogeneities affect the battery cell, its electrochemical behaviour and ageing is obtained.

Table of Content

Symbols

Symbols

a, b, c	-	Lattice Parameters
$at.\%$	%	Atomic Concentration
Δ		Difference
E_A	eV	Activation Energy
f	Hz	Frequency
h, k, l		Miller Indices
θ	°	Diffraction Angle
I	A	Current
L	M	Length
λ	nm	Wavelength
Q	Ah	Amount of Charge
$\dot{Q}$	W	Heat Generation
R	Ω	Resistance
$\tilde{R}$	$Jmol^{-1}K^{-1}$	Universal Gas Constant
R_{col}	Ω	Temperature-dependent resistance of the current collectors
R^2		Coefficient of Determination
t	s	Time
T	°C or K	Temperature
U	V	Voltage
V	m^3	Volume
φ	°	Phase Change
wt.%	%	Weight Concentration
x	-	Degree of intercalation
z	m	Thickness
Z	Ω	Impedance
Z'	Ω	Real part of the Impedance
Z''	Ω	Imaginary part of the Impedance
ω	1/s	Angular Frequency

Indices

avg	average
corr	corrected
cyc,th	thermischer Zyklus
irr	irreversible
max	maximum
min	minimum
norm	normalised
OCV	Open Circuit Voltage
ohm	Ohmic
pol	Polarisation
rev	reversible
Sim	simulated
tot	total

Abbreviations

AFM	Atomic Force Microscopy
AM	Active Material
BoL	Begin of Life
BSE	Backscattered Electrons
CC-CV	Constant Current – Constant Voltage
CT	Computer Tomography
DMC	Dimethyl carbonate
DoD	Depth of Discharge
DVA	Differential Voltage Analysis
EAT	Equivalent Ageing Temperature
EC	Ethylene carbonate
ECM	Equivalent Circuit Model
EDX	Energy-dispersive X-ray spectroscopy
EFC	Equivalent Full Cycles
EIS	Electrochemical Impedance Spectroscopy
EoL	End of Life
GUM	Guide to express the Uncertainty in Measurement
HS	Homogeneous-Stationary
HT	Homogeneous-Transient
ICA	Incremental Capacity Analysis

ICP-OES	Inductively Coupled Plasma Optical Emission Spectroscopy
IS	Inhomogeneous-Stationary
IT	Inhomogeneous-Transient
LAM	Loss of active material
LCO	Lithium Cobalt Oxide
LFP	Lithium Iron Phosphate
LIB	Lithium-Ion Battery
LLI	Loss of lithium inventory
LMO	Lithium Manganese Oxide
NCA	Lithium Nickel Cobalt Aluminum Oxide
NMC	Nickel Manganese Cobalt Oxide
NMP	n-Methyl-2-Pyrrolidone
OCV	Open Circuit Voltage
PC	Propylene carbonate
PE	Polyethylene
PP	Polypropylene
PMA	Post-mortem Analysis
PVDF	Polyvinylidene Fluoride
qOCV	quasi Open Circuit Voltage
SE	Secondary Electrons
SEI	Solid Electrolyte Interface
SEM	Scanning Electron Microscopy
SoC	State of Charge
SoH	State of Health
TVT	Institute of Thermal Process Engineering
XPS	X-ray Photoelectron Spectroscopy
XRD	X-ray Diffraction

Acknowledgement

This thesis was accomplished during my time as a research assistant at the Institute of Thermal Process Engineering (TVT) at the Karlsruhe Institute of Technology (KIT) from February 2016 till September 2021. First of all, I would like to express my gratitude to Prof. Dr.-Ing. Thomas Wetzel for the opportunity to work on this exciting topic. I appreciate his trust and confidence and enjoyed the freedom I had doing research.

I would also like to thank Prof. Dr.-Ing. Ulrike Krewer very much for providing the second review of this thesis, following along with the tight schedule, and encouraging me (unrelated to the dissertation).

For their support at TVT, I would like to thank Prof. Dr.-Ing. Matthias Kind and Dr.-Ing. Benjamin Dietrich. Many thanks go to Nicole Feger and Vanessa Gamer, who did a lot of work in the background so that everything went smooth from ordering to contract extensions and took care that all documents were filled out the right way.

I have to thank the TVT-workshop-team Stefan Böttle, Vanessa Drakeford, Stephan Fink, Lukas Halas, Max Renaud, and Michael Wachter for manufacturing parts for the experimental set-ups. Many thanks, in particular, to Sabrina Herberger, who runs the laboratory and keeps everything running smoothly and provides active support in every situation.

I would also like to express my appreciation for the willingness at KIT to cooperate and my thanks to all those who supported me with measurements and their expertise. First of all, Annette Schucker who transferred from the TVT lab to IAM-ET and was ready to perform the XRD measurements. Manfred Janzen and Rainer Mönig made it possible to take some of the SEM images in the laboratory of IAM-WBM, and Olivia Wiegand prepared the cross-sections at IAM-ESS. I thank Dr. Julia Maibach and Dr. Christian Njel for the XPS measurements and analysis and the support during the interpretation, and Elisabeth Eiche, Chantalle Kotschenreuther and Janine Wagner for the ICP-OES

measurements and the acid digestion. Additionally, I want to thank Thomas Sollich from IFG for conducting the mercury porosity and Peter Krolla for testing battery materials with AFM, although these measurements did not find their way into this thesis.

I am grateful for the energetic support of all the students I have supervised during my time at TVT: Marijan Mohr, Nicolas Kunkel, Fabian König, Marcel Nussberger, Christian Of, Lisa Giang, Jakob Technau, Simon Rihm, Simon Traub, Qijun Zhang, Laura Dreyer, Leonie Pfeifer, Stefan Höll, Lisa Cloos, David Herrmann, Ulrich Rist, Julia Spies, Raphael Mühlpfort und Kathrin Schuld.

I am thankful to have been part of the SiMET research training group as an associate. In addition to a guest stay at Warwick University with Dhammika Windanalage, conference participation, countless workshops, I have met amazing people who have enriched the doctoral period not only thematically but personally.

To the current and former colleagues at the Institute, I thank you deeply for the collaborative atmosphere, the professional and emotional support, the enriching discussions, the fun activities beyond work. I am happy about your friendship.

I want to thank my family for their love, confidence and support and all my friends who pulled me through tough times and shared wonderful moments outside work.

I especially want to thank Philipp Dechent for enriching my life.

Karlsruhe, August 2021 Sabine Paarmann

1 Introduction

Batteries as electrochemical energy storage devices are widely discussed, and they are utilised in numerous applications. Their potential as a buffer for renewable energies in the course of the "Energiewende" with ambitious goals [1] is particularly promising. Besides, they are in the spotlight of the public and politics regarding electromobility. And the expectations are high. With the rise of the automobile and as early as the beginning of the 20th century, the battery-powered electric motor was competing with the internal combustion engine. The outcome of this competition is well known and has its origin in the high costs, short lifetime, and low driving range of electric vehicles [2]. When Sony launched the first rechargeable lithium-ion battery (LIB) in 1991, its success began. By 2000, LIB were integrated into almost all laptops [3], but the application was limited to portable electronic devices. By now, the energy density has increased by a factor of four while the costs have dropped by a factor of ten [4]. Now, the battery is a growing element in the transportation sector, and electromobility is once again competing with the internal combustion engine – and the odds have changed. Due to the now changed circumstances, its market share is enormously expanding [5].

A major advantage of LIB compared to other storage technologies is their high energy and power density. However, the challenges for their acceptance and market breakthrough have not yet been overcome. Driving range, cost, safety, and lifetime of the battery still have to be addressed and improved [2, 6]. Improving the energy and power density is a priority in cell and pack design for an increased driving range. Cost and safety are critical aspects in automotive applications, which promoted the development of new materials [6].

Besides the acceptance in society, the battery lifetime is the decisive factor in the ecological sustainability of electric vehicles. In addition, companies are interested in a prolonged lifetime and lifetime prediction as they have to provide warranties for their products [7]. The United States Council for Automotive Research LLC (USCAR), for example, demands a lifetime of 15 years at 30 °C

and a cycle number of 1,000 to 300,000, depending on the application [8]. The lifetime is also vital for economic profitability as the battery costs contribute substantially to the total vehicle price. Besides the importance of a battery's lifetime, there is still a lack of understanding degradation, which leaves room for improvement [4].

Apart from the electrical and electrochemical aspects and optimisation potentials, the contribution of temperature to battery behaviour and ageing received little attention from the scientific community and industry over a long time [9]. This has changed significantly over the past few years. Especially for electric vehicles that need large battery packs containing vast amounts of energy and dissipating much heat, temperature effects become more relevant and a possible safety issue. The attention paid to the influence of temperature is increasing and is reflected in the growing number of publications. The findings obtained emphasise how crucial temperature is. The batteries' ageing, performance and usable energy depend on the internal temperature and temperature distribution. It should be operated in the optimal temperature range of about 15–35 °C, and a maximum temperature of about 55 °C should not be exceeded [10, 11]. The internal heat generation caused by both irreversible dissipation and reversible entropic effects is actively counteracted by external cooling. This induces temperature gradients inside the cell [12] and module and, depending on the temperature control strategy, also temporal temperature changes. For high C-rates, temperature differences in the cell of more than 10 K may arise [13]. Therefore, the optimisation of thermal management has a considerable potential to improve the battery packs with regard to weight, power and cost [9]. The close interaction of the electrical and thermal behaviour also results in an uneven current distribution [14]. Together with the temperature-dependent resistance, they cause a non-uniform heat generation within the cell that again influences the temperature distribution. This aspect poses a challenge, particularly for the widely discussed fast charging, which has not yet been solved sufficiently. Due to the temperature- and current-dependent ageing behaviour, it is to be expected that, coming along with these temperature inhomogeneities, ageing inhomogeneities develop over time [12]. For individual battery cells, this means that after a certain time, they will exhibit more severe ageing in certain areas than in others, and locally different degradation mechanisms may occur. Those

differences in the cells likely have a negative impact on the overall ageing behaviour. And while the main chemical processes related to battery ageing were established almost 20 years ago, the interdependencies between the factors involved are much less known [15]. For these reasons, the maximum temperature difference in modules is commonly limited to 5 K [3]. This value is frequently referred to as "common practice" [16], although there is no explanation or scientific evidence for it. In contrast, there is no such value regarding temperature inhomogeneities in individual cells altogether.

Thesis Aim and Hypothesis

Therefore, this work aims to provide a scientific foundation for the definition of a value for the maximum temperature difference over the length of a battery cell, which should not be exceeded for enhanced performance and lifetime. This objective includes addressing the following questions:

"How do temperature gradients influence the performance of LIB?"

"How do temperature and heat generation interact?"

"Does an inhomogeneous temperature distribution lead to locally different ageing effects?"

Those research questions will be investigated experimentally in the thesis at hand. Therefore, it is explored how complex external thermal boundary conditions affect the overall performance and ageing behaviour and to what extent Lithium-ion cells are able to tolerate temperature gradients.

First, relevant literature is reviewed to determine what is already known about the influence of temperature and non-uniformities concerning performance and degradation. Subsequently, the impact of non-uniformities is investigated experimentally. The performance is analysed by means of voltage, resistance and current. With the results, temperature-dependent correlations are derived for resistance and current, which are utilised to calculate the heat generation. Via these coherencies, also safety aspects can be addressed. In the next step, the

cyclic ageing under different defined thermal boundary conditions and the influence of inhomogeneities is investigated. The ageing effects at electrode level are analysed and evaluated regarding their homogeneity in a post-mortem analysis. Finally, the results are synthesised and correlated with the prevailing thermal boundary conditions.

2 State of the Art

The design and operating principles of batteries in general and lithium-ion cells in particular, as well as the materials involved, are explained in detail in numerous textbooks and other references [3, 17–19]. This section aims to condense the knowledge regarding the temperature influence on performance and ageing of LIB in the context of this work. Thus, particular emphasis is put on understanding the findings regarding inhomogeneities and how they can be identified.

2.1 Materials

In conventional lithium-ion cells, graphite on copper is used as the active material on the anode side. Figure 1 a) shows the voltage profile of graphite versus Li/Li^+ with its characteristic potential steps indicating the phases of graphite transformation with increasing degree of lithiation x. The steps differ regarding their stoichiometry of intercalated lithium. Stage-1, for instance, has the highest degree of lithiation with lithium between every graphite layer and a stoichiometry of LiC_6. Compared to the anode, there is more variety of active materials on the cathode side. Depending on the application, lithium cobalt oxide (LCO), nickel cobalt aluminium oxide (NCA), nickel manganese cobalt oxide (NMC), lithium manganese oxide (LMO), or lithium iron phosphate (LFP) is chosen [20] and coated on an aluminium current collector. Their voltage range and specific capacity vary significantly between the different cathode materials, as shown in Figure 1 b). Relevant to this work is LCO (purple) and NCA (cyan). These two materials are combined in the cell at hand to a blend cathode. The cell investigated in this work is introduced in detail in Section 3.1. LCO is characterised by a high specific capacity and long lifetime but is chemically unstable. Doping with nickel and aluminium enhances chemical stability. Both materials are layered oxides with a trigonal crystal and a hexagonal lattice system [21, 22] but with differing morphology. LCO particles are irregular in shape with a smooth surface. The spherical NCA secondary particles consist

of many primary particles, which are also practically spherical. Both are depicted in Figure 1 b). The overall voltage of a battery cell results from the subtraction of cathode and anode potential. The voltage ranges of the electrodes are not fully exploited. The so-called balancing, which is defined during production, determines how the voltage profiles are shifted against each other and which sections are utilised [23].

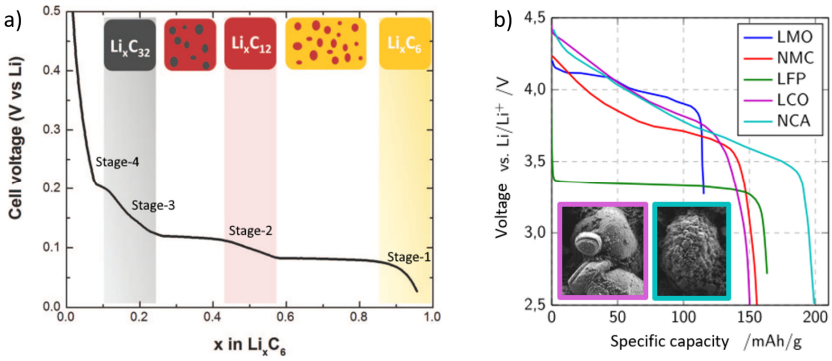

Figure 1. Voltages versus Li/Li^+ of a) graphite plotted over the degree of intercalation (adapted from Gallagher et al. [24], with permission of IOP Publishing) and b) cathode materials depending on specific capacity (adapted from Schmalstieg [25], license CC BY 3.0 DE).

The electrolyte in the pores of the active materials and separator consists of an organic solvent with a lithium salt, typically $LiPF_6$, as a conductive agent. Xu [26] summarises possible components, properties, and stability. The separator is a thin, highly porous membrane that usually consists of polyethylene (PE) or polypropylene (PP) [3]. The combination of materials determines the behaviour of the battery in all respects, including ageing characteristics.

2.2 Electrochemical Characterisation

Here, voltage and impedance that determine the behaviour of LIB are introduced. Their measurement allows the non-destructive examination of LIB.

These properties are used later to investigate the influence of temperature inhomogeneities and to quantify the cells' alterations during ageing.

Voltage Characteristic

One main characteristic for operation is the open-circuit voltage (OCV) as a function of the state of charge (SoC). The OCV represents the equilibrium at a given SoC and temperature. As soon as the cell is exposed to a current, dissipation mechanisms and thus overpotentials occur. They increase for higher currents, higher internal resistance, and lower temperatures. These conditions result in a lower voltage level for discharging while it is increased for the charging process. The measurement of the OCV is very time-consuming because of long relaxation times. Thus, often a quasi-OCV (qOCV) with small currents like C/20 or C/40 is measured. The standard capacity of a battery cell is measured according to manufacturer specifications, which is often a temperature of 25 °C and a C-rate of C/2 in certain voltage limits. The cell voltage results from the difference of cathode and anode potentials often defined and measured in half-cell configuration versus Li/Li^+. To the best knowledge of the author, nothing has been published yet on how temperature inhomogeneities influence voltage characteristics.

Differential methods emphasise inconspicuous changes in the OCV, as shown in Figure 2. The differential voltage analysis (DVA) in Figure 2 c) is the derivative of the voltage with respect to charge throughput, so it is the slope of the OCV in Figure 2 a). In analogy, for the incremental capacity analysis (ICA), the accumulated charge throughput is derived with respect to the voltage to calculate the differential capacity shown in Figure 2 b). The plateaus from the OCV that correspond to the individual phases of the electrochemical system appear in the ICA as peaks at which intercalation potentials can be determined [28]. The integral of the ICA is proportional to the charge throughput [29]. The curves are much less influenced by internal cell resistance than the OCV [30]. Both differential methods are mainly used for ageing diagnosis as their characteristics, e.g. peak height, are changing with ageing. The quality of the voltage measurement is crucial for an evaluation with ICA [27], and data has to be processed carefully to not be altered [31].

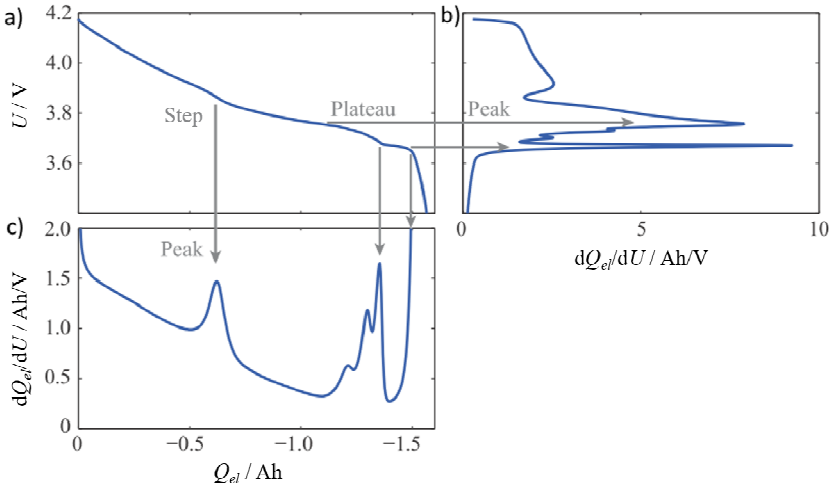

Figure 2. a) qOCV for a cell with LCO cathode and graphite anode, b) incremental capacity (ICA), and (c) differential voltage (DVA) (adapted from Schmidt [27], license CC BY-SA 3.0 DE).

Electrochemical Impedance

Ohm's law defines the relationship between resistance, current, and voltage for an ideal resistor with certain assumptions. These simplifications are not valid in a more complex system, and impedance is used instead of a simple resistance [32]. Electrochemical impedance spectroscopy (EIS) is a powerful tool for measuring impedance, characterising the dynamic behaviour of electrochemical systems, and separating the processes according to their time constants [33–36]. Spectra are recorded with a sinusoidal excitation signal over a frequency range. This signal can be either current or voltage. The response signal, either voltage or current, is also sinusoidal but phase-shifted. The complex impedance is calculated from the phase shift and the change in amplitude using Equation 2.1 [32].

$$Z(f) = \frac{U(\omega)}{I(\omega)} = \frac{\hat{U}}{\hat{I}} \cdot e^{j\Delta\varphi} = Z' + jZ'' \tag{2.1}$$

The theory behind the method and the calculation via Fourier Transformation requires a linear, time-invariant, and causal system [37]. Within certain limits, this is valid for batteries and can be verified via the Kramers-Kronig correlation [38, 39]. One freely available tool for this purpose is Lin-KK [40].

The real part of the impedance versus the imaginary part is depicted in a so-called Nyquist plot for visualisation. Alternatively, the magnitude of the impedance and the phase angle are plotted against the frequency in the Bode plot. Thus, the information about the frequency is retained. Often, equivalent circuit models (ECM) [41] are employed to further analyse the electrochemical impedance spectra. They compose different idealised elements to represent the individual processes in LIB and to approximate their behaviour [42].

The spectra reflect the internal processes, so they depend equally on the temperature and the SoC. Furthermore, the spectra change during ageing as different ageing mechanisms lead to an impedance rise. Therefore, EIS is also used to quantify its progress and the cells' state of health (SoH) [7, 43–47]. SoC dependency varies from cell to cell. In general, the impedance increases for lower SoC. The temperature dependency of the impedance follows an Arrhenius function [48–51]. Knowing this function, the internal temperature of the cell can be determined inversely by measuring impedance spectra. Either the real part [50, 52, 53], the imaginary part [49, 52], or the phase shift [51] can be selected as a temperature-dependent measure of the impedance. The method is mainly applied to establish a temperature control in the application [54] and expand it to battery packs [55]. Thus, the focus is on temperature estimation and not on how temperature gradients influence impedance. The authors use different frequencies for their evaluation: a trade-off between high temperature sensitivity, low SoC sensitivity, and measurement time when the method is aimed for temperature control. Concerning temperature gradients, Schmidt et al. [50] found that the ohmic resistance of a cell corresponds to that of its average temperature. In contrast, Troxler et al. [48] evaluated the charge transfer resistance, which decreases with an increasing temperature gradient. In their case, the resistance behaves as if the average temperature was higher. This effect is more pronounced at low average temperatures and reduced at higher

ones. Both authors considered temperature gradients perpendicular to the electrode layers. Pulse tests conducted by Klein et al. [16] reveal a significant decrease of resistance with an increasing temperature gradient. Opposing to this, other tests based on US06 [56] show a rising resistance with increasing gradient when more than about 10 % of SoC are (dis-)charged.

2.3 Temperature and Heat Generation

A battery cell itself is a complex system in which numerous (electro-)chemical reactions and various transport phenomena occur. The temperature dependency of all these processes adds complexity. The internal temperature is not uniform, and its distribution is dominated by heat generation, heat conduction, and heat dissipation [10]. Bernardi et al. [57] established the general energy balance for battery systems in 1985 and discussed the contributions to heat generation and internal temperature. Alipour et al. [58] summarised the temperature-dependent material properties and the main thermal, chemical, and physical equations with their dependency on temperature [58]. Bandhauer et al. [14] and Xia et al. [10] have written comprehensive reviews on the thermal aspects of batteries, and Offer [59] illustrates the temperature influence and provides a well-argued summary of the interrelationships.

The Arrhenius law [60] is valid for most of the processes taking place in a cell. This exponential increase of chemical reaction rates with rising temperature leads to a double reaction rate for a temperature rise of 10 K [61]. Mass transport is facilitated as the diffusion coefficients in the active material [62] and electrolyte [63] increase. These processes lead to reduced losses and a decrease in internal resistance. Low temperatures, in contrast, reduce the performance significantly. The poor low-temperature performance can mainly be attributed to the high charge transfer resistance of the electrodes [64] and the low lithium diffusivity in the carbon anode [65], which cause slower diffusion and intercalation [66]. Additionally, the lower electrolyte viscosity leads to sluggish ion transport, and materials, e.g., binder, get brittle at low temperatures [11, 67]. As a result, elevated overpotentials occur, and voltage limits are

reached earlier, leading to poor capacity utilisation. This performance deteriorating effect is shown in Figure 3 a), based on own measurements on the Kokam cell focused upon in this work. The available capacity decreases significantly with lower temperature, and at 0 °C (blue), only about one-third of the discharge capacity is reached compared to 50 °C (yellow). Similar behaviour is observed for aged cells at their end of life (EoL), with the behaviour being amplified at low temperatures. The temperature dependency of a discharge process is further illustrated in Figure 3 b). At the beginning of the 3C discharge, the cell has a temperature of 0 °C, which is raised to 50 °C at about 50 % SoC. This temperature change causes a distinct increase in voltage despite a constant discharge current.

The Arrhenius law also applies to the parasitic side reactions leading to degradation and increased resistance, especially for temperatures higher than 40 °C [3]. The ageing and its dependency on temperature will be covered in more detail in Section 2.5.

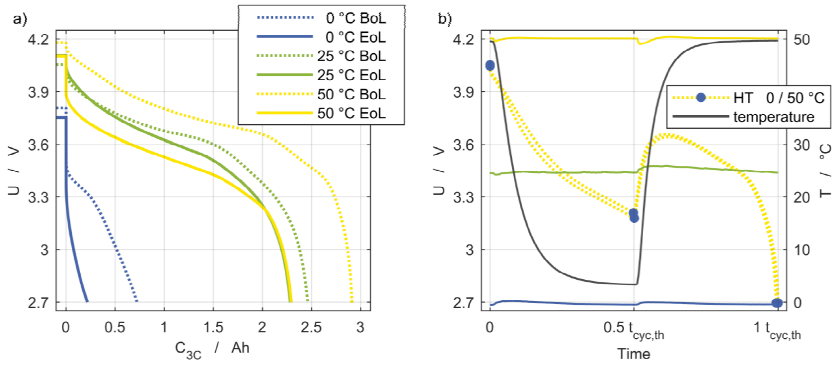

Figure 3. a) Voltage characteristic at 3C and different temperatures for Begin of Life (BoL) and End of Life (EoL). b) Voltage for a 3C discharge with a temperature change from 0 °C to 50 °C at about 50 % SoC. [68] (license CC BY 4.0)

The reduced losses and decreased internal resistances described above affect the current rate and the heat generation. The self-heating of the cell increases with increasing current and decreasing temperature [69]. Two main factors are contributing to heat generation [14], as represented in Equation 2.2. One is the

irreversible Joule heating $\dot{Q}_{irr}$, which is due to ohmic resistances and overpotentials [70]. This fraction increases with the square of the current and dominates the overall heat generation for high C-rates. The second is the reversible entropic heat generation $\dot{Q}_{rev}$ due to the chemical reactions and entropy changes. It is proportional to the current, and the contribution can be either positive or negative, depending on the reaction direction. Both, irreversible and reversible heat generation depend on SoC [71] without any particular pattern [72]. The heat generation of the individual components differs [73]. For cell chemistries containing LCO, the heat generation is dominated by this material for almost all C-rates [71]. It has significant kinetic limitations and the most considerable entropy change compared to other cathode materials or graphite [70, 71, 74].

$$\dot{Q}_{ges} = \underbrace{I \cdot (U - U_{OCV})}_{\dot{Q}_{irr} = I^2 \cdot R} + \underbrace{I \cdot T \cdot \left(\frac{\partial U_{OCV}}{\partial T}\right)_{SoC}}_{\dot{Q}_{rev}} \tag{2.2}$$

Temperature and heat generation affect each other, as electrical properties and temperature are linked [14]. Resistance and current are temperature-dependent and, at the same time, determine the heat generation. The effect of increasing heat generation due to a higher resistance at low temperatures is often assumed to be minor compared to a higher temperature leading to a higher current and therefore higher heat generation. Thus, usually, a positive feedback mechanism is assumed [48, 59, 75]. These interdependencies are especially relevant for inhomogeneities in battery cells. An increased current density follows the increased temperature caused by self-heating. Local electrochemical impedance varying with temperature [76] is the main reason for current density inhomogeneities. This leads finally to local SoC differences [69]. The origins, impacts, and interactions of inhomogeneities are discussed in depth in the next section.

2.4 Inhomogeneities

This section outlines which properties are potentially distributed inhomogeneously within the cell, how those inhomogeneities interact and how they affect

the cell. After a brief overview of different inhomogeneities, the focus is on non-uniform temperature distributions.

Already during the production processes, deviations occur in the electrode thickness, mass loading, and porosity. In particular, the latter two have significant implications on cell performance. It starts with machine tolerances leading to deviations at each manufacturing step and uncertainties in the structural parameters and deviations of electrochemical properties. This ultimately leads to variations on cell level that impact the lifetime and overall performance of cell and pack [77]. The variations of resistance and capacity within a cell affect the maximum currents, OCV, and SoC differences [78, 79]. Thereby, the influence on the current and charge throughput of a variation in capacity is minor compared to differences in impedance [80, 81]. At the beginning of a discharge or charge, the cell current is distributed inverse to the local resistance ratio until a certain OCV difference is reached [82]. This non-uniform current results in a non-uniform SoC and equilibrium potential distribution [83, 84], which means that the capacity of the active materials [85] is not fully exploited. This non-uniform utilisation of active materials reduces their energy density [84]. The discharge energy decreases almost linearly with non-uniformity of the current density [86], and qualitatively, the power loss distribution corresponds to the current distribution [75]. In general, the behaviour of high-power cells is more dynamic during (dis-)charge compared to high-energy cells [81]. Additionally, the cell design itself accounts for inhomogeneities. For example, the current density is higher near the tabs with a developing SoC gradient when distanced from the tabs [85]. Even at electrode level, local current densities differ and are in the region close to the separator far higher than average. For graphite anodes, this is the case at the beginning of each intercalation stage [87].

Crucial to the evolution of the current distribution during discharge is the OCV. A steeper OCV curve acts as a corrective and compensates the effect of diverging SoC, as the inhomogeneous distribution of equilibrium potentials balances the current distribution. Therefore, non-uniform SoC distributions have a self-damping effect [75], further induced by higher resistances at lower SoC. This effect is especially significant when the magnitude of the differences in the

equilibrium potential corresponds to the overpotential due to the cell resistances [83]. The current distribution following the OCV leads to a SoC balancing so that the highest SoC difference in the cell is not at the end of the discharge. As the SoC balancing is more effective for cell chemistries with a steeper OCV, NMC, LCO and NCA are well suited to be parallel-connected [75, 78].

This influence of the OCV on the current distribution also explains its typical wavy shape shown in Figure 4. Both in single cells a) and parallel connections b), initial effects occur followed by a plateau with an almost constant current over a certain range. In further progress, the compensation effects of the SoC mentioned above arise, and the current distribution reverses. Measuring the temperature, current, or SoC distribution within cells is impossible without affecting the system [76]. As a single battery with its layers behaves like a battery pack [59], often parallel connections are used to investigate current distributions. A similar characteristic shape is evident in Figure 4, even for different cell chemistries. To facilitate comparing the individual currents, the normalised current can be evaluated as in Figure 4 b). It is calculated by relating the current of each cell to the average current of all cells. If the current was equally distributed, the value for all cells would be unity.

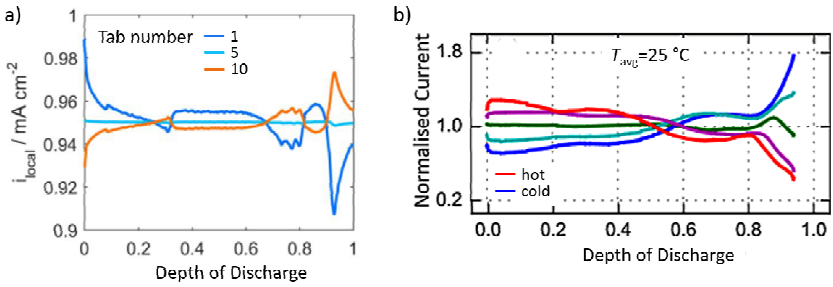

Figure 4. Current distributions at a C/2 discharge and an average temperature of 25 °C. a) Over the length of a multi-tab pouch cell (NMC) [88] (license CC BY 4.0) and b) in a parallel connection with five cylindrical cells (LFP) and a temperature difference of 20 K [83] (license CC BY-NC-ND 4.0).

The cells' internal resistance as the main parameter determining the current distribution depends on several factors such as temperature and SoC. In regions of the cell with a low temperature, the resistance is higher, leading to a non-uniform current, particularly at low temperatures below 0 °C [89]. There is some disagreement in literature on which effects are driving stronger inhomogeneities. According to Osswald et al. [90] and Zhang et al. [85], larger current and SoC non-uniformities occur for increasing cell temperatures and higher currents. Others claim that the difference of internal resistance between cells is much more evident at low temperatures [80] as significantly higher SoC differences occur at lower ambient temperatures [75]. Mistry et al. [91] found less uniform lithium deposition at lower temperatures leading to reduced capacity.

Another influential factor causing and amplifying inhomogeneities are thermal gradients [92]. In batteries, there always is a temperature gradient [59] caused by external temperature control or self-heating. Usually, the temperature at the cathode tab is higher than at the anode tab due to the lower electrical conductivity of the cathode materials [93] along with higher heat generation [94]. Intricate heat transfer paths due to the anisotropic thermal conductivity of the cell stack complexify the temperature distribution [95, 96]. Those inevitable temperature gradients are the main contributor to inhomogeneous cell parameters as electrochemical impedance varying with temperature [76]. They lead to significant non-uniformities in current and SoC distributions [76, 97]. Compared to the effects driving inhomogeneities, there is more consistency in literature regarding the impact of influencing factors with temperature gradients present. At a constant temperature difference, a lower SoC and lower average temperature results in greater divergence [83, 98]. Likewise, temperature gradients due to self-heating increase with increasing C-rate and decreasing temperature [69]. An increase in temperature difference has a minor impact on energy density, but the inhomogeneity in current density is increased [98]. A non-uniform temperature distribution has a self-intensifying character. With a positive feedback mechanism, they accelerate themselves [48, 59, 75, 92], making the electrical system inherently unstable concerning temperature gradients [99]. The extent of inhomogeneity depends on the cell chemistry. Klein and Park [83] found a current fraction of 80 % in the warmest cell in a parallel connection of five NMC cells that was twice as high as for LFP.

Ageing mechanisms are temperature-dependent, as the Arrhenius law applies for parasitic side reactions, and mainly low temperatures trigger lithium plating. Therefore, a temperature distribution causes locally different rates of side reactions. With the coupled electrochemical inhomogeneities, local ageing differences occur, affecting and accelerating the overall cell ageing [66, 69, 76, 100]. Its performance degrades slightly faster compared to a cell with the same average temperature but without a temperature gradient [12]. According to Lewerenz et al. [101], the localised ageing effects are impacted by the homogeneity of lithium distribution. The non-uniform degradation enhances the inhomogeneity of cell parameters [102], and the temperature distribution in aged cells differs completely from pristine ones with much higher temperature gradients [99]. This further increases unbalanced currents and other inhomogeneities. Those findings are consistent with observations in parallel connected cells. Their inconsistency causes degradation of the overall pack [10, 84], where a 20 % difference in resistance can result in a 40 % reduction in cycle life [103]. The degradation caused by non-uniform current distribution is amplified when temperature gradients are present [104]. Over the battery lifetime the current distribution changes due to the inhomogeneous resistance change caused by local ageing [84, 105], and aged cells exhibit an increased parameter variation compared to new cells [106]. Not only is the ageing inhomogeneously distributed, but also temperature gradients can evoke other mechanisms. For instance, Carter et al. discovered plating in a coin cell with an inter-electrode gradient of 2 K, an average temperature of 35 °C, and a current of C/5. In contrast, there was no plating under isothermal conditions [107].

We can state that many factors cause and intensify inhomogeneities in LIB. A very influential one is an inhomogeneous temperature distribution. So far, as can be seen from the above, there is a large number of publications that report this influence qualitatively, but no quantitative correlation is established. A common assumption related to packs is a maximum temperature difference of 5 K. Although it is widely accepted, no physical, statistical or otherwise founded justification for this value can be found.

2.5 Ageing Behaviour

In lithium-ion battery cells, alterations occur over time and during operation, which becomes noticeable by the reduction of the overall performance and storable energy. A variety of studies on ageing behaviour and lifetime prediction can be found in literature. They differ regarding cell chemistry and format as well as boundary conditions and stress factors. In general, it is distinguished between cyclic ageing and calendar ageing during idle periods. For calendar ageing, the storage temperature and the SoC have the highest impact on the degradation behaviour over time. Both for higher temperatures and higher SoC, the ageing is accelerated [108–115]. Nevertheless, the temperature is the primary influencing variable and significantly determines long-term behaviour. However, different cell chemistries exhibit other characteristics during calendar ageing [116].

The main stress factors determining cyclic degradation are temperature [46, 117–132], depth of discharge (DoD) [111, 124, 127, 130, 133, 134], correlated with the average SoC [121], and C-rate [46, 47, 121, 124, 127, 130–132, 134, 135]. Often, the ageing progress is not expressed as a function of time but in relation to the charge throughput as equivalent full cycles (EFC). Another relevant issue is fast charging [136], with different charging protocols influencing ageing [127, 128, 137]. Su et al. [138] statistically ranked the influencing factors starting with the highest impact: charging current – upper cut-off voltage – temperature – lower cut-off voltage – discharge current. Some studies address the combination and superimposition of calendar and cyclic ageing [111, 114, 139, 140]. Different mechanisms on electrode and particle level are triggered during the ageing process, outlined in the next section. Collectively, they reveal themselves as capacity fade or resistance increase (power fade) in the cell behaviour. They are typically quantified in most studies to evaluate the ageing progress. Both should always be considered to gain a holistic understanding.

Focussing on temperature, literature shows that the capacity fade and resistance increase, and therefore the ageing, are accelerated at higher and lower

operating temperatures. For homogeneous temperatures, the ageing rate depends on the temperature expressed by an asymmetric U-shaped function [118, 122]. This reflects two different superimposed correlations determining the ageing behaviour regarding temperature. The temperature at which ageing is minimal depends on cell chemistry and cycling conditions [124]. Sometimes thermal runaways account for degradation. This safety-critical phenomenon is a chain reaction of exothermal chemical reactions and usually accompanies an internal short circuit and leads to the destruction of the battery. In this case, the occurring reactions are not representative of conventional battery behaviour or degradation and are therefore not considered in this thesis.

While the effect of absolute temperature on ageing behaviour is well investigated, information on other temperature effects is scarce. Hunt et al. [141] compared surface to tab cooling and found a faster degradation for surface cooling. They attribute this observation to the gradient perpendicular to the electrode layers, which causes a different behaviour in each layer. The gradient parallel to the layers, in contrast, provides a uniform utilisation of each layer. Fleckenstein et al. [12] implemented ageing in an electrical-thermal model. He concluded that the electrical performance with temperature gradient degrades slightly faster than an isothermal cell with the same volumetric average temperature. Carter et al. [142] and Atkinson et al. [143] deliberately provoke or inhibit plating within a coin cell by the directionality of the interelectrode thermal gradient. Besides temperature gradients, temperature changes have an impact on ageing that is not yet known. Preliminary results from Gering et al. [144] indicate a slightly increased impedance for the severe thermal cycling between 10 °C and 40 °C. Carter et al. [145] observed massive lithium plating for cells charged under a thermal transient either from 40 °C or 10 °C to 0 °C. According to Chang et al. [146] also transitions to higher temperatures can lead to failure within practical temperature ranges.

In detail, it is not possible to distinguish the various individual ageing mechanisms in an operational battery, which are introduced in Section 2.6. Therefore, they are often grouped according to their implications, leading either to a loss of active material (LAM), a loss of lithium inventory (LLI) or an increase in resistance [147]. Both differential methods help to identify them. Dubarry, for

example, prefers to evaluate ICA [148–152], while others like Bloom consider DVA [28, 153–155].

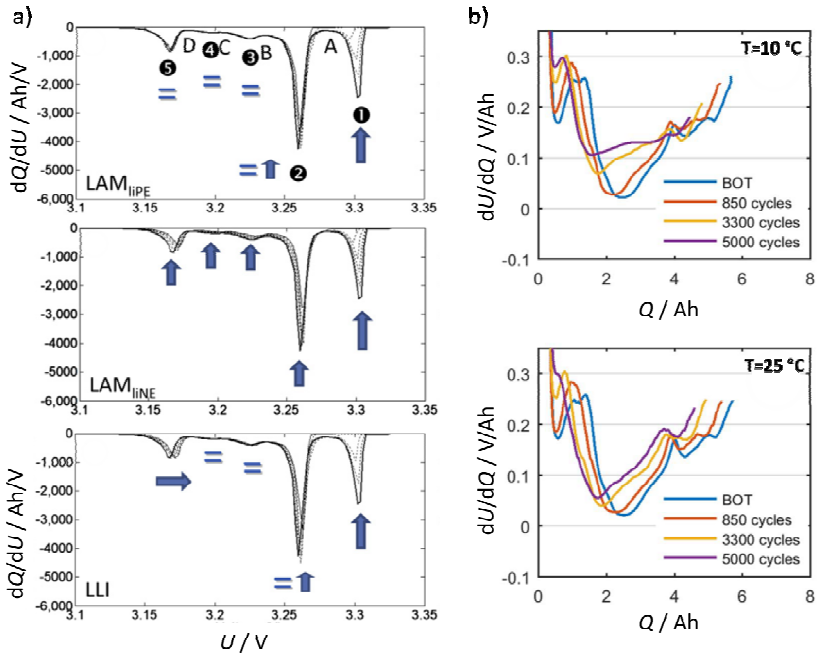

Figure 5. a) Differences in the ICA for LAM and LLI at the positive and negative electrode [148] (with permission from Elsevier) and b) changes in DVA from the begin of test (BOT) to 5000 cycles for 10 °C and 25 °C [46] (license CC BY 4.0).

Theoretically, a loss of active material can be assumed to cause a uniform decrease in electrode capacity, meaning the peaks from one electrode move closer together with ageing [28]. Dubarry et al. [148] present a concise example of how LLI and LAM affect ICA, as shown in Figure 5 a). In ICA, the occurring changes are difficult to assign precisely. In the DVA, LLI hardly alters the curve, but the last slope moves to lower capacities. Thus, the curve is virtually cut off. Sometimes it also becomes noticeable by a parallel shift of the DVA [156]. For LAM, different changes occur depending on whether charging or discharging is considered. Common is a compression of the curves

and a convergence of the peaks. Figure 5 b) shows a typical evolution of the DVA over ageing for cycling at 10 °C and 25 °C. A similar representation of LLI and LAM can be found in the dissertation of Wu [156], complemented by the influence of the ohmic resistance, which cannot be seen in the DVA and shifts the unchanged characteristic along the x-axis in the ICA. Several ageing results show reduced peak heights and peak shifts in both, with a shrinkage of the curve indicating LAM [150, 154]. Lewerenz et al. [101] observe different peaks in the DVA being sensitive to LLI or LAM. While LLI mainly impacts the peaks at high SoC, LAM affects the DVA by compressing it at low SoC.

Usually, LLI and LAM occur together with different shares to the capacity loss, and it is often hardly possible to reliably distinguish them [46]. In addition, blurring of the peaks or their shift in the ICA can be caused by increased (polarisation) resistance [151]. These less defined patterns may indicate slow kinetics [157] and hinder the interpretation regarding the degradation modes. Carter et al. [107] simulated their effect on ICA. They detected a reduction of peaks for LLI and a shift of different peaks in certain directions depending on which electrode LAM occurred. Sarasketa-Zabala et al. [158] verified LAM at the graphite anode with scanning electron microscopy (SEM) and X-ray diffraction (XRD). By measuring half-cell potentials versus lithium, the peaks of the DVA and ICA can be assigned to the individual electrodes [28, 46]. Once this assignment is established for a material combination, alterations in DVA and ICA can be related to the electrodes. Also, for blend electrodes, individual peaks can be attributed to each component, e.g., in NCA/LCO mixtures [46]. Thus, it can be identified that cathode characteristics shift with respect to capacity, while the anode remains almost unchanged [23, 150] and vice versa [159]. This shift changes the electrode balancing determined during production. Bloom et al. [154] report a disappearing anode peak during cycling. They assume it to be due to an increasing amount of decomposition products between the graphene layers caused by solvent co-intercalation. During ageing, the shift in the alignment of the electrodes changes [160], often referred to as electrode slippage [28]. The main driver for this phenomenon is LLI [161, 162] which usually has a significant contribution to capacity fade [151, 158]. Keil and Jossen [163] found the shift in electrode balancing to be the primary ageing

mechanism as it triggers other processes such as passivation layer growth [163] both at anode and cathode.

The temperature effect on ageing behaviour is also evident in the DVA. For both higher and lower cycling temperatures, the DVA shows greater changes that differ from each other. The high temperature from around 40 °C causes the peak indicating stage-1 of graphite to disappear, suggesting a higher loss of positive active material or lithium inventory [46, 152]. Lower temperatures cause a much flatter main peak [46] and a stronger shift [164] compared to higher temperatures, as shown in Figure 5 b). According to Carter et al., temperature gradients perpendicular to the electrode layers induce LAM at the colder electrode, especially when the anode is colder [107] than the cathode. Furthermore, inhomogeneities in ageing can be detected within certain limits. Bloom et al. [153] observe the splitting of an anode peak and attribute this to a local decrease in accessible material. Lewerenz et al. state that the height of the graphite peak at low SoC decreases [101, 165] if there is a variety in lithium concentrations in the anode. The inhomogeneous lithium distribution causes the phase transition not to take place simultaneously, so the OCV/DVA/ICA is a superposition with less distinct features. Others [166] also observe this phenomenon. Bach et al. [167] note a large scatter in the results of the half-cell samples that average the course of the original aged cell. Thus, the peaks in the ICA are smoothed. In addition, the degradation modes do not begin simultaneously, but LLI occurs first before LAM increasingly sets in [149].

Identifying underlying mechanisms, either physical or chemical [168], that provoke ageing is difficult as they often interact [2, 169, 170] and affect battery components with similar consequences and at a similar time scale [171]. The mechanisms can be identified, however, with the help of cell openings and subsequent analyses.

2.6 Ageing Mechanisms

The diversity of ageing mechanisms is the subject of numerous publications. Mostly, the focus is on a specific mechanism, as plating and SEI growth, or on a component. Some reviews summarise the mechanisms graphically [172, 173] or in tables [121, 166, 173] and consider the interdependencies [174].

The underlying root causes are mostly various chemical or structural changes inside the cell and observed in all cell components. Diverse degradation mechanisms reflect that Li-ion cells are operated close to or outside the stability window of their materials [22]. Due to inhomogeneous conditions in the cell – thermally, electrically and mechanically – ageing and all its processes likewise proceed non-uniformly. In the following, typical ageing phenomena are explained, focusing on the materials employed in the cell type analysed in this thesis.

Graphite as anode material is used in most of today´s applications. The exact composition of the electrolyte is not known for the cells used in this thesis. Presumably, it is a mixed carbonate solution with $LiPF_6$, which is almost identical for all battery producers and only varies in the amount and type of additives. Therefore, the ageing mechanisms are expected to be comparable [2]. In contrast, the different cathode materials impact the individual ageing mechanisms [2]. The investigated cells comprise blend cathode of NCA and LCO, which are both layered oxides. The similar crystal structure leads to similar ageing mechanisms.

2.6.1 Anode Active Material

The primary degradation mechanisms at the anode are the growth of a solid electrolyte interface (SEI) and lithium plating [123, 171], both occurring at the electrode/electrolyte interface. In addition, mechanical degradation may arise during operation. Agubra and Fergus [175] give a detailed review of ageing mechanisms on the anode.

Solid Electrolyte Interface

Conventional organic electrolytes are stable between 1 V – 4.5 V but not at the prevailing low potential of the graphite anode of about 0.05 V [2]. They react with lithium on the surface of the active material or decompose at the anode's surface, forming a passivating surface layer [26, 176]. The decomposition and reaction products build up to an ion-permeable layer on the surface called solid electrolyte interface. Typically, it contains Li_2CO_3, $ROCO_2Li$, $(CH_2OCO_2Li)_2$, and LiF, comprises crystalline and amorphous components [177] and is a few nanometers thick [178]. The electrolyte and its components play a crucial role in forming a stable SEI with low resistance [18]. Verma et al. [179] provide a broad overview of parameters influencing SEI formation and techniques to characterise its properties. Although the SEI poses an additional resistance and cyclable lithium consumption causes an irreversible capacity fade, it is necessary to protect the active material from further decomposition [176]. Thus, the initial formation of a stable SEI is most desirable. Peled [180] raised detailed considerations about the SEI and concluded already in 1979 that a "proper anodic SEI is the key for the operation". During battery life, the SEI thickness increases due to decomposition products [181]. This process has no further advantage but increases the resistance and the loss of active lithium [175, 182]. The resistivity of the SEI layer correlates with its thickness, which increases with the square root of time [183]. In extreme cases, the SEI can grow to a micrometre thick layer on top of the anode [184]. SEI evolution and its characteristics can also be affected by transition metal dissolution, an ageing effect at the cathode. Current, temperature and voltage are essential for SEI growth [185, 186], especially the polarisation and overpotentials [187–189] at the anode. Temperature determines the reaction kinetics of SEI formation [190] and transformation. At elevated temperatures, the SEI layer grows faster, becoming more porous and unstable [66]. In $LiPF_6$ systems, the SEI is thermally unstable at temperatures above 60 °C [66, 191] and reacts with the electrolyte or active material [179]. With a further temperature increase, unstable components convert to more durable species like Li_2CO_3 [192, 193]. The deposition of constantly new reaction products may cause clogging of pores [184, 194]. Additionally, the volume expansion during (de-)lithiation of the graphite and the SEI [195] itself causes mechanical stress, leading to fracture. The SEI is the

weakest material and, therefore, more prone to fracture than graphite [196]. The created fresh graphite surface reacts again with the electrolyte to new SEI, causing more loss of active lithium. Concerning overpotentials, the most severe conditions prevail at the anode-separator interface, resulting in a thick SEI layer and high film resistance there [197]. Since SEI growth highly depends on the conditions, it is sensitive to when they are inhomogeneously distributed. As a consequence, the SEI growth is inhomogeneous over the thickness and the length of the electrode [198].

Lithium Plating

Plating describes the phenomenon during charging when lithium ions are reduced and deposited on the graphite surface instead of intercalating into the lattice structure. Literature broadly agrees that plating originates from limitations either in the charge transfer or the lithium diffusion in the graphite. Typically charging with high currents or at cold temperatures [198] combined with an already high SoC [127] are associated with plating [66, 128, 199]. It can occur when the anode potential drops below the standard potential of Li/Li^+ [128]. Li et al. [200] provide an overview of lithium deposition and its main aspects, like when it occurs, its morphology how it is influenced and potentially interacts with the SEI. Although according to conventional theories, mainly low temperatures lead to plating, it may also occur at elevated temperatures [123]. In addition, Carter et al. [145] report plating for charging during a temperature transient. They also showed that plating is not limited to high currents but that even conditions of 35 °C and C/5 can lead to enhanced deposition when interelectrode temperature gradients are present [107, 142]. Those findings indicate that plating is less understood than it might appear. For inhomogeneous temperatures parallel to the electrode, plating is observed in the warmer cell regions as the higher current dominates [161]. In this case, the location but not the severity of plating [201] is influenced. Lithium deposition is an inhomogeneous process that gets more uniform with higher temperatures [91, 143]. Preferably, lithium deposits at the edges of the electrode sheet as there the lithium concentration increases faster than in the bulk [161]. This so-called edge effect even occurs when the anode is oversized. Part of the lithium loss caused by plating is reversible and is restored after the so-called stripping

process [202]. The irreversible plated lithium reacts with electrolyte to SEI, becomes electrically isolated, and therefore 'dead lithium' [143, 161]. Besides the massive loss of lithium, plating poses a potential safety risk when lithium deposits as dendrites [175]. Severe plating that covers the electrode surface disables the intercalation and leads to a partial, non-uniform utilisation of the active material [127].

Mechanical Degradation

During lithium intercalation, the host material expands, and it contracts during deintercalation. Graphite exhibits a volume change of about 10 %. In the long run, this mechanical stress leads to cracking within the active material. Crack propagation may even cause isolated particle fragments with no electrical contact to the current collector. This is more likely for higher C-rates and low temperatures. The stress is induced by higher concentration gradients in the particles due to a lower diffusion coefficient [203, 204]. At elevated temperatures, on the other hand, the cell generates larger thermal stress [205], accelerating fracture. The formation of cracks exposes fresh surface that reacts with electrolyte to SEI consuming lithium [204, 206].

Related to particle cracking is exfoliation, which is the cracking along graphene layers. This is either provoked by solvent co-intercalation [207] or by the pressure due to gas formation [208] at the crevices at the edges of the layers. A stable SEI can prohibit the exfoliation tendency [209]. Additionally, delamination of the active material layers, the separator and the current collector [210] can occur. High C-rates increase stresses at the electrode-separator interface [211], and high temperatures degrade the binder, which ensures the electrical conductivity between graphite and the current collector. This can be compensated by applying mild pressure on the electrode stack [212].

The consumption of electrolyte in side reactions leads to gas accumulation. This dry-out of pores electrochemically isolates particles or electrode regions, especially at temperatures above 25 °C [46]. The electrode dry-out is suspected to be one potential reason for the knee point [213], at which ageing accelerates rapidly.

2.6.2 Cathode Active Material

Both NCA and LCO belong to the layered oxides, and their ageing mechanisms have been detailed by Hausbrand et al. [22].

Similar to the SEI on the anode, irreversible decomposition (oxidation) [26] of the electrolyte leads to a surface layer on the cathode particles that contains decomposition products [22]. Major components are LiF, LiPFO, and (Li)CHO. Its formation is strongly influenced by SEI components migrating from the anode to the cathode surface [214]. At high temperatures and voltages, the surface modification is more pronounced. It reduces the active surface area by blocking pores and hinders the lithium kinetics, increasing the impedance [215]. At high voltages, this surface layer breaks down accompanied by the evolution of mainly CO_2 [26]. The loss of lithium caused by the surface layer formation shifts the voltage characteristics of the electrodes and leads to an overcharging of the cathode material. This can induce oxygen to be released from the crystal lattice, which then reacts with the electrolyte. The remaining defects and oxygen vacancies lead to an intrinsic instability, especially of $LiCoO_2$ in the delithiated state [22].

A critical ageing mechanism in cathode active material is mechanical degradation leading to disturbed electronic pathways within the composite cathodes and, therefore, to higher contact resistance [216]. Primarily at high voltages, cracks emerge at the boundaries of primary particles [137]. This intergranular cracking can largely be attributed to the strong anisotropic evolution of the crystal structure during lithium (de-)intercalation [67]. Therefore it depends on the SoC range during cycling and less on temperature. With the separation of the primary particles, the kinetic behaviour of individual oxide particles becomes non-uniform [216]. Additionally, the exposure of fresh surface to electrolyte accelerates structural damage and mechanical disintegration [137]. The electrical pathways are further degraded when the carbon-binder mixture detaches from the particles, and the secondary particles lose contact [217].

For cathode materials, mechanical degradation also on the atomic level is relevant when – potentially – lattice parameters change. They depend on lithium concentration and thus change reversibly during every charge and discharge

process [218]. Irreversible changes in the crystal structure from rhombohedral to electrochemically inactive cubic mainly occur at the particle surface, reduce the specific capacity of the active material [219] and increase the charge transfer impedance. This process is accelerated at high cathode potentials [2, 67, 137] when the cell is cycled to upper cut-off voltages of 4.2 V – 4.5 V. Besides the changes in the lattice structure, so-called cation mixing can occur. Nickel and lithium ions are similar in size so that nickel cations can migrate into the delithiated layers of the crystal structure [215]. This lowers the lithium stoichiometry, resulting in a loss of capacity. Transition metal swapping their places is known as antisite defects and occurs mainly in NCA and NMC [2]. This effect and vacancies in the structure result in less cathode stability [22]. Especially at fresh surfaces originating from particle cracking, transition metals dissolve [220]. This ageing mechanism mainly affects the SEI, where the transition metals alter its formation and lead to an enhanced loss of lithium. Manganese is prone to metal dissolution, but also nickel, cobalt, and rarely aluminium can be found in the SEI.

Overall, the ageing mechanisms at the cathode are less sensitive to temperature than those on the anode, but the voltage (range) is decisive for its degradation.

2.6.3 Passive Components

Electrolyte

A detailed analysis of possible reaction paths and degradation products is provided by Nowak et al. [221]. Xu et al. [26] give an overview of voltage and temperature ranges in which the electrolytes are stable and comment on possible decomposition mechanisms.

It is known that conventional organic electrolytes are stable between 1 V – 4.5 V but not at the prevailing low potential of the graphite anode [2]. They react with lithium on the surface of the active material or decompose at the electrode surface [26, 176]. Electrolyte solvents decompose reductively on graphite generating gaseous propylene as one of the reaction products. Additionally, radical anions are generated, which continuously further degrade the

solvents [26]. Not only are electrolytes chemically unstable but also thermally. The thermal decomposition starts at temperatures >60 °C. The most unstable component in the system, both chemically and thermally, is $LiPF_6$ [221]. It decomposes at 50 °C – 60 °C. The electrolyte must contain as little water as possible since even traces would cause side reactions with lithium and lead to unwanted surface layers [18].

Separator

The primary ageing mechanism affecting ion transport through the separator is the reduction of porosity. This particularly occurs when deposits clog the pores, for example, during SEI formation or lithium plating. In addition, the separator is with a yield strength of 10 MPa – 40 MPa mechanically the weakest link and susceptible to mechanical stress. Viscoelastic creep may induce pore closure and reduce ion transport [222]. Elevated temperatures increase the creep rate, although typical separators made of PE or PP have a melting point around 130 °C – 160 °C [223].

Current Collector

Copper and aluminium have good chemical stability. Nevertheless, the harsh conditions in batteries can lead to their corrosion. At high SoC during calendar life tests, the aluminium current collector may suffer from severe pitting-like corrosion leading to capacity fade [26]. Copper, in contrast, is sensitive to impurities in the electrolyte, which dramatically increases its oxidation tendency [224].

2.6.4 Non-Uniformities in Ageing Mechanisms

In reality, the individual mechanisms described above often coincide and are mutually dependent [174]. Moreover, the same integral phenomenon [107] can be triggered by different underlying root causes. For instance, the knee point or sudden death can be initiated either by transition metal dissolution, leading to accelerated SEI growth [7] or by pore-clogging of graphite leading to lith-

ium plating [130, 158]. Another example is the shifting of the anode characteristic due to lithium loss, resulting in higher voltages at the cathode and consequently its damage. Despite these complex couplings, the stability of SEI is key to the overall cell stability. Then the nature of the positive electrode and its reactivity determine the battery ageing characteristics [182].

Observing the ageing mechanisms, it is noticeable that they are hardly homogeneous and at most statistically distributed. The SEI is heterogeneous in terms of its components, and it comprises crystalline and amorphous parts [177]. Plating occurs preferentially at the edges and is extremely local and inhomogeneous [143, 198]. In addition, the morphology changes depending on the conditions so that not all plating is the same. Plating is also strongly influenced by uneven temperature [142]. Non-uniform SEI and plating, covering the surface, decrease the electrode area, which in turn increases the inhomogeneity in the cell [225].

2.7 Identifying Inhomogeneous Ageing

Under certain conditions, specific processes can be observed in-situ or in-operando. In ageing tests on commercial cells, a post-mortem analysis is usually performed to identify and assign individual mechanisms [123]. Various methods are used to detect and quantify the changes that occur to capture a wide variety of effects. Waldmann et al. [172] provide a detailed overview of the analysis methods and what they are sensitive to. With each physico-chemical analysis method, it is only possible to identify specific aspects of degradation. Several complementary methods are necessary to achieve a holistic picture of the ageing mechanisms. A reasonable combination provides information regarding microstructure, crystallographic structure, and chemical composition [172]. A full understanding of the ageing processes is obtained with additional electrochemical investigations of the electrodes in half-cells and their evaluation. For the identification of inhomogeneities, this must be taken into account when selecting the methods [226].

2.7.1 Cell Opening and Sample Preparation

Regarding the procedure of cell opening and sample preparation, Waldmann et al. [172] and Williard et al. [227] provide a summary of the significant points. The opening of LIB requires a controlled environment with minimal concentrations of oxygen and water to ensure consistency between cell and disassembled components. Especially for chemical consistency, a glovebox with a dry Argon atmosphere is necessary [227]. For further analysis with scanning electron microscopy (SEM), inductively coupled plasma optical emissions spectroscopy (ICP-OES) or X-ray diffraction (XRD), a brief contact with air does not alter the results [167, 227, 228]. An important and crucial step is washing the electrode material, although there are different aspects and studies on how the procedure should look like. The aim is to remove residual conductive salt that remains on the surface when the electrodes dry. The literature largely agrees on dimethyl carbonate (DMC) as a solvent. However, German et al. [185] use diethyl carbonate. In his dissertation, Winkler [178] studied washing treatments with different combinations of DMC and propylene carbonate (PC) and concluded that DMC with 10 vol-% of PC followed by rinsing with DMC produces the best results. The exact procedure applied by the authors during the washing process varies greatly. One challenge is that not only conductive salt residues ($LiPF_6$) but also parts of the SEI (LiF, Li_xPF_y) are dissolved [229]. According to Schmid et al. [230], the washing procedure has no impact on the deviation in capacity, but the variations in impedance are significant when the material has been washed. In contrast, there is general agreement to remove active material from the current collector using n-Methyl-2-pyrrolidone (NMP) before experimental cells are build up [136, 218, 231, 232]. Along with the sophisticated measurement methods explained subsequently, measuring the layer thickness can be revealing [233]. Waldmann et al. [118] found an increase of thickness for anodes aged at $T > 25$ °C and attributed it to the SEI growth.

2.7.2 Electrode Characterisation

There is a wide range of characterisation methods that are applicable to battery materials. However, since the measurements are ideally carried out in the absence of air, the adaptation for the intended purpose can be very costly. Partly, possible analytical methods complement each other, and partly they are redundant. Waldmann et al. [172] provide a good but not all-encompassing overview of the methods and their employment in battery research.

With atomic force microscopy (AFM), for example, mechanical properties, surface morphology and conductivity can be measured on the nanoscale. It has high potential but is not yet state of the art for battery materials as their surfaces are extremely rough. The challenges for determining the porosity or active surface are of a different character. Although physical adsorption, mercury porosity, and optical microstructure reconstructions are principally suitable, each has its drawbacks. The active surface of battery materials is too small to obtain quantitative results with gas adsorption. The uncertainty of mercury porosity is too high to detect differences between samples, and 3D reconstruction via SEM combined with a focused ion beam is extremely costly and has difficulties distinguishing pores, carbon black and binder. The analysis techniques used in this work are briefly presented below.

X-Ray Diffraction

X-ray diffraction analyses the crystal structure of the sample material by diffraction of X-rays. The theory behind the technique and the measurement principle is addressed in several textbooks [234, 235]. Different anodes, typically copper or molybdenum, are used as radiation sources depending on the sample or the atomic distances in the sample. They differ in the emitted wavelength λ of the radiation. If the wavelength of monochromatic X-rays is in the same order of magnitude as the diffraction grating, they are diffracted, and interference develops. In ordered crystal structures, constructive or destructive interference occurs at certain angles. These angles depend on the distance between the atoms and thus allow conclusions to be drawn about the crystal structure. In an XRD spectrum, the intensity is plotted over twice the diffraction angle θ, resulting in distinct peaks. Based on their position, the lattice plane spacing d

can be determined via Bragg's law according to Equation 2.3. Subsequently, the reciprocal and real lattice parameters a^*, b^*, c^* and a, b, c are calculated. The letters h, k, and l refer to the Miller indices.

$$2 \cdot d_{hkl} \cdot \sin\theta_{hkl} = n \cdot \lambda \tag{2.3}$$

$$\frac{1}{d_{hkl}^2} = (h^2 + k^2 + h \cdot k) \cdot a^{*2} + l^2 \cdot c^{*2} \tag{2.4}$$

$$a^* = b^* = \frac{2}{a\sqrt{3}} \qquad c^* = \frac{1}{c} \tag{2.5}$$

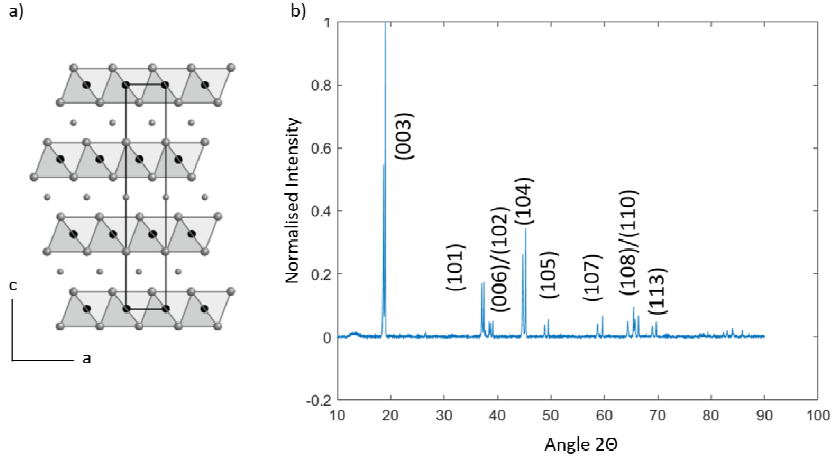

Figure 6. a) Layered crystal structure of LCO [3] (with permission from Springer). Black atoms represent cobalt, grey atoms oxygen and the small atoms are lithium. b) XRD spectrum of a LCO/NCA blend cathode with Miller indices labelling the respective peaks.

The crystal structure of a layered oxide is shown in Figure 6 a), with a hexagonal unit cell being highlighted and the coordinate system indicating the direction of the lattice parameters.

Graphite anodes are usually not affected even by heavy cycling [236]. In this work, X-ray diffraction is applied to powders of the cathode material to study the crystal structure changes during ageing and relate those to the thermal boundary conditions. The spectrum of a LCO/NCA blend cathode is shown in Figure 6 b). Both materials have the same crystal structure, and therefore, all

peaks appear twice in the spectrum. The peaks located at slightly smaller angles can be assigned to NCA. According to the literature, the lattice parameter *a* does not change remarkably during cyclic ageing for either NCA or LCO [120, 133, 236], whereas parameter *c* increases [236, 237]. Ramadass et al. [120], in contrast, found a smaller *c*/*a* ratio indicating a decrease in lithium stoichiometry with cycling. A shift of the peaks with Miller indices of (003) and (104) to lower angles can be attributed to lithium deficiencies in discharged LCO [236]. There are rarely changes in the crystal structure [120, 237], but Maher et al. found the peak (003) to split, which they relate to a transformation from hexagonal to cubic spinel lattice [236].

Inductive Coupled Plasma – Optical Emission Spectroscopy

Optical emission spectroscopy (OES) is based on the characteristic wavelength emitted by excited electrons to identify elements. In ICP-OES, the sample is injected as an aerosol into an inductively coupled plasma (ICP) for excitation. The measurement principles are available in detail in literature [238, 239]. One advantage in battery research is that ICP-OES can detect almost all elements, including lithium, except hydrogen, fluor, carbon, and oxygen in a broad concentration range from ppm to major components [44]. Sample preparation involves the generation of an aerosol, so solids are digested in acid, for example. Digestion of graphite can only be achieved with great effort, but with aqua regia [44], partial digestion can be reached, which is sufficient for the analysis. The whole sample is dissolved and measured at once, which means no local phenomena can be analysed except separate samples are taken. ICP-OES is frequently applied for identifying dissolved transition metals from the cathode that were transported through the electrolyte to the surface of the anode. The chemical stability increases in the order manganese, nickel, cobalt, aluminium [220]. Therefore, manganese is most likely to be found at the anode, followed by nickel and cobalt. This phenomenon is sometimes referred to as cross-talk [44]. The transition metals integrate into the SEI layer leading to a loss of cyclable lithium and enhanced SEI growth. Ageing, namely capacity fade and resistance increase [240], and the SEI thickness correlate linearly with lithium phosphorus and manganese concentration [118]. For nickel and cobalt,

the correlation is less explicit [220]. The concentration of those elements increases with temperature and time [118, 123, 167]. The additional lithium found on aged anodes is correlated to a lithium loss from the cathode [118, 240, 241] for the whole temperature range. Besides elevated temperature, overcharging is critical for the stability of the cathode. Voltages beyond 4.2 V for LCO and 4.3 V for NCA caused cobalt and nickel to deposit at the anode [171, 220]. Transition metal dissolution can be found for calendar and cyclic aged cells. Stiaszny et al. detected with ICP-OES concentrations of cobalt, nickel and manganese that were 3.7 – 5.4 times higher than in the pristine cell for cyclic ageing [44] and 2 – 2.4 times higher for calendar ageing [45]. Bach et al. [167] found higher manganese concentration in the regions where lithium plating occurred. Thus ICP-OES is also suitable to identify inhomogeneous concentrations, although not in a high resolution. Therefore, it is used in this work to identify possible temperature-dependent differences in SEI thickness via the concentration of lithium and phosphorus. Additionally, the concentration of cobalt, nickel and aluminium is assessed to detect the occurrence of cross-talk.

Scanning Electron Microscopy

A precisely focused electron beam is moved line by line over the sample's surface during this imaging technique giving the scanning electron microscopy (SEM) its name. The entire measurement set-up is placed in a vacuum. Depending on the type of interaction between electrons and sample material, different signals can be detected. The most commonly used signals are those of the secondary electrons (SE), backscattered electrons (BSE) and the characteristic X-ray emission. Secondary electrons are ejected from the valence bands of the atoms after interactions with beam electrons. They have low energy and originate from the first nanometer of the sample surface [242]. The intensity of the detected signal depends on the topography, and edges appear brighter than flat surfaces. Electrons that originate in the beam and are reflected at the surface are high-energetic backscattered electrons. The heavier the sample material, the more electrons are reflected and the brighter the image appears. For energy-dispersive X-ray spectroscopy (EDX), high accelerating voltages are applied so that the beam ejects electrons from inner shells. The electron from

an outer shell fills the hole and emits characteristic X-rays. Therefore, EDX is element-specific. A very local resolution and, thus, detailed imaging of specific structures is possible. Some SEMs achieve resolutions better than one nanometer. The higher the energy of the electron beam, the larger the range of excitation. The analysis method requires the samples to be conductive. Otherwise, they become charged by the electron beam, and the image becomes blurry over time. If battery electrodes are examined, this requirement is fulfilled. Other sample materials can be sputtered.

Inherently, SEM-imaging is highly effective for detecting changes occurring on the active material surface during ageing. In particular, the morphology of the SEI on the anode surface becomes observable. It spreads and becomes thicker over ageing [7, 118, 129, 184] and is not uniformly distributed but covers some graphite particles only partially [158, 243]. Klett et al. [184] found further deposits between the graphite particles. Besides the SEI, cavities on the graphite or delamination are observed and attributed either to solvent co-intercalation or gas formation [129, 158]. Friesen et al. [129] realised bright spots which mark regions with static electric charge indicating a poor electric conductivity of the surface layer. The surface of the cathode is altered much less [7, 118]. At elevated temperatures, also agglomerates form, which appear as small round deposits [117]. The mechanical stress leads to particle cracking, especially at high C-rates and gaps in the secondary particle structure [22, 206, 210]. SEM provides a reliable tool for obtaining a large-scale overview of the electrode surface and observing global and local changes. Thus, SEI formation and occurrence of plating is detected in this work and conclusions about their homogeneity can be reached.

X-ray Photoelectron Spectroscopy

X-ray photoelectron spectroscopy (XPS) is an element-specific analysis technique in which X-rays eject photoelectrons from the inner atomic orbitals. The kinetic energy of the electrons directly indicates the binding energy of the electrons and is characteristic of the atom. It can even be determined from which orbital the corresponding electron is emitted. This allows determining the chemical state of elements and the surface composition within a depth of about 10 nm. Figure 7 shows the overall C(1s) and F(1s) spectra in black that are

deconvoluted and the smaller peaks indicating the chemical bond with its binding energy [244]. The scan is performed on an ellipsoidal area with an axis length of about 400 µm. The detector is adjusted for specific kinetic energy ranges. Thus, on the one hand, a survey spectrum can be acquired over a wide energy range and, on the other hand, a specified smaller range of binding energy can be covered with a higher resolution. The theory and technique are comprehensively outlined by Vickerman et al. [245].

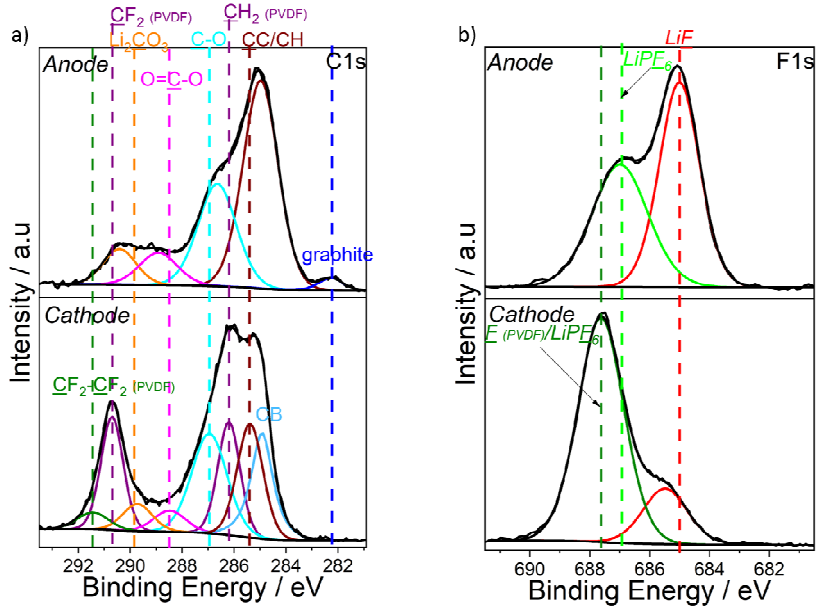

Figure 7. C(1s) and F(1s) spectra with peaks for different chemical states at characteristic binding energies.

XPS is one of the few methods to study the SEI and the decomposition products on the anode surface [172] and to determine the chemical composition of the covering layer. Therefore, it is employed here to identify the SEI components and how they and their concentration depend on temperature.

In the C(1s) spectrum in Figure 7 a), the characteristic peak of graphite of the anode active material is located at 282.5 eV. The three peaks at 286.2 eV (CH_2), 290.7 eV (CF_2–CH_2), and 291.8 eV (CF_2–CF_2) are evidence of components of the binder consisting of polyvinylidene fluoride (PVDF) at the cathode surface. The four other components at 285.4 eV (C–C/C–H), 286.8 eV (mix of C–O/ROLi), 288.5 eV (C=O) and 290.0 eV are associated with Li_2CO_3, which is present due to electrolyte degradation and a component of the SEI. Always present in the cathode is carbon black, with the characteristic peak at 284.9 eV. The F(1s) spectrum in Figure 7 b) displays two components, one located at 685.0 eV indicating LiF and one located around 687.1 eV, indicating the presence of P–F bonds that correspond to the conductive salt. At the cathode, an additional peak arises that is associated with CF_2–CH_2 from the PVDF binder. This peak assignment is performed in the same way for all other elements present in a sample. In literature, different compilations can be found on which binding energy is associated with which element and SEI component [179, 246]. When interpreting the spectra, the composition of the sample must be coherent. The conducting salt, for example, appears both in the F(1s) spectrum and in the P(2p) spectrum.

The constituents of the SEI are mainly RCH_2OCO_2Li, RCOOLi and LiF for the outer SEI and mainly Li_2CO_3, Li_2O and LiF for the inner SEI [185]. With combined depth-profiling, XPS can reveal that the SEI thickness increases for aged cells [206, 243]. The amount of Li_2O and Li_2CO_3 increases during cycling [219, 243], while LiF is getting more dominant for elevated temperatures [206]. Also, at high temperatures, unstable components convert to Li_2CO_3. However, the onset temperature highly depends on electrolyte composition [179]. Jung et al. [181] found the fluorine and carbon elements on the SEI to decrease with cycling, whereas oxygen increased. XPS measurements also reveal a partial dissolution of the SEI during operation [247, 248]. Theoretically, XPS measurements are possible at the cathode. Still, one challenge there is to differentiate surface layer components because PVDF binder and conductive carbon black have very similar binding energies [214] as decomposition products.

2.8 Interim Conclusion

The review of the current literature has demonstrated that temperature has a tremendous impact on lithium-ion batteries. The influence of the temperature level is well studied, as well as the internal heat generation and the shares contributing to it. There are studies on temperature inhomogeneities that suggest that they affect ageing behaviour. However, no conclusions have been reached about their quantitative impact or what mechanisms they induce. It is evident that temperature influences or provokes ageing mechanisms. Therefore, it must be assumed that this also leads to local differences in the presence of temperature inhomogeneities. Especially as many of them are inhomogeneous anyhow. Furthermore, many complementary analytical techniques have been established in battery research that allow identifying many of the ageing processes previously addressed.

However, no maximum temperature difference can be derived from the literature results – neither for single cells nor for interconnections. Moreover, even the publications that explicitly mention a value of 5 K as maximum temperature difference for packs do not provide any reasons or cite other publications, which in turn do not offer any arguments. Yet, reasons to set a limit, in general, are clear. Significant temperature differences could reduce performance and capacity during operation, have an adverse effect on lifetime or even lead to safety-critical conditions. In this situation, 5 K seems like an arbitrary definition because it is not known better, and the above is to be avoided. Thus, the questions posed in this thesis can contribute to filling this gap in research by providing more insight into the effects of temperature inhomogeneities.

3 Concept and Procedure

The experiments in this work are conducted to answer the research questions posed at the outset and shown again in Figure 8.

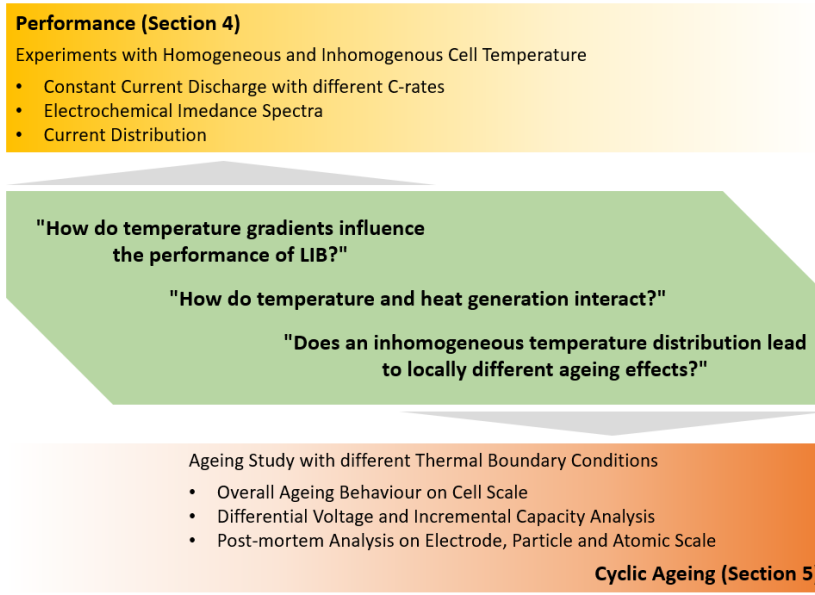

Figure 8. Research questions of this thesis and the experimental methods to approach the answers.

To evaluate how the performance changes with temperature gradients, the cell is discharged and charged with different constant current rates and with various thermal boundary conditions applied. Additionally, electrochemical impedance spectra are recorded under similar thermal conditions. Furthermore, the temperature-dependent current distribution is assessed by two methods. First, a new approach is developed to determine it on a single cell. Then the results are verified by measurements with a parallel connection. With both methods,

a correlation for the temperature-dependent current is derived. This correlation is then used with a relationship for the temperature-dependent resistance to calculate how the heat generation depends on temperature.

The second aspect of this work is the influence of temperature inhomogeneities on the ageing behaviour of LIB. For this purpose, cyclic ageing experiments are performed, and the results are evaluated regarding capacity fade, impedance increase and the dominant degradation modes. Subsequently, the cells are opened in a glovebox and examined in detail with different methods, which are presented in Section 3.4.

This chapter discusses the experimental approach to achieve defined thermal boundary conditions in a battery cell, which are necessary to evaluate their influence on performance and ageing. Thermal simulations demonstrate that the internal temperature distribution experimentally attained is suitable to draw profound conclusions regarding the impact of the applied thermal conditions.

3.1 Battery Cell and Test Set-up

The experiments and results presented in this thesis are based on the pouch cell SLPB 8043140H5 from the manufacturer Kokam Co., Ltd., shown in Figure 10 a). Its specifications are listed in Table 1.

Table 1. Cell specifications of SLPB 8043140H5.

Parameter	Value
Nominal capacity	3.2 Ah
Measured at	0.5C, 25 °C
Typical capacity for charge/discharge protocol	3.0 Ah
Nominal voltage	3.7 V
Voltage range	2.7 V - 4.2 V

The high-power cell consists of a graphite anode and a composite cathode comprising NCA and LCO. SEM images of the anode (first row) and cathode (second row) at BoL are shown in Figure 9. In the top-view of the cathode, the

round secondary particles of NCA composed of much smaller primary particles and the LCO particles with a smooth surface are visible. Since it is a commercial cell, the manufacturer does not disclose its components. Therefore, the composition of the electrolyte is uncertain. For the separator, a melting point analysis indicated a melting temperature of about 134 °C (Appendix), suggesting PE as separator applied [223]. XPS measurements confirm that $LiPF_6$ is used as conductive salt and indicate that the solvent is probably ethylene carbonate (EC) and/or DMC. With a typical capacity of 3 Ah, it is a small cell that enables many tests with a wide variety of test conditions. It can be assumed that the temperature influences in this thesis are transferable to other cells but may vary between different cell chemistries and geometries. Still, relevance is given for large cells.

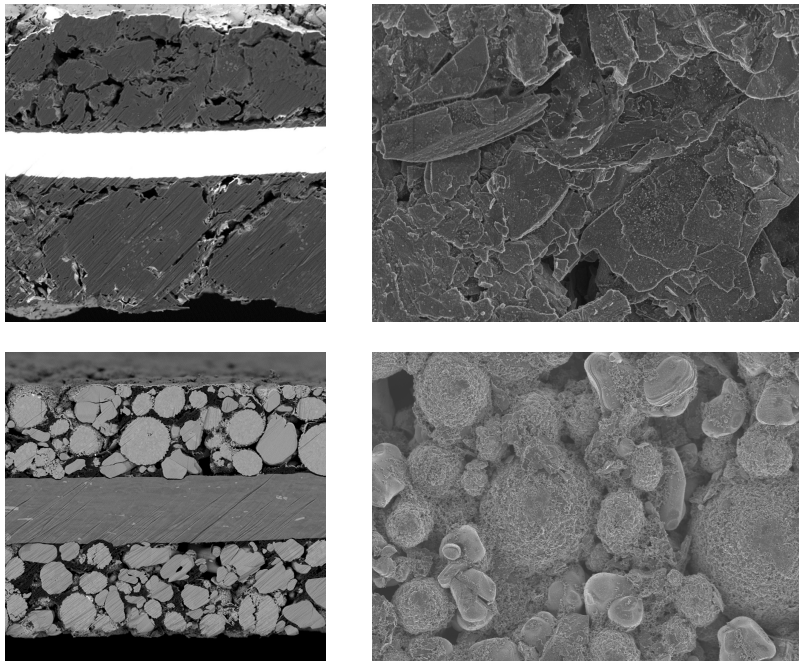

Figure 9. SEM images of cross-sections of the anode (top) and cathode (bottom) and top-views of the surface.

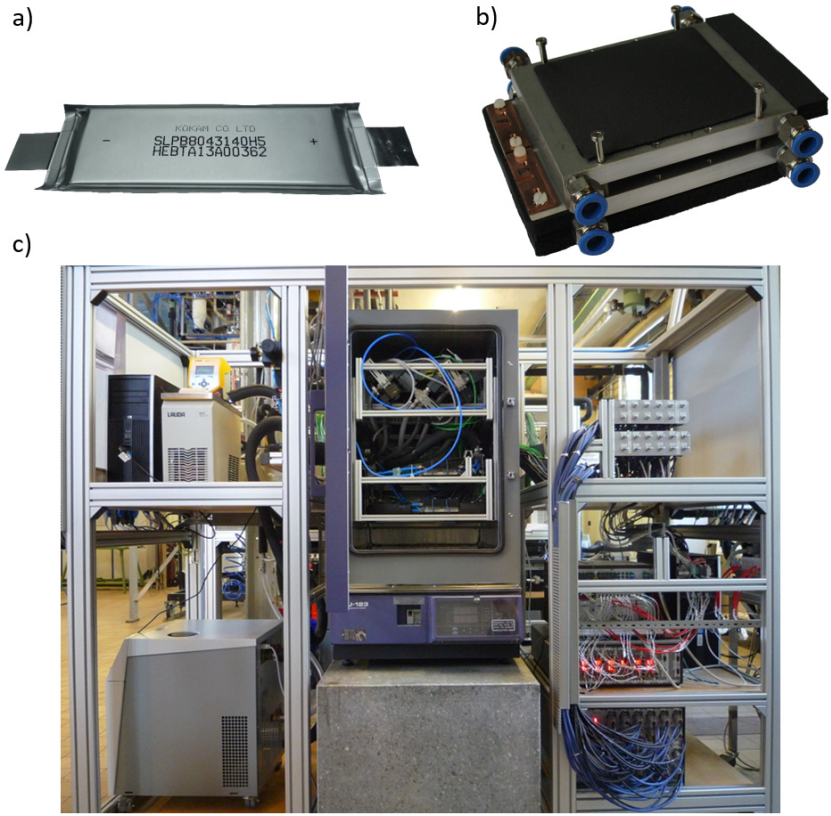

Figure 10. a) Pouch cell investigated in this thesis, and b) a typical cell holder designed for providing constant pressure and defined thermal boundary conditions on the cell surface. c) Test set-up with the safety chamber for cell testing in the centre, on the right the electrical test devices, and left the thermostats for temperature control.

Thermally, the thin aluminium composite foil as housing of the electrode stack has the advantage of enabling direct temperature control. The configuration of opposing tabs provides a more uniform potential and current density and a homogeneous heat generation. The temperature distribution is more even, and the active material is utilised uniformly [73, 249, 250]. As a high-power cell, it has low heat generation during cycling as the layers are thinner and the resistance lower than in high-energy cells. Also, the charge throughput during the check-

up procedure does not alter the ageing results. Another advantage is that the cell is also used in other projects, so it is well characterised, and fully parameterised thermal models are available [251, 252].

To ensure precise temperature control and reproducible conditions for each test, cell holders were designed (Figure 10 b)). The cells are clamped between two aluminium heat transfer plates, and springs provide a constant pressure onto the cell of 3.3 N/cm^2. The cell holders are equipped with reproducible electrical contacting. In the plates, channels for fluid flow at the edges of the electrode stack close to the tabs enhance the heat transfer. They are supplied by thermostats and cryostats, which guarantee good temperature stability. The temperature is controlled both at the surface and tab to achieve the external boundary conditions within the cell as defined as possible. With this set-up, the temperature of the cells can be controlled either homogeneously or inhomogeneously. The inhomogeneous boundary conditions are achieved by fluids at different temperatures that flow through the respective channels on opposite sides of the same plate. The temperature gradients in this work are imposed along the length of the cell. A linear temperature gradient develops in the heat transfer plate between the two temperatures defined by the fluids.

Several thermostats and cryostats from Lauda Dr. R. Wobser GmbH & Co. KG [253] realise the thermal boundary conditions. For the temperature measurement, thermocouples type K and measuring modules from National Instruments Corp. are implemented, which are always calibrated beforehand to increase the temperature measurement accuracy. Temperatures are measured both at the cell surfaces and tabs for monitoring and control. For (dis-)charge processes, test devices from BaSyTec GmbH [254] are used, depending on the desired current rate, either a CTS Lab with higher accuracy or a XCTS with a higher current limit. The electrochemical impedance spectra are measured with an electrochemical workstation from Zahner-Elektrik GmbH & Co. KG [255] in galvanostatic mode with a current amplitude of 1 A and a frequency range of 25 mHz to 100 kHz. They are tested for validity with the LinKK tool [40] provided by IAM-ET at KIT [256]. The interaction of the devices and their software is controlled, when reasonable, via LabVIEW to enable automated test sequences. To prevent environmental effects, the experiments are carried

out in a safety chamber LU-123 from ESPEC CORP or thermally insulated safety boxes. The current measurements on the parallel connection are performed with the digital power meter WT333E from Yokogawa Test & Measurement Corporation [257] via shunt resistances. Figure 10 c) shows the complete test set-up with the safety chamber containing the cell holders in the centre, the thermostats for the fluid supply and temperature control on the left. On the right-hand side, there are the electrical measurement devices and their interconnections.

3.2 Testing and Evaluation Procedure

Before the actual tests are conducted, each cell is pre-conditioned with several cycles at 25 °C with a current of C/5 [68]. The standard capacity, e.g. for adjusting the SoC, is also measured at 25 °C and a current of C/2, while the qOCV is measured at C/20. In both cases, the cell is charged previously to a SoC of 100 % with a constant current – constant voltage (CC-CV) charge protocol.

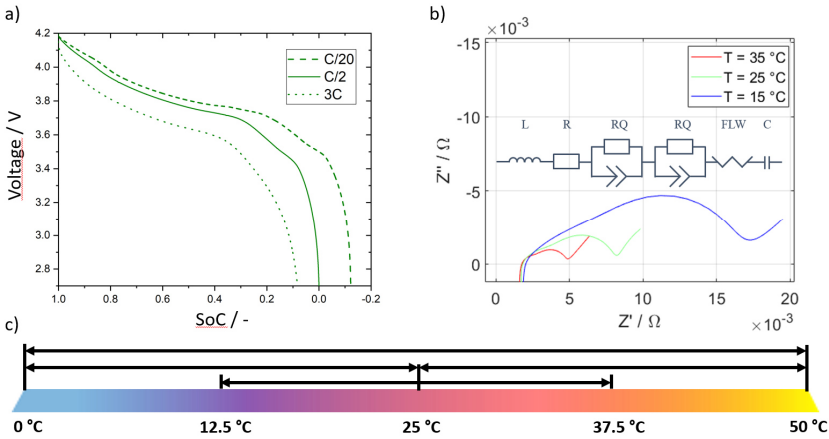

Figure 11. Characteristics of the investigated cells: a) discharge at 25 °C and different C-rates and b) impedance spectra at different temperatures and 50 % SoC with the ECM used for fitting. c) Temperature range with considered temperatures and gradients.

The C-rates considered in this work (Figure 11 a)) are mainly C/20 as qOCV and C/2 as standard current. Additionally, a current of 3C is used in the cyclic ageing tests and to evaluate the behaviour at a higher current. In each case, complete cycles are performed between the voltage limits given in Table 1. Figure 11 b) exemplifies the impedance spectra at 35 °C, 25 °C and 15 °C and displays the increasing resistance, especially the polarisation resistance, with decreasing temperature. Additionally, the ECM to fit the data and to evaluate ohmic and polarisation resistance is depicted. To calculate the heat generation in Section 4.4, the real parts of its individual elements are added up.

Given the objectives of this thesis, there is a distinct variation in the temperature boundary conditions. The temperature range between 0 °C and 50 °C is covered and schematically shown in Figure 11 c). The commonly applied temperature of 25 °C serves as reference temperature and basis of comparison. These three temperatures allow the temperature range to be divided symmetrically with average temperatures of 12.5 °C, 25 °C and 37.5 °C. With the combinations 0 °C/25 °C, 0 °C/50 °C, 12.5 °C/37.5 °C and 25 °C/50 °C, very high temperature differences are applied between the cell edges. Thus, a linear temperature gradient of 222 K/m or even 444 K/m is achieved. In this context, the expression *temperature gradients* refers to the defined temperature differences over the length of the cell.

Concerning reproducibility, it has to be noted that it is not common in battery research to work with systematically determined uncertainty figures. Even though there can be high deviations between cells [258] and a reliable prediction is barely possible even with a large amount of data [259]. One reason is the huge effort to perform a sufficient number of tests to obtain statistically meaningful results due to the required infrastructure and numerous influencing factors. However, without the uncertainty of a measurement being specified, the validity of the result is diminished. To tackle this issue – at least to some extent – all experiments are conducted on at least two cells. For example, in the ageing study (Section 5), all boundary conditions are applied to two cells. The impedance measurements (Section 4.2) at homogeneous temperature control used for parameterisation are performed at least four times per SoC-temperature combination. The measurements of the current distribution using the

parallel connection are conducted with two different cell sets of three cells each. Moreover, new cells are selected for the respective test series to guarantee comparability. The cells exhibit only a very slight deviation [68], probably due to manufacturing tolerances. The reproducibility of the measurements with the experimental set-up is guaranteed, and the reliability of the results is increased as far as possible. However, a systematic uncertainty analysis following GUM [260] is hardly manageable, as cells change with time and depending on measurement conditions.

The cyclic ageing tests are conducted with charge-discharge cycles with 3C constant current. During the check-ups, qOCV, standard capacity, pulse resistance, and impedance spectra are recorded at 25 °C. For evaluating the capacity fade, the qOCV is employed since the influence of the changing impedance is not altering the measured capacity for the low C-rate. Based on qOCV, DVA and ICA are obtained, and their changes during the ageing progress are analysed. The impedance spectra are fitted with a simple ECM shown in Figure 11 b). The increase of resistance – ohmic, pulse, and polarisation – and the capacity fade are used to quantify the ageing progress depending on equivalent full cycles (EFC). EFC is the charge throughput during cycling normalised to the standard capacity at BoL.

The design and construction of the test set-up to achieve the desired boundary conditions is part of the PhD Thesis of Daniel Werner and already jointly published [68]. Thermal simulations are conducted and presented in the following to evaluate to what extent these external conditions prevail within the cell stack. Once this is shown, the results can be correlated with the boundary conditions applied externally.

3.3 Internal Temperature Distribution

Internal temperature measurement in operating cells is not possible without the risk of altering their behaviour. To obtain an understanding of the internal temperature distribution and to verify that the externally applied boundary conditions dominate internally, thermal simulations are performed in Deal.II [261,

262]. Therefore, an already available, well-parameterised thermal cell model [252] is used. A magnified section of the implemented geometry is shown in Figure 12 a). The cathode tab and current collectors are depicted in beige, while the anode current collectors are shown in red. The spaces resulting from the T-shaped tab structure between the cathode tab and the anode layers are parameterised as thermally insulating layers. Active material and separator are homogenised (blue) as they have similar thermal material properties, while the current collectors with their high thermal conductivity are resolved. The boundary condition of the simulation equals its initial condition and corresponds to the experimental boundary condition. The constant temperature gradient is implemented with a Dirichlet condition at the upper and lower surface of the cell stack without considering the pouch foil.

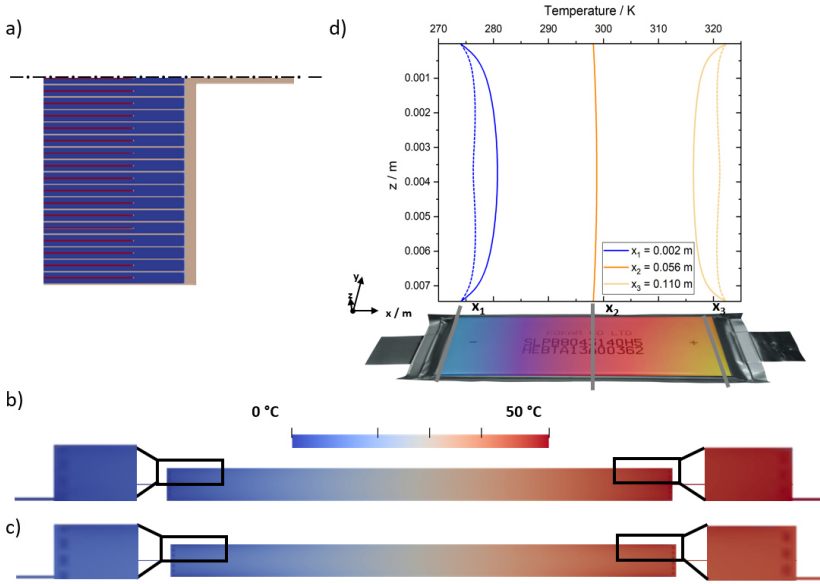

Figure 12. a) Magnified section of the cell stack implemented in the thermal model. Simulated temperature distribution for an applied temperature gradient b) without and c) with temperature control at the tabs. d) Temperature profiles over the cell thickness for cases without (thick lines) and with (thin lines) temperature control at the tabs.

Two scenarios are simulated to evaluate the influence of the temperature control at the tabs, one with an additional Dirichlet condition at one side of the tabs and one with adiabatic tabs. Then the temperature-dependent heat generation (cp. Section 4) that corresponds to 3C is applied in the active material. The temperature distribution is simulated for an average temperature of 25 °C, first at a homogeneous temperature and second with a gradient between 0 °C and 50 °C. The results are evaluated when the steady-state final condition is reached. The heat generation causes negligible warming of the cell stack. In the case with homogeneous temperature control only at the surface, the maximum temperature is 25.66 °C in the centre.

Figure 12 b) and c) compare the temperature distributions with an applied gradient of 0 °C – 50 °C with and without temperature control at the tabs. The images reveal a very similar distribution, with no discernible differences in the centre. Closer to the tabs, red and blue are brighter when the tab temperature is not controlled (c), visible in the enlarged sections, which means the cell stack is less warm and less cold, respectively. This is due to the high thermal conductivity of the metal current collectors, which leads to a high effective thermal conductivity parallel to the layers. The results are evaluated in more detail based on the temperature profiles over the cell thickness in the centre and at both ends 2 mm from the edge of the electrode stack. The profiles in Figure 12 d) reveal the effect of the temperature control at the tabs more clearly. Both, the warm and cold edge are kept closer to the desired temperature of the boundary condition. The maximum slope in the temperature profile is 10.9 K/m directly at the cell surface and drops to just 0.8 K/m in the cell stack 1.5 mm from the surface. In contrast, the maximum slope for tab cooling is only 3.8 K/m and thus two orders of magnitude smaller than the slope along the length of the cell. The cooling (warming) effect of the tab is apparent in the centre, indicated by a slight minimum (maximum). There the tab is closest to the current collectors, and the heat transfer path is shortest. The current collector layers themselves are not discernable. Overall, the additional temperature control of the tabs, as realised in the experiment, provides an internal temperature distribution that follows the defined boundary conditions on the cell surface. Therefore, the assumption of a linear temperature gradient over the length of and throughout the cell stack is proven.

3.4 Inhomogeneous Ageing

The electrical characterisations in the check-ups during the ageing study document the overall changes via capacity fade and impedance rise during the ageing progress. Inhomogeneous ageing mechanisms that lead to changes in the voltage characteristic can only be identified to a limited extent with DVA. On the sealed cell, it is possible to detect whether a considerable amount of gas is present, and an increase in cell thickness enables conclusions whether surface layers or particle fracture occurred in the cathode [233]. The thickness of the investigated cells is measured with a gauge from Käfer [263] before and after ageing. It is not expedient to acquire computer tomography (CT) images of the entire cell since it is too large to obtain a resolution at which details are discernable. Significant deformation of the electrodes is not possible in the sealed, vacuumed pouch foil. To reveal fundamental mechanisms and ageing inhomogeneities, a post-mortem analysis is conducted to infer local ageing mechanisms at the electrode and particle level. The ageing effects detected can be attributed to the electrodes and related to the overall capacity fade and impedance increase. Besides the aged cells, a cell in its initial state (BoL) is opened and characterised with all methods used, and the results are compared with those of the aged cells under the different boundary conditions.

For comparability, all cells are discharged before opening with a C-rate of C/20, then C/40, followed by a CV phase at 2.83 V, which corresponds to the relaxation voltage at BoL after complete discharge to 0 % SoC. Following this procedure suggested by Kobayashi et al. [219], the influence of overpotentials due to different impedance rises is reduced. The cells remain in their regular operating window and are not completely discharged to 0 V to avoid material changes unrelated to ageing [172]. A comparison of the capacity before cell opening with that from the last check-up ensures that no further changes have occurred over time. Then, the cells are opened in a glovebox under an inert gas atmosphere of argon with ceramic tools to avoid short circuits. All tools and parts required in the glovebox into which water can diffuse are dehumidified at 60 °C for at least eight hours before use. Anode and cathode sheets are separately washed in DMC for about two minutes to remove residual conducting salt, following the recommendations from Waldmann et al. [172]. Then the

electrodes are dried, and the samples are prepared according to the requirements of the subsequent analysis.

Electrode Weight and Thickness

To determine the area-specific weight of the electrodes, five electrode coins with a diameter of 20 mm are stamped out with a punch. They have a defined area so that their weight can be compared. They are ejected from the glovebox, weighed on a precision scale, and the mean value is calculated. Subsequently, the thickness of the double-coated electrode is carefully measured on those coins with a digital indicator from Mitutoyo [264]. The results of this mechanical gauge were verified for the electrode thickness at BoL with a thickness evaluation from the SEM images of the cross-sections.

Half-cells

Anode and cathode samples are separately measured against lithium. This setup is further referred to as half-cells as it is common in literature. For this purpose, the standard test cell ECC-Std from EL-Cell is employed [265, 266]. First, the active material is detached on one side from the current collector with NMP, and electrode coins with a diameter of 17 mm are punched out. Also, coins with a diameter of 18 mm are punched out of a 2 mm thick lithium foil. Both coins are assembled, separated by a glass fibre separator, 1.55 mm thick and 18 mm diameter, and soaked with 250 µl 1M LiPF6 EC/DMC solution as electrolyte. From cells aged with temperature gradient, coins are extracted from the cold and warm edges to identify potential inhomogeneities in the electrochemical behaviour.

Table 2. Capacity, area, and a current of C/20 for the Kokam SLPB 8043140H5 and the experimental cells.

	Capacity / mAh	Area / mm^2	C/20 / mA
Kokam	3,000	279,510	1,500
EL-Cell	2.436	226.98	0.1218

After assembly, the half-cells are cycled with C/20, C/5, and C/2 between the cut-off voltages of 3.0-4.3 V and 0.01-1.0 V for cathode and anode, respectively. As it is unknown which voltages versus Li/Li^+ the electrodes have in the commercial cell, those values are based on a broad literature review [120, 185, 194, 206, 212, 228, 241, 267, 268] and selected considering that no additional damage should be induced. For graphite, the capacity difference is only 15 µAh when the upper cut-off voltage would be changed to 1.5 V. This extra capacity is negligible and not worth the risk of damaging the anode material. In addition, the voltages of the individual electrodes were measured in full-cell configuration with lithium reference in a PAT-Cell housing from EL-Cell. Those are within the specified voltage range.

The current related to the C-rates is based on the area-specific capacity of the cathode, as it is smaller than the anode. It is calculated with the total cathode area and the capacity of the Kokam cell to 0.01073 mAh/mm^2. Those values are given in Table 2. The evaluation of electrode capacity and DVA is achieved using the data of the second C/20 curve if it shows no evidence of artefacts. Otherwise, the alternative experimental cell or the first C/20 cycle is evaluated.

SEM

SEM micrographs are taken of both electrodes from the surface and a cross-section. Approximately 5 mm x 5 mm sections are cut out of the electrode using ceramic scissors. Those are transported to the microscopes in glass vials with rolled rim and snap-cap sealed with Parafilm. They are only opened shortly before the sample is transferred into the device, so the air exposure remains as short as possible. Own observations prove that brief contact with air is not critical for the imaging, which is consistent with literature [227, 228] and was confirmed in discussions with project partners, even for samples with substantial lithium plating. The surface is analysed with a SE detector (secondary electron) and an accelerating voltage of 2 kV with magnifications between 10 000-60 000, depending on the detail. First, overview images are taken with lower magnification, then zoomed in, and close-up images are obtained of individual particles and conspicuous structures.

Before the cross-sections are examined, the surface is polished with an ion beam milling system from Leica Microsystems [269] to achieve a planar surface. Therefore, argon ions are accelerated with a voltage of 6 kV and remove the outermost surface mechanically. In the hard tabs and cathode particles, grooves from this treatment are visible in some locations. The cross-section images are taken with a magnification of 1,000 – 3,000 with a back scattered diffraction (BSD) detector and an accelerating voltage of 5 kV.

XRD

XRD spectra are measured on powders. For this, the cathode active material is carefully scraped from the current collector with a scalpel. The obtained powder is filled in glass vials with rolled rim and snap-cap and sealed with Parafilm. The samples are transferred to the D8 Advance-diffractometer by Bruker [270]. The X-rays have a wavelength of 1.51484 Å as they originate from a copper source. The diffractometer is build up in a Bragg-Brentano arrangement. It covers angles in the range of 10° to 90° divided into 7820 steps, with an acquisition time of 3 s each. Directly after the measurement, the background noise is subtracted, and the $K\alpha 2$ separation is conducted. This data consisting of angle and intensity is evaluated with a Matlab routine, which was mainly developed in the bachelor thesis of Leonie Pfeifer [271]. It calculates the lattice parameters a and c as well as the ratio of the peaks (003)/(104), which indicates the crystal structure. This calculation was verified with XRD measurements at different SoC as literature data is available for comparison [272, 273].

ICP-OES

Before the actual measurement, acid digestion is conducted to bring the components of the sample into solution. Graphite is partially digested, and all other elements are dissolved using a microwave system from MLS Application. Two 20 mm diameter punched pieces weighing 75 mg – 77 mg are used from each cell, and duplicate determinations are performed on two cell samples. In addition to the samples, two acid blanks were also measured to avoid allocating any impurities to the samples. The acid digestion is carried out with 6 ml HNO_3 (65 %), 1 ml H_2O_2 (30 %), and 1 ml deionized water. An immediate reaction

with the samples takes place. Therefore, it is necessary to wait briefly before sealing the containers and placing them in the microwave system. This operates a three-step program for graphite digestion with temperatures between 260 °C and 220 °C and powers of 700 W – 1,000 W, with the pressure rising to about 30 bar. This procedure takes 36 minutes, and then the samples have to cool down first. A dark, bluish supernatant (liquid) with a black residue of graphite remains. Subsequently, they are decanted into volumetric flasks and with deionised water (MilliQ) diluted to 25 ml.

The actual measurement is carried out with the iCAP 7000 from ThermoFisher Scientific [274]. The solution is dosed and mixed with argon to form an aerosol, which is excited in the measuring chamber with a plasma at up to 900 °C.

XPS

To prevent chemical alteration of the samples by air contact prior to XPS measurement, the samples are mounted on sample holders in the glovebox and introduced into the instrument under constant air exclusion.

The XPS spectra were acquired using a K-alpha spectrometer from Thermo Scientific. The samples were analysed using a micro-focused, monochromated Al Kα X-ray source (1486.6 eV, 400 µm spot size). XPS spectra were recorded with a concentric hemispherical analyser at a pass energy of 50 eV and fit with one or more Voigt profiles with uncertainty in the binding energy of ±0.2 eV, and Scofield sensitivity factors [275] were applied for quantification using the Avantage software package.

On the cathode samples, all spectra were referenced to the CF_2 component originated from the PVDF binder centred at 290.7 eV binding energy. Regarding the anode samples, the spectral calibration was based on the C(1s) peak (C–C, C–H) at 285.0 eV binding energy controlled by means of the photoelectron peaks of metallic copper, silver, and gold, respectively. The fluorine (F1s) spectra were recorded before and after each high resolution analysis to check the absence of any sample alteration under irradiation. To better understand the interaction between salt and solvent of the electrolyte and the electrode materials, the variation of the degradation products of the conductive salt (LiF)

and solvent (Li_2CO_3) are studied on each electrode together with the amount of salt ($LiPF_6$). The calculation of the amounts of LiF, Li_2CO_3 and salt species is described below in Equations 3.1 – 3.2.

$$at.\%LiF = at.\%F(685\ eV) \cdot 2 \tag{3.1}$$

$$at.\%Li_2CO_3 = at.\%C(290\ eV) \cdot 6 \tag{3.2}$$

$$at.\%LiPF_6 = at.\%P(136\ eV) \cdot 8 \tag{3.3}$$

4 Non-Uniform Temperature – Performance

Temperature gradients are potentially critical for the performance of a battery cell. The decisive properties in this respect are the voltage, resistance and current. This chapter aims to systematically approach a definition of a possible maximum temperature difference within the cell that does not alter its performance. Therefore, voltage, impedance and current under different thermal gradients are analysed and related to homogeneous temperature conditions. For the voltage and impedance measurements, the conditions explained in Section 3.2 were applied. The current distribution was measured with a newly developed method, verified with and compared to the current distribution in a parallel connection using different cell sets.

In the later course of this chapter, the heat generation is evaluated depending only on temperature to investigate their interaction.

4.1 Voltage

The effect of temperature and C-rate on the voltage characteristics is known. Now, the influence of temperature gradients compared to a homogeneous average temperature on the voltage characteristics for different currents is investigated here. Figure 13 a) shows voltage characteristics as a function of SoC for a C/2 discharge. For the discharge at homogeneous temperatures, indicated with solid lines, the expected temperature dependence is obtained. Due to the higher resistance and overpotentials at low temperatures, there is a more substantial voltage loss. Those overpotentials become more pronounced towards low SoC when the OCV is steeper and the resistance higher. In this range, there are also the largest deviations of the discharge curves with a temperature gradient (dashed) compared to those with a homogeneous average temperature (solid). In particular, the cell with the gradient between 0 °C – 25 °C has a higher voltage level than the cell at a homogeneous temperature of 12.5 °C.

Similarly, the voltage curve of the cell with the gradient between 25 °C – 50 °C is positioned above the corresponding voltage curve at 37.5 °C. The difference is significantly less than at the lower temperature level, though. At high SoC, the two curves align precisely. In those two cases, the cell with a temperature gradient behaves as if it was at a slightly higher temperature than the theoretical average temperature. In contrast, the curves obtained for an average temperature of 25 °C and a temperature gradient (0 °C – 50 °C and 12.5 °C – 37.5 °C) are slightly below the curve with a homogeneous temperature of 25 °C.

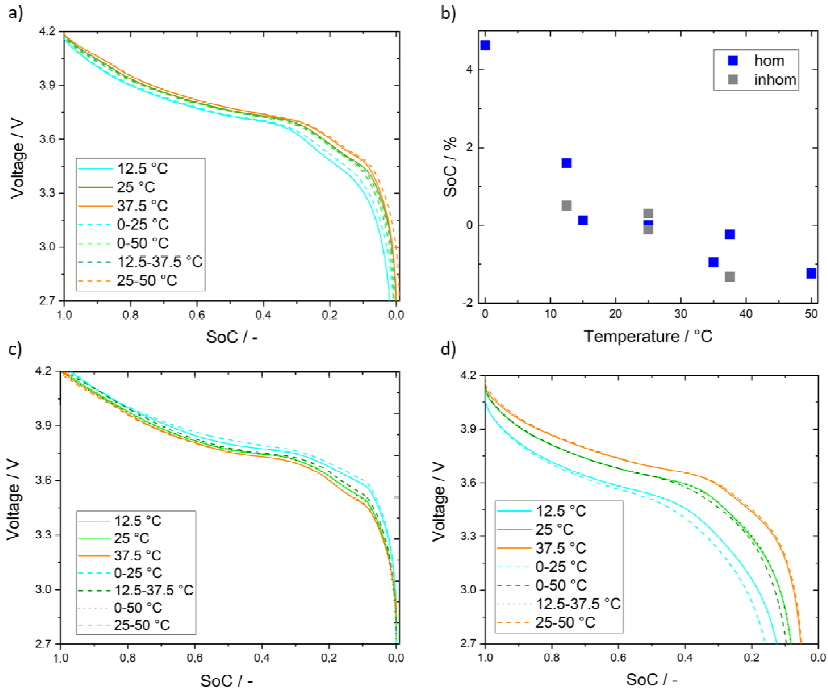

Figure 13. Voltage characteristic at different temperatures with and without gradients for discharge currents of a) C/2 and d) 3C and c) charge currents of C/2. b) Remaining SoC for different temperatures when discharging with C/2.

The consequence of lower resistance and thus lower overpotentials at higher temperatures can likewise be observed in Figure 13 b). It shows the remaining

SoC after a discharge with C/2 until the lower cut-off voltage. A SoC of 0 % is achieved for 25 °C as this is the temperature at which the standard capacity is measured. A negative SoC means that more than the standard capacity could be extracted, which is possible for higher temperatures. While it is evident that the remaining SoC depends on temperature, the influence of temperature gradients is minor compared to the absolute temperature level. Comparing Figure 13 a) and c), the differences between discharging and charging at the same current can be detected. Again, the influence of the absolute temperature appears as expected, with the voltage curves at lower temperatures being above the ones at higher temperatures. However, this difference is less than in the discharge process. This can be explained by the cells having a similar SOC in the steep section of the OCV at the beginning of charging. This changes, but the SoC differences at different temperatures in the flatter part of the OCV have little effect on the voltage curve. Therefore, the impact of temperature gradients is minor too.

At a discharge with 3C, the temperature influence on the voltage characteristic increases as shown in Figure 13 d), as the overpotentials are already higher at higher currents. For average temperatures of 25 °C and 37.5 °C, there is no influence of temperature gradients. Noteworthy is only the voltage of the cell with a gradient between 0 °C and 25 °C, which is lower than the voltage of homogeneous 12.5 °C. A higher current seems to induce a different temperature dependency at low temperatures than a smaller current of C/2. This tendency also applies to charging with 3C, although there, the differences are revealed more clearly as for a C/2 charge.

So far, it can be stated that the influence of temperature gradients on the voltage characteristic is not sufficient to define a value for a maximum temperature difference. On the other hand, there is an influence that might have two possible explanations. Firstly, we assume that the average temperature is the same compared to the homogeneous case. Then, there has to be an asymmetry in how the regions with different temperatures determine the overall behaviour. In areas with a higher temperature, the resistance is lower and, thus, the current is higher. Therefore, both resistance and current depend on temperature and are non-uniform according to the temperature gradient. Then, larger currents

flow through the warm region of the cell, thus giving this part a greater significance and shifting the overall behaviour in the direction of the elevated temperature. This might be valid for relatively low C-rates. Possibly at higher overpotentials at high C-rates, the current that can bypass the cold region is limited, and the resistance that increases exponentially at low temperatures dominates the behaviour. Secondly, the average temperature might differ indeed. If this was the case, the overall heat dissipation within the cell has to be higher for lower C-rates when there is a temperature gradient present. According to Equation 2.2, heat dissipation is influenced by current, resistance and temperature. The higher resistance in the lower temperature region could cause an increased heat dissipation, but at the same time, the current decreases, which leads to a reduction in heat dissipation. Usually, a positive feedback mechanism is assumed for high temperatures, which cause high currents, which again cause high temperatures [48, 59, 75]. However, the interdependencies are complex, so a clear conclusion is not possible at this stage.

4.2 Electrochemical Impedance

The measurement data shown in this section and part of the evaluation used for the analysis were generated and developed in collaboration with Nicolas Kunkel [276] as part of his master thesis.

Along with the voltage, the resistance is decisive for the performance of a battery. To judge the criticality of temperature gradients more differentiated, impedance spectra are recorded over a broad temperature range with and without gradients, and the effects on the spectra are compared. It is known that the impedance strongly depends on temperature. Several authors [49, 50, 52, 64, 277] have quantified this dependency inspired by the law of Arrhenius [60]. This relation was proved to be valid for the investigated pouch cell. The adjustment with the constant parameter R_{col} as in Equation 4.1 was used according to Schmidt et al. [50]. R_{col} accounts for the temperature-independent resistance of the current collectors and improves the fit compared to the Arrhenius law.

$$R(T) = R_{\mathrm{col}} + k \cdot \exp\left(\frac{E_{\mathrm{A}}}{\tilde{R} \cdot T}\right) \tag{4.1}$$

The Arrhenius function in Equation 4.1 is parameterised with impedance spectra at homogeneous temperatures ranging from 0 °C to 50 °C and at SoC of 35 %, 50 %, and 65 %. The measurement data with error bars and the respective fits are shown exemplarily for the polarisation resistance in Figure 14 a). The temperature dependency can be adapted for each SoC with high accuracy and a coefficient of determination R^2 of 0.997 – 0.999. The fit differs for the different SoC. Below 20 °C (293.15 K) and with further decreasing temperature, the fit representing the 35 % SoC is steeper than for 50 % and 65 %. This means that the temperature impact is slightly more pronounced at lower SoC and lower temperature. The influence of the SoC in this range is minor compared to the temperature dependency. Various impedance values can be fitted, and the fit is best for those which highly depend on temperature.

The Bode plot in Figure 14 b) shows the impedance for different temperatures and hatched the SoC range 35 % - 65 % with an additional measurement at 50 %. As expected, the impedance decreases with increasing temperature as well as with increasing SoC. The influence of both variables is stronger at low frequencies than at high frequencies. The same qualitative temperature dependency is shown in the Nyquist diagram in Figure 14 c) for a SoC of 50 %. While the ohmic resistance at a high frequency is practically identical for 25 °C (blue) and 35 °C (red), the impedance of the second semi-circle is significantly lower at 35°C. This is consistent with the observation in Figure 14 b) that temperature sensitivity is high at those lower frequencies. The local minimum minus the ohmic resistance is associated with the polarisation resistance. Given its temperature sensitivity, it can be assumed that temperature inhomogeneities have an impact on this value. Therefore, it is the focus of further considerations regarding the influence of temperature gradients. The dashed spectra in Figure 14 c) were measured at an average temperature of 25 °C with a temperature difference of 20 K and 50 K, respectively. Compared to the spectrum at homogeneous 25 °C, the ohmic resistance and the first semicircle are almost aligned, while the minimum moves towards smaller impedances. Thus, the impedance under temperature gradients responds in the same way as the impedance at a

slightly increased average temperature. However, the impact even of extreme gradients is small compared to the effect of absolute temperature.

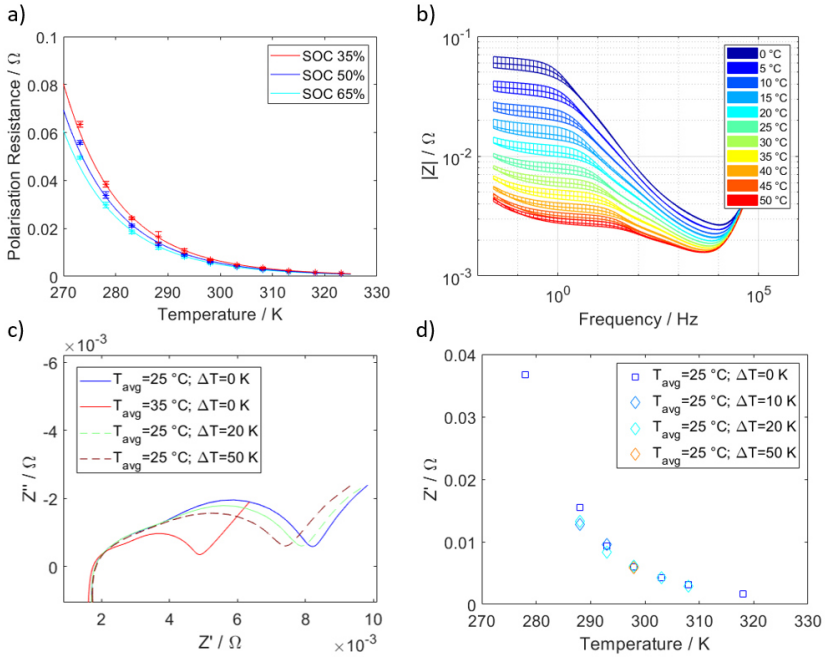

Figure 14. Temperature dependency of a) the polarisation resistance for different SoC and b) the absolute impedance in the Bode plot with additional SoC dependency (inspired by Schmidt et al. [50]). Influence of temperature gradients at 50 % SoC compared to the influence of absolute temperature c) in the Nyquist plot and d) based on the polarisation resistance.

To further elucidate the impact of gradients, the polarisation resistance with different average temperatures and temperature differences is depicted in Figure 14 d). Overall, the characteristic exponential decline of the resistance with temperature is the same as in Figure 14 a). Additionally, the values measured with a temperature gradient are plotted at the respective average temperature. At higher temperatures than 20 °C, the effect is negligible. With decreasing temperature, the polarisation resistance becomes lower with a gradient compared to the homogeneous average temperature. At 25 °C, the deviation in the

polarisation resistance with a temperature gradient of 50 K and a homogeneous temperature is 2.1 %, while it is 14 % for 15 °C with a 20 K temperature difference. Still, the influence of gradients is considerably smaller than the deviation of 47.7 % and 159.3 % in polarisation resistance when the homogenous temperature is increased and reduced from 25 °C to 35 °C and 15 °C, respectively.

The results reveal that the average temperature level is more relevant for the resistance than the homogeneity of the temperature distribution. When frequency ranges are considered where the impedance is less sensitive to temperature, the influence of temperature gradients is equally reduced. This is valid over a wide SoC and temperature range even though the influence of gradients becomes stronger at low temperatures.

A quantitative comparison with literature data is not possible since the results are only specified qualitatively there. In addition, different resistances – ohmic [50] charge transfer [48], pulse or depletion [16] resistance – are used to consider the influence of temperature inhomogeneities and mainly gradients across the layers are investigated. Qualitatively, resistances obtained from EIS and pulse measurements with temperature gradient are also slightly lower than the value for the corresponding average temperature. Similarly, the trend for increasing temperature differences, especially for low temperatures, is qualitatively in good accordance with literature. It can be noted that the polarisation resistance, which was considered here as a representative of the impedance, is susceptible to temperature but is only slightly influenced by temperature inhomogeneities. Concerning the resistance, the overall cell behaviour under temperature gradients is shifted somewhat towards a warmer average temperature. However, similar to the voltage curves, the absolute average temperature is much more decisive.

With the results obtained, the question raised in the previous chapter can be reconsidered as to whether elevated average temperatures or asymmetric behaviour is present. No significant heat generation is expected during the EIS measurement because the sign reversal in the sinusoidal current eliminates the reversible entropic heat source term, and the current intensity of 1 A (C/3) is low for a high-power cell. This means that no increased cell temperature due

to heat dissipation causes the shift, but in fact, an asymmetric behaviour is integrally measured. An asymmetric behaviour has to be the result of the temperature inhomogeneity leading to current inhomogeneity.

4.3 Current Distribution

The results presented in this section are partly published [278]. The experimental set-up for the parallel connection was developed with Lisa Cloos during her Master Thesis [279]. The experiments on the single cell are based on the Bachelor Thesis of Jakob Technau [280] and his work as a student assistant.

Besides voltage and resistance, the current needs to be included for a comprehensive performance analysis. As explained in Section 2, temperature and current are closely related, influence each other and interact strongly. The literature review did not reveal quantitative relations between temperature and current. When temperature differences are investigated, only qualitative results are shown, and no benchmark measurement at a homogeneous temperature is conducted to quantify cell-to-cell variations and wiring impact (cp. Section 2.4).

Therefore, own measurements were performed on a parallel connection, and a compensation was introduced to account for temperature-independent influences on the current distribution. However, in parallel connections, the impact of temperature differences is always measured along with the influence of the absolute temperature, and the system reacts very sensitively to high currents and low temperatures. Consequently, a new measurement method was developed that circumvents these shortcomings and provides reliable results without the influence of cell-to-cell variation and wiring. Based on those, a quantitative correlation is established. It allows a conclusion on how an inhomogeneous temperature distribution impacts the current distribution.

4.3.1 Parallel Connection

A parallel connection with individual temperature control and current measurement is built up to measure the temperature-dependent current distribution. The configuration of three cells in parallel has a total capacity of 9 Ah, to which the C-rates specified hereafter refer. Since even details in the measurement setup can strongly affect the results [281, 282], the same cable lengths and, whenever possible, material bonded contacts were carefully considered. Therefore, the resistance between measuring devices and cells is low and similar for all cells, which preliminary tests have confirmed. An evaluation of all the tests carried out shows a loss resistance that is low enough to be negligible, according to Wu et al. [283]. Temperatures are measured both at the cell surfaces and tabs for monitoring and control. The greatest heat generation occurs at the cathode tab due to ohmic losses [284]. Nevertheless, for C-rates up to 1C, this temperature never deviates more than 2 K from the set temperature, even at 0 °C. Consequently, a homogeneous temperature is assumed for each cell. The system is susceptible to long pauses and charging processes with inhomogeneous temperature control. This is discernible by a noisy current profile, combined with voltage fluctuations. Apparently, both are critical conditions for the system. Additionally, some noise occurs at low SoC, when the OCV gets steeper (below 40 % SoC), and at high C-rates, when the overpotentials are higher. These conditions seem to promote instabilities of the overall system.

The reproducibility of the measurements was examined. When there is no noise, reproducible results are confirmed for the same cells during the plateau phase. It is also not affected if other temperatures are assigned to the cells. Deviations occur with fast current changes, i.e. at the very beginning of the discharge and towards the end when the wavy pattern starts. To consistently ensure reproducible and reliable results, a C/2 discharge at homogeneous 25 °C was performed as a reference before each experiment. They show that the actual capacity of the individual cells depends strongly on the direct history. In particular, the cell measured at low temperatures exhibits strong capacity fluctuations. However, this "capacity loss" is reversible, and with a discharge at a very low current (C/40), the initial value can be recovered. This effect can be caused by extended interruptions, high C-rates, and low temperatures

(< 20 °C) of one or more cells. Most likely, this is related to the internal resistance, which is subject to variations, according to Lv et al. [285]. When using other cells, the results differ significantly but qualitatively follow the same pattern. Those deviations demonstrate the influence of the cell parameters, which can slightly deviate in terms of capacity and internal resistance due to production [77].

The strong impact of cell parameters not only causes variations between cell sets but leads to a non-uniform current distribution even for a homogeneous temperature. In an ideal case, the normalised current referenced to the average current (Equation 4.2) equals unity for each cell *i*. The results for a homogeneous temperature of 25 °C are shown in Figure 15 a). This discrepancy impedes a precise evaluation of temperature effects. Therefore, an adjustment is introduced that eliminates the influences of cell-to-cell variations and allows an assessment of the temperature influence. The correction factor f_i is determined with Equation 4.3 by the ratio of the normalised current with inhomogeneous temperature control and the normalised current with homogeneous temperature control at 25 °C. The normalised current is then modified with this correction factor, which is determined at a SoC of 65 %. The entire current profile is then corrected with this value by a shift along the y-axis (Equation 4.4).

$$I_{i,\mathrm{norm}} = \frac{3 \cdot I_i}{\sum_{i=1}^{3} I_i} \tag{4.2}$$

$$f_i = (65\%, T_i) = \frac{I_{i,\mathrm{norm}}(65\%, T_i)}{I_{i,\mathrm{norm}}(65\%,\ 25°C)} \tag{4.3}$$

$$I_{i,\mathrm{norm}}^{\mathrm{corr}}(SoC_j, T_i) = I_{i,\mathrm{norm}}(SoC_j, T_i) + (1 - f_i(65\%, T_i)) \tag{4.4}$$

It is assumed that the 65 % SoC as a value during the plateau phase represents the temperature influence and that no compensation processes have started yet, as they become visible only from about 40 % SoC by the wavy pattern. To take chronological differences into account and to be able to eliminate them, a standard discharge at homogeneous 25 °C is carried out before each test to correct the subsequent measurement. The correction of the measured values described here was validated using different sets of cells, which can be found in the Appendix. The procedure for measuring the current distribution on the parallel connection is illustrated in the left column of Figure 16.

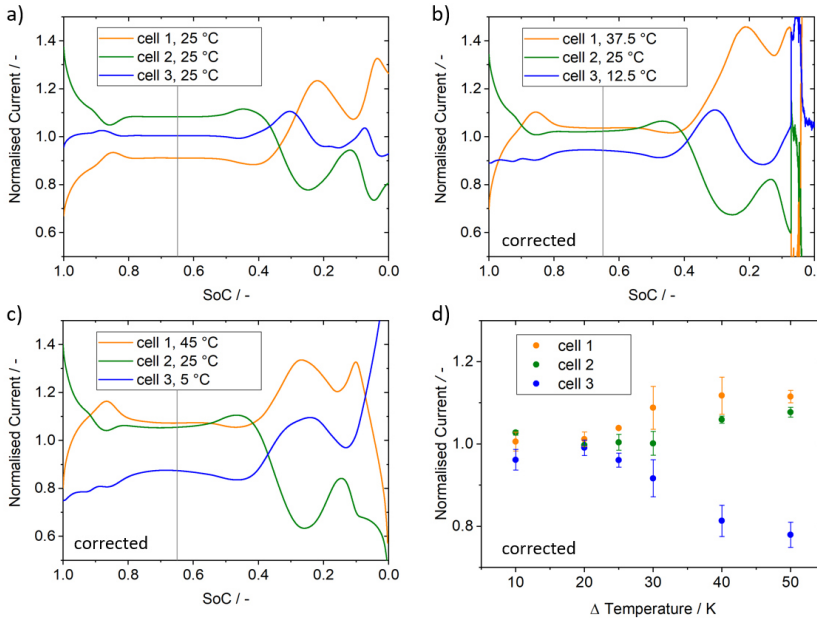

Figure 15. Normalised discharge current in the parallel connection at a mean temperature of 25 °C for a) a homogeneous temperature, b) a maximum temperature difference of 25 K and c) a maximum temperature difference of 40 K. d) Normalised current for different temperature differences at 65 % SoC and an average temperature of 25 °C. [278] (license CC BY-NC 4.0)

Figure 15 shows the current distribution for three cells with a mean temperature of 25 °C and the influence of the temperature difference. In a) the uncorrected current is shown as measured to illustrate the deviation induced by cell-to-cell variations and the set-up. After applying the correction factor, the plateaus are in good agreement (cp. Appendix). Figure 15 b) and c) show that the current distribution gets broader with an increasing temperature difference. The currents for the two warmer cells are similar in contrast to the one of the cold cell, which is significantly smaller. This effect is more pronounced for a higher temperature difference and means that a symmetrical temperature difference does not lead to a symmetrical current distribution. This finding is supported by literature [83]. The asymmetry becomes even more evident in Figure

15 d) in which the normalised current at 65 % SoC is plotted against the maximum temperature difference at an average temperature of 25 °C. A significant impact only becomes apparent above a temperature difference of 25 K when cell3 has 12.5 °C. This is further supported by measurements with the same temperature differences but at different average temperature levels. They also reveal that temperature differences at a low temperature level have a more pronounced effect than at a high temperature level. (Appendix)

Moreover, it is noticeable that the cell current at the low temperature increases sharply at the end of the discharge, while it decreases for the other two cells. This is precisely the case at the SoC, at which the OCV becomes steeper (cp. Section 3.2, Figure 11). From there on, the differences in SoC that have accumulated due to the different currents are compensated to some extent. The fact that even at the end of the discharge, the cell still has a higher SoC at low temperatures is revealed both by a comparison of the measured charge quantity and by the equalising current that flows in the direction of the two warm cells during relaxation. This is consistent with the findings in Section 4.2.1 and literature.

In literature, it has likewise been observed that in parallel connections, a temperature difference leads to a non-uniform current without quantifying this further [83, 89, 98, 100]. Fleckenstein et al. [76] deduce that a higher temperature difference leads to a higher difference in current due to the temperature-dependent resistances for the current distribution within a cell. According to other literature, a higher average temperature leads to a more dynamic behaviour [83, 90] concerning the current fluctuations and a smaller difference in current. The results here show a minor influence for higher but an increasing current difference for lower average temperatures.

The focus of this thesis is on temperature, but to complete the picture, additional tests with different C-rates were performed. Again, the results are broadly consistent with literature, which identifies less dynamic current characteristics for a higher C-rate [83, 85]. This can be attributed to the higher overpotentials that blur the characteristics of the OCV. Concerning current variations, conflicting statements are ranging from decreasing [89] to increasing [88] differences for a higher C-rate. The results obtained here do not show a

clear tendency for currents of C/5, C/2 and 3C, but the noisy measurement data for 3C hinders the interpretation. There is a slight increase in current difference when the current is increased from C/5 to C/2. But it does not significantly change for a further rise to 3C. One can suspect that the current difference above a specific current does not increase further due to higher irreversible heat generation at low temperatures and, therefore, a higher temperature.

During charging, the current distribution fluctuates compared to discharging and responds more sensitively to temperature inhomogeneities. There is no pronounced plateau phase. The steep OCV at the beginning causes high differences in the SoC, which equalise when the flatter section of the OCV is reached. Thus no stable, representative state is reached until the end of the charge. Therefore, no single value can be selected that allows a reliable evaluation of the temperature-dependent current distribution. Also, most studies in literature focus on the discharge process only. Still, it should be noted that the charging is sensitive to temperature inhomogeneities which is especially relevant when fast charging is addressed in applications.

4.3.2 Single Cell Measurement

In this section, a new method is presented, which was developed to determine an equivalent current distribution using measurements on one individual cell. The number of factors influencing and altering the results is reduced by eliminating the impact of cell-to-cell variations and the wiring. With this approach, a current distribution is identified that exclusively depends on temperature. Furthermore, the effort of the test set-up is significantly reduced compared to a parallel connection. For battery testing, usually, a constant current is applied. Now, a voltage curve is measured at a constant current and for different homogenous temperatures. This recorded voltage characteristic is then used as the control parameter during discharge with different thermal boundary conditions. The presented approach allows the current to adapt to the voltage characteristic as a function of temperature.

The experimental procedure is illustrated in Figure 16 in comparison with the parallel connection procedure. The grey shading indicates the step that is performed only once to record the voltage curve. As depicted, the voltage curves were acquired with a constant current of C/2 at different temperatures T, namely 12.5 °C, 25 °C and 37.5 °C. Before the actual measurement, the cell voltage is adjusted with a low current of C/20 to the initial voltage U_{start}, at which the voltage curve starts to avoid current spikes at the beginning. In addition, voltage curves with temperature gradients were recorded, and the influence on the current distribution was determined. The current characteristics during discharge matched those of the average temperature, so they will not be discussed further.

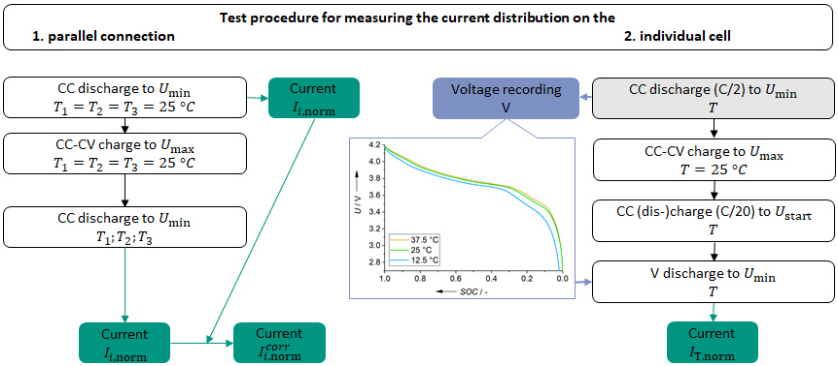

Figure 16. Comparative schematic of the experimental procedure for the parallel connection (left) and the individual cell (right). (adapted from Paarmann et al. [278], license CC BY-NC 4.0)

The evaluation is performed in analogy to the parallel connection based on the normalised current, which is calculated slightly different. The current applied during voltage recording is used as the reference value for the normalisation. The measurement set-up is very robust and provides reproducible results without any noise for a current of C/2. Only at the end of discharge with a 3C current is some noise in the measurement data (Figure 17 d)).

Figure 17 a)-c) show the current distribution during complete discharges at different temperatures in the range of 0 °C-50 °C with the voltage recorded at

12.5 °C, 25 °C and 37.5 °C with C/2, respectively. Figure 17 d) gives the current distribution comparable to b) but with a reference current of 3C. The colours and corresponding temperatures in the legend are valid for all diagrams.

Compared to the measurements on the parallel connection, the temperature is adjustable with finer increments. This is due to the elimination of other interfering factors and the measurement at absolute temperatures instead of temperature differences. The measured currents arrange according to temperature, with the lowest current at the lowest temperature and the highest current at the highest temperature. At the end of the plateau phase, when the compensation begins, the distribution is completely reversed.

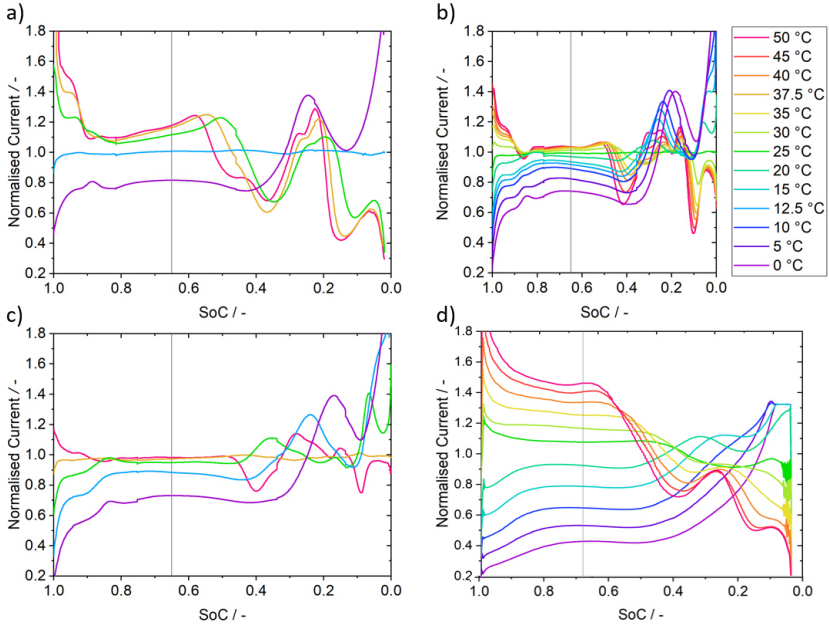

Figure 17. Normalised current measured on the individual cell at different temperatures with a voltage characteristic recorded with C/2 at a temperature of a) 12.5 °C, b) 25 °C, and c) 37.5 °C [278] (license CC BY-NC 4.0) and d) 3C at 25 °C.

The normalised current obtained at the same temperature as the one at which the corresponding voltage was recorded is consistently close to unity and exhibits only slight deviations. This result is expected but gives credibility to the new method. Comparing the distributions for different temperatures during voltage recording, the measured currents for the same temperature and their distribution are very similar and only exhibit an offset downwards for higher temperatures. This offset means that the temperature during voltage recording determines the position of the distribution relative to the y-axis. Additionally, the plateau phases become longer and the wavy shape less dynamic when this temperature gets higher. In all three cases, the current differences at high temperatures are significantly reduced compared to those at low temperatures, despite the same or even considerably larger differences in temperature. Above about 30 °C, the currents in the plateau phase hardly differ and only deviate when the wavy characteristic starts.

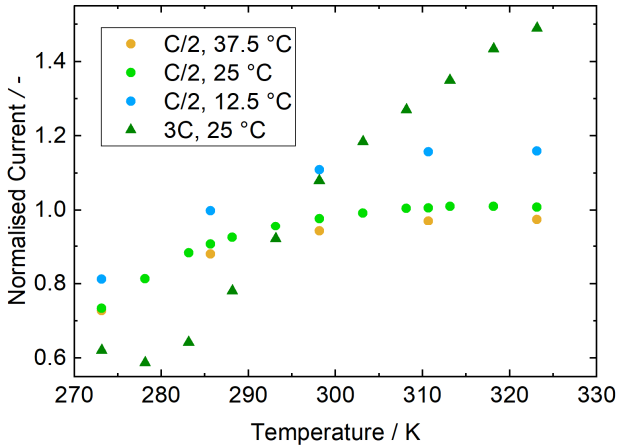

Figure 18. Normalised current at 65 % SoC for C/2 voltage recording at different temperatures and 3C voltage recording at 25 °C.

A different current distribution is shown in Figure 17 d). The voltage was recorded in analogy to Figure 17 b) at 25 °C, but with a current of 3C. The higher current significantly broadens the distribution, and up to the maximum test

temperature of 50 °C, an apparent influence on the current distribution is observed. These findings are revealed more clearly in Figure 18, where the normalised current at 65 % SoC is depicted against the temperature.

The legend gives the temperature at which the voltage was recorded. The results for C/2 as round markers do not show a linear dependency of the current on temperature but a higher temperature influence at a lower temperature level. These findings are in good agreement with the results of the parallel connection. Above a certain temperature, the temperature influence decreases, and the current approaches a maximum value. Thereby the measuring points for a low temperature during the voltage recording are shifted upwards to higher currents. In comparison, the voltage characteristic recorded with 3C causes a considerably greater temperature dependency of the current. The current distribution follows an almost linear, only slightly bent progression, which does not exhibit a maximum value in the relevant temperature range. The reason is the much higher overpotential at the high current. For C/2, the current follows the recorded voltage characteristic close to equilibrium already at about 25 °C. An increased temperature and, therefore, enhanced kinetics and mass transport do not lead to a higher current. In contrast, for 3C, even at high temperatures, overpotentials occur, and a further temperature increase leads to accelerated reactions and enhanced transport properties and thus directly to a higher current. No plateau is established, meaning that even the high temperatures cannot compensate for the overpotential caused by the high discharge current.

In general, a temperature-dependent current distribution can be determined with the method developed here. The temperature of the voltage recording has to be considered when the results are evaluated, which is comparable to the average temperature of the parallel connection. The main advantage is the elimination of parasitic influences on the current distribution and the possibility to measure the current depending on temperature and not on temperature differences. A significant difference lies in the measurement methodology. During the single-cell measurements, the cell remains closer to equilibrium as the current adjusts to temperature and voltage but is not “forced” through the cell. Therefore, no specific current or power is drawn as in typical battery applications.

4.3.3 Temperature-Current Correlation

Based on the results obtained in the previous two subsections, a quantitative correlation between temperature and current is now derived. For this purpose, the measured data for the parallel connection is initially displayed in the same way as for the single cell as a function of temperature. However, the normalised current depends on the temperature difference as well. The asterisks in Figure 19 a) represent this data. Their mean value for the normalised current is unity because each depends on the other currents, and a constant total current is applied as the driving force. The temperature range is limited when different temperature levels with symmetrical temperature differences are examined. Therefore, only an average temperature of 25 °C is considered for the quantification with the parallel connection. The individual cell experiments, on the other hand, are not restricted in this regard. The round markers depicting the data of the individual cell are the same as in Section 4.3.2. The half-filled ones represent the data with the voltage curve recorded with a temperature gradient.

Since the temperature dependency of the current originates mainly from the temperature dependency of the internal resistance, which can be expressed by the Arrhenius law (Section 2.2 and Section 4.2.2), the exponential approach in Equation 4.5 is used to quantify the relationship of temperature and current.

$$I_{\mathrm{norm}} = a \cdot \exp\left(-\frac{b}{T-c}\right) \tag{4.5}$$

The constant coefficients a, b and c are adapted with a non-linear least-square solver to the measurement data. The Kelvin temperature is chosen as it is commonly employed for Arrhenius approaches. The resulting fits are shown as lines in Figure 19 a), with the colours indicating the mean temperature. The solid lines represent the individual cell tests at homogeneous temperature during voltage recording, while the dashed lines represent the current distribution based on voltage recording with temperature gradients. The dotted line gives the fit for the parallel connection. Overall the fits are in good accordance with the measurement data. This is confirmed by the values for the coefficient of determination R^2, which is >0.99 (cp. Appendix) for all cases except the parallel connection.

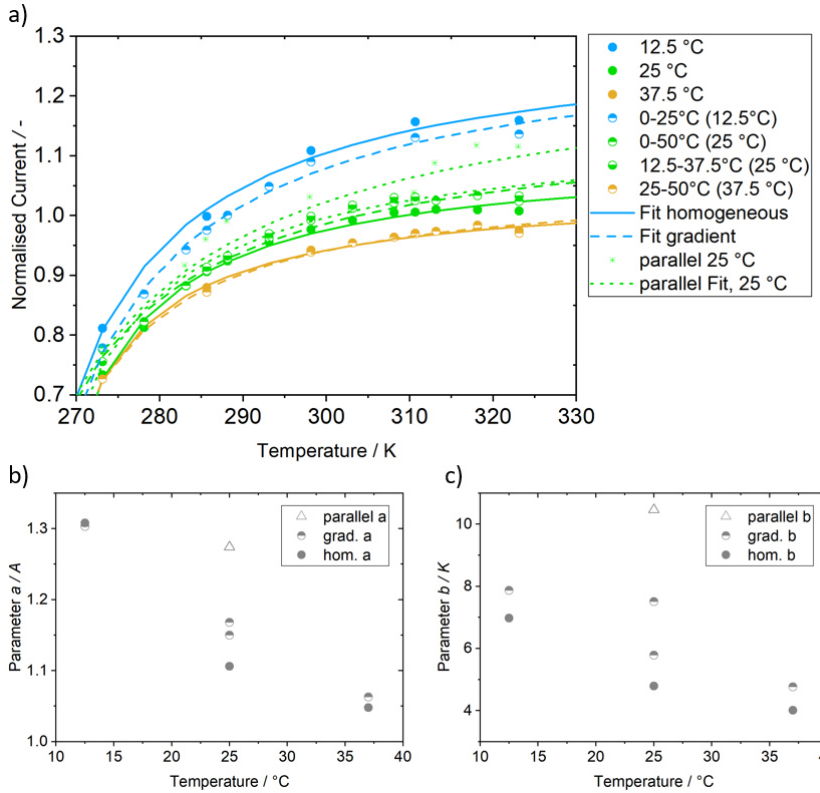

Figure 19. a) Temperature-dependent normalised current at 65 % SoC for the individual cell with voltage recordings at different temperatures with and without gradient and for the parallel connection with the corresponding fit results. b) coefficient *a* and c) coefficient *b* of the exponential equation depending on the average temperature during voltage recording.

In Figure 19 b) and c), the coefficients *a* and *b* are shown as a function of temperature. They reveal an almost linear trend in temperature dependency and slight differences between the individual cell tests with and without temperature gradient and the parallel connection. The coefficient *a* determines the maximum current value towards which the function converges. It decreases with higher temperature during voltage recording. This decline of the limit

value is likewise visible in Figure 19 a). Comparing coefficient *a* for the tests with and without temperature gradient, there is no significant deviation while it is comparably high for the parallel connection.

Coefficient *b* defines the curvature, which decreases for a higher value of *b*. When the voltage is recorded at a lower temperature, the curve is bent more strongly. This is probably due to the higher overpotentials when the voltage is recorded. During the current measurements at higher temperatures, the steeper voltage characteristic further diminishes the minor temperature influence at high temperatures. A temperature gradient during voltage recording leads to a higher coefficient *b* which means less curvature. The fit of the parallel circuit shows the slightest curvature, which can be attributed to the interdependence of the cells' currents. Coefficient *c* (Figure 40.A, Appendix) shows a similar linear temperature dependency as *a* and *b* with minor differences between the tests with and without temperature gradient. Here too, the coefficient for the parallel connection does not quite match the values for the individual cell tests. The exponential current function is only applicable for small C-rates as C/2. Higher C-rates (3C) result in a more linear function in the relevant temperature range. A polynomial of degree two is well suited to fit the data and describe the temperature-dependent current.

In conclusion, a relatively simple function was introduced to characterise the temperature-dependent current distribution. It reveals that temperature inhomogeneities cause non-uniform current distributions, which could be critical for the cell, especially at high currents.

4.4 Heat Generation

In the previous sections, temperature-dependent equations were introduced for the cell resistance and current and parameterised for the investigated cell. With these, the heat source definition introduced in Equation 2.2 in Section 2.3 can be expressed as purely temperature-dependent. Equation 4.6 gives the expression for a current of C/2. As shown in Figure 18 in the previous section, the current distribution for an overall current of 3C is almost linearly dependent

on temperature instead of the exponential dependency valid for C/2. Therefore, the term for the temperature-dependent current in Equation 4.6 must be adjusted for the respective current. This approach enables conclusions to be drawn about whether an inhomogeneous temperature and current distribution may lead to an unexpected critical heat generation that poses a safety issue. For thermal models, this means that coupling with an electrical model is not necessarily required, although a lot of care has to be taken for parameterisation.

$$\dot{Q}(\mathrm{T}) = \left(I_{C/2} \cdot a \cdot \exp\left(-\frac{b}{T-c}\right)\right)^2 \cdot \left(\mathrm{R_{col}} + k \cdot \exp\left(\frac{E_A}{\tilde{R} \cdot T}\right)\right) + \cdots$$

$$I_{C/2} \cdot a \cdot \exp\left(-\tfrac{b}{T-c}\right) \cdot T \cdot \left(\tfrac{\partial U_{OCV}}{\partial T}\right)_{50\%} \tag{4.6}$$

It has to be noted that the parameters for the resistance were determined at a SoC of 50 %. In the range of 35 % - 65 % SoC, the changes in the temperature dependency of the resistance are negligible. Therefore, the coefficients can be used as an approximation, but the function cannot be extrapolated further. Unlike the polarisation resistance, whose temperature dependency was considered before, the sum of all real parts of an adopted ECM is employed to calculate the heat generation. The entropy coefficient $\frac{\partial U_{OCV}}{\partial T}$ for the reversible heat contribution is also determined at a SoC of 50 % using a newly developed method [286]. It is based on the conventional assumption that the entropy coefficient is constant over the temperature range considered [27]. The current function is specified for C/2 and 3C, respectively, and a SoC of 65 %. Looking at the plateau phase, the current distribution is similar for a SoC range between 50 % - 75%. Thus this equation is not generally valid but only in a SoC range of 50 % - 65 %, where resistance and current are parameterised. The parameters are given in the Appendix.

Another limitation of the temperature-dependent function of current distribution is that it is strictly applicable only for the considered case at which it was parameterised. At other average temperatures, the total current taken into account in the calculation is not the same as that used for parameterisation. This is because no closing condition matches the sum of the local currents with the

total current. Thus, the following consideration is based on equilibrium assessments. Still, it is beneficial for reflecting the interaction of temperature and current distribution with heat generation. With the limitations in mind, those interactions can be implemented easily in a purely thermal model to consider them. A suitable example for applying this equation are oscillations around a specified SoC with current pulses.

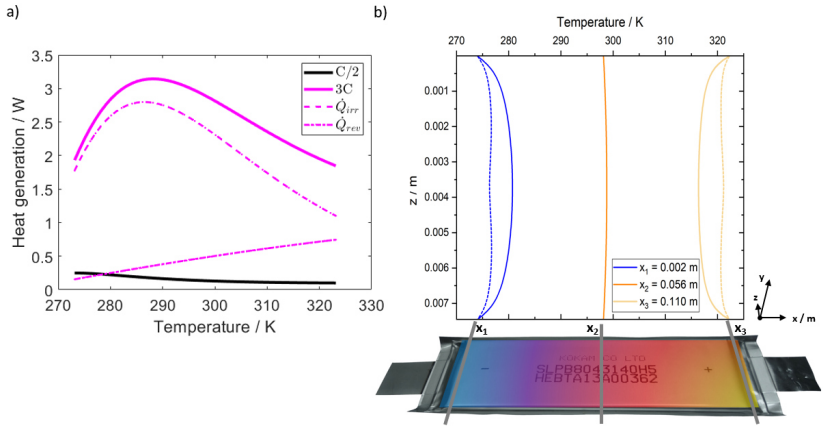

Figure 20. a) Heat dissipated with a current of 3C and C/2 at a SoC of 50 %. b) Temperature profiles across the cell thickness (hot and cold side and centre) at steady-state when a temperature gradient between 0 °C – 50 °C and a current of C/2 is applied.

Figure 20 a) shows the temperature-dependent heat source term calculated with Equation 4.6 for an applied temperature gradient 0 °C – 50 °C. Due to the higher current, the heat generation is far higher for 3C (magenta) than for C/2 (black). For the high current, the heat generation first increases with rising temperature until a maximum of 3.14 W at 288 K is reached. This can be explained by the high resistance at low temperatures, which results in a small current. With a further increase in temperature, the heat generation declines, although the resistance decreases while the current increases. This means, depending on temperature, either the current or the resistance dominates the heat generation. Also, this finding questions the common understanding of a positive feedback mechanism between temperature and heat generation [48, 59,

75]. According to this assumption, current and heat generation would continuously increase with higher temperatures. The dashed curve in Figure 20 a) represents the irreversible heat generation that dominates the overall behaviour at high C-rates. The irreversible heat generation increases with temperature, indicated by the dash-dotted line.

The heat dissipation, shown in Figure 20 a) for two examples, is implemented for different cases in the same thermal cell model [252] as in Section 3.4. The following calculations are based on a discharge but do not account for its SoC dependency. The initial condition of the simulation corresponds to the boundary condition. Then the temperature-dependent heat source term is applied in the active material according to Equation 4.6 with the local temperature-dependent current and resistance. The temperature distribution, average temperature, current and heat are evaluated when a steady-state is reached.

$$I\big(T(t,x,y,z)\big) = \frac{1}{V_{AM}} \cdot I_{C/2} \cdot a \cdot \exp\left(\frac{-b}{T(t,x,y,z)-c}\right) \tag{4.7}$$

$$I_{\mathrm{Sim}} = \int_{AM} I\big(T(t,x,y,z)\big)dV \tag{4.8}$$

According to Equation 4.7 and 4.8, the overall current and overall heat dissipated can be calculated for the different cases by integrating current I and heat $\dot{Q}$ over the volume of the active material, where the heat is dissipated. This way, two objectives are pursued. First, whether and (if so) how the average cell temperature with a gradient differs from a homogeneous temperature. Second, how the temperature-dependent heat generation affects the temperature distribution.

Table 3. Average temperature, overall current I and heat generation $\dot{Q}$ for the simulation cases with the temperature-dependent heat generation.

Case	T_{avg} / K	I / A	$\dot{Q}$ / W
2C, Hom 12.5 °C	285.69	1.52	0.22
2C, Hom 25 °C	298.17	1.45	0.13
2C, Hom 37.5 °C	310.67	1.45	0.10
2C, Inhom 0 °C – 25 °C	285.68	1.45	0.21
2C, Inhom 0 °C – 50 °C	298.17	1.47	0.15

2C, Inhom 12.5 °C – 37.5 °C	298.17	1.47	0.14
2C, Inhom 25 °C – 50 °C	310.67	1.45	0.11
3C, Hom 25 °C	298.61	9.41	2.88
3C, Inhom 0 °C – 50 °C	298.50	9.14	2.71

Table 3 gives the results for the average temperature T, the overall current I and the overall heat generation $\dot{Q}$. The average temperature in all cases corresponds to that resulting from the respective boundary conditions. Only for a current of 3C, it is insignificantly elevated by 0.5 K due to the high heat dissipation. The current differs from the constant current applied for voltage recording due to the strict temperature dependency of the heat source. It deviates only slightly and is very close to 1.5 A for C/2, while it is exceeding the 9 A for 3C. Comparing the heat generation in the cases with homogeneous temperature control with those with an applied temperature gradient, the values demonstrate a heat generation that decreases with higher temperature but does not depend on the gradient.

The temperature profiles in Figure 20 b) are evaluated over the thickness of the cell at different locations as indicated by the grey lines as in Section 3.3. Here the temperature profile is shown for C/2 and the temperature gradient 0-50 °C. The temperature profiles are the same, only in the middle, the maximum temperature is lower. Overall, the heat generation does not alter the temperature profile, but the thermal conductivity within the cell does at the very edges of the cell stack. As the temperature profile is symmetric, the average temperature is still the same.

4.5 Interim Conclusion

The obtained results reveal that the lithium-ion cell at a temperature level below 20 °C exposed to temperature gradients behaves – in terms of its voltage obtained for low C-rates and resistance – as if it was slightly warmer than its average temperature. The EIS measurements with no significant heat generation indicate that it is not due to an actual higher average temperature. This is confirmed with the help of the simulations in which a temperature-dependent

heat source term is implemented. Even at a high C-rate, neither the heat generation nor the average temperature is higher for the temperature gradient than for the homogenous temperature control at the respective average temperature. Instead, the behaviour can be attributed to an asymmetric weighting of the cell regions with different temperatures. Troxler et al. [48] reached a similar conclusion based on impedance data. The lower resistance at high temperatures leads to higher current densities in this region. Thus, the cell performance is dominated by the properties of the warmer cell regions, and the overall cell behaviour is comparable to that of a cell at a higher average temperature.

This phenomenon changes when high currents are applied, as the voltage characteristics at 3C in Figure 13 show. The temperature-dependent current distribution in Figure 18 explains this now, as the normalised current for 3C deviates significantly from that for C/2. Since there is no maximum current at the high overvoltages of 3C even at high temperatures, the warmer region of the cell cannot dominate its behaviour. This diagram also reveals how strongly the current depends on temperature (or the temperature-dependent resistance). Despite this high temperature sensitivity, the overall influence of temperature gradients on the performance is not significant enough to require a limitation of temperature differences along with the electrode layers. Furthermore, the characteristic of the temperature-dependent heat source term shows that it is dominated by resistance at higher temperatures. Thus, in contrast to common belief, there is no positive feedback between temperature, current and heat generation, so that there are no safety-critical concerns associated with temperature gradients.

5 Non-Uniform Temperature – Cyclic Ageing

The general influence of temperature on the overall ageing phenomena is basically known and discussed in Section 2. So far, however, there has been no systematic investigation of how temperature gradients affect overall ageing and to what extent they lead to an inhomogeneous distribution of ageing mechanisms. This question is addressed by focusing on how a maximum tolerable temperature difference in the cell for ageing can be defined.

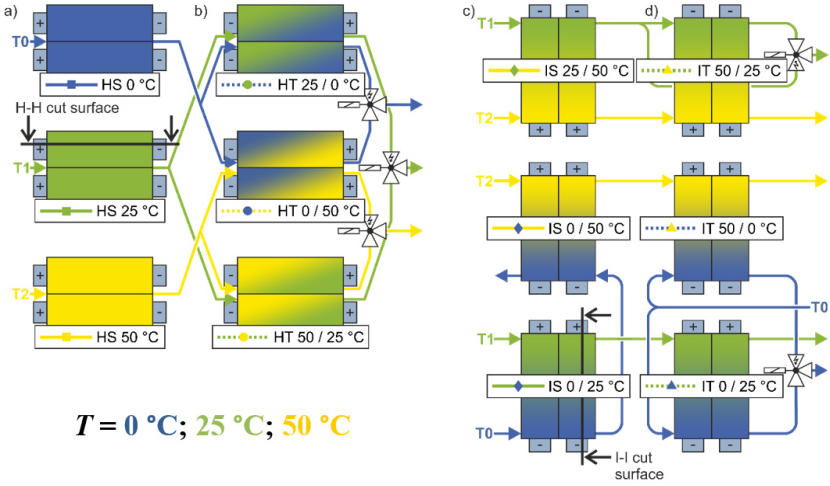

Figure 21. Flow diagrams with the thermal boundary conditions [68] (license CC BY 4.0). The colours represent the temperatures 0 °C (blue), 25 °C (green), 50 °C (yellow) and the letters the type of condition: H-homogeneous, S-stationary, T-transient, I-inhomogeneous. They are combined to a) homogenous stationary, b) homogeneous transient, c) inhomogeneous stationary, and d) inhomogeneous transient thermal boundary conditions.

The experimental set-up, the measurement results, and empirical ageing functions are published [68, 287]. The design of the test stand was part of the previous PhD project "Projekthaus e-drive", so it is not discussed here, and the

reader is referred to Part 1 of the joint publications [68]. In this work, first, the capacity fade and impedance increase during ageing are presented, and a temperature-dependent ageing function is derived. The degradation modes are then analysed using the differential methods. Subsequently, the results of the post-mortem analysis are reported and interpreted. The electrode, particle and atomic levels are considered.

The cyclic ageing tests were performed at a constant C-rate of 3C (9 A) over the entire SoC range. Different thermal boundary conditions were applied externally, as shown in Figure 21. The colours indicate the temperatures, and the symbols used later on in the graphs are already introduced here to facilitate the assignment of the legend entries to the boundary conditions. The temperature control is distinguished in four types of conditions:

a) The cells were cycled at homogenous stationary (HS) conditions (Figure 21 a)) at the three temperature levels 0 °C, 25 °C, and 50 °C, as a reference and basis for comparison.
b) For the homogeneous transient (HT) conditions represented in Figure 21 b), the temperature at the cell surface changed with time. The colour at the top shows the starting temperature. After half an electrical (dis)charge process, solenoid valves switched, and the second temperature was applied on the cells' surface during the other half of the (dis)charge process. The same sequence was repeated for each subsequent charge and discharge.
c) In the cases with inhomogeneous stationary (IS) temperature control in Figure 21 c), a temperature gradient between the reference temperatures was imposed along the length of the cell. In these cases, the lower temperature was applied to the anode tab.
d) In the inhomogeneous transient (IT) cases in Figure 21 d), the temperature on the cathode tab side of the cell remained constant. In contrast, the fluid on the anode tab side was switched on and off alternately in the same sequential pattern as in the HT cases. Consequently, the gradient developed and receded over time. In other words, a temperature front moved from the anode tab to the cathode tab and back again.

The SoH was determined by capacity and impedance measurements during check-up measurements conducted at homogeneous 25 °C. The check-up frequency was higher at the initial stage of ageing when it was conducted every 150 cycles. Later on, when the ageing slows down, the frequency is reduced to every 300, 600 and 900 cycles.

5.1 Capacity and Impedance

In this section, the capacity fade and impedance increase during cyclic ageing are analysed, first qualitatively then quantitatively. The data referred to is the remaining capacity obtained with a discharge current of C/20 and the polarisation resistance from impedance spectra at 50 % SoC. Both are related to the value at BoL according to Equation 5.1 and shown in Figure 22 as a function of equivalent full cycles (EFC) for the different set-ups. In general, the order of degradation is the same for each group of set-ups. This means a higher capacity fade comes with a higher increase in polarisation resistance, although they do not directly correlate. Figure 22 a) shows the results for the homogeneous stationary temperature control at the respective temperatures. As expected, the cells cycled at a temperature of 25 °C exhibit the least degradation. However, the capacity declines, and the impedance increases faster for both increasing and decreasing temperature, which is more pronounced at 0 °C than at 50 °C. The low charge throughput at 0 °C resulting in a low number of EFC is due to the high overpotentials at low temperatures. The influence of temperature changes over time between two temperatures can be seen in Figure 22 b). Especially for the changes over the wide temperature range of 50 K, a significantly higher loss of capacity and rise in polarisation resistance is recorded.

$$\Delta C_{\mathrm{C/20}} = \frac{C_{\mathrm{BoL}} - C(EFC)}{C_{\mathrm{BoL}}} \quad \text{and} \quad \Delta R_{\mathrm{pol}} = \frac{R_{\mathrm{pol,BoL}} - R_{\mathrm{pol}}(EFC)}{R_{\mathrm{pol,BoL}}} \tag{5.1}$$

Comparing the capacity fade of the stationary tests (Figure 22 a) and c)), lowering the temperature at the anode tab from 50 °C to 25 °C (IS25/50°C) results in a similar capacity fade as a homogeneous temperature of 25 °C (HS25°C). If the temperature on the anode side is further reduced to 0 °C (IS0/50°C), there

is hardly any change compared to the HS50°C condition. In contrast, the temperature gradient between 0 °C and 25 °C (IS0/25°C) has a severe effect on the capacity compared to cycling at a homogeneous temperature of 25 °C (HS25°C). Similar findings apply to increased polarisation resistance, although the resistance increase for IS0/25°C is more enhanced than for the other boundary conditions. Comparing the results of Figure 22 b) and c) reveals that a permanent temperature gradient between 0 °C and 50 °C (IS0/50°C) has less of an effect on the capacity fade and impedance rise than temperature changes between the same temperatures. The evolution of the capacities and impedances for the inhomogeneous transient condition in Figure 22 d) does not vary sufficiently with the different boundary conditions to allow for a meaningful interpretation [68]. Therefore, they are disregarded in the following.

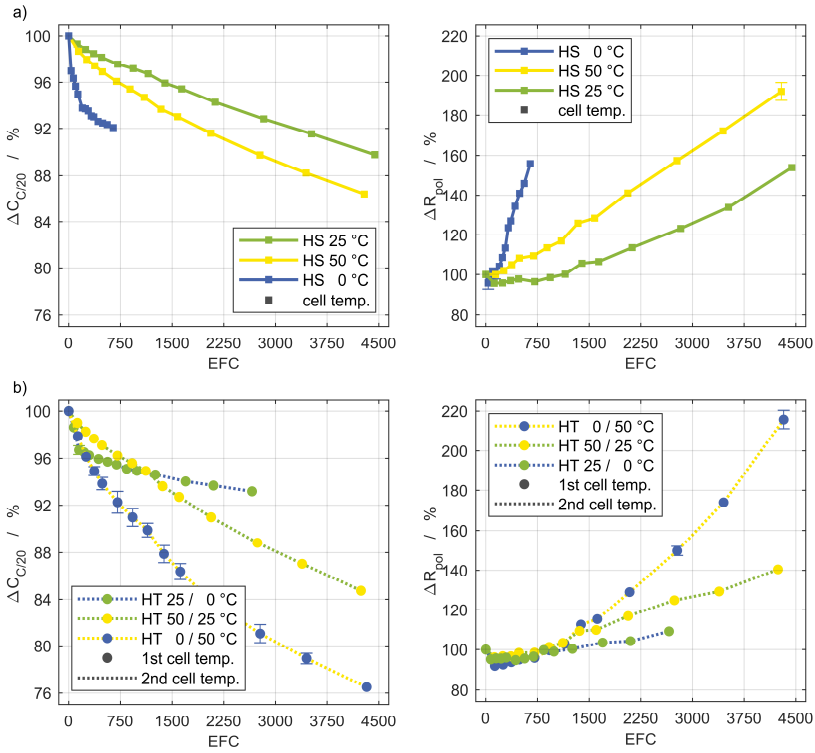

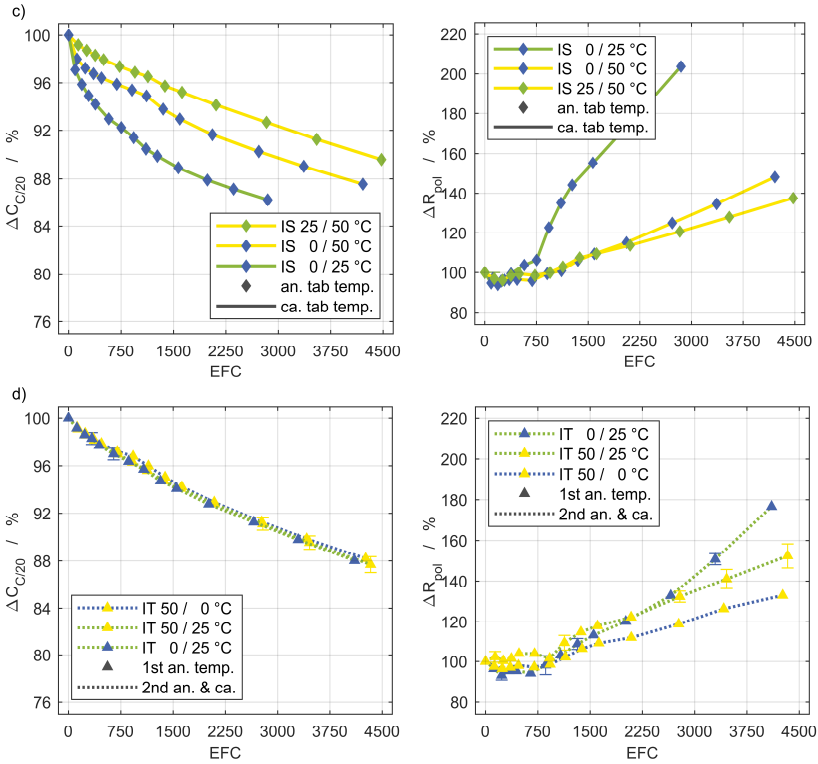

Figure 22. Remaining capacity (left column) and polarisation resistance (right column) for a) HS, b) HT, c) IS, and d) IT conditions [287] (license CC BY 4.0).

In order to enable a quantitative analysis of the degradation under various thermal conditions, we introduced the concept of the equivalent ageing temperature (EAT) [287]. EAT relates the degradation caused by spatial and temporal temperature inhomogeneities to similar degradation caused by a homogeneous stationary temperature control during cycling. According to Equation 5.2, EAT is calculated by temporal and spatial integration of the temperatures during one thermal cycle $t_{cyc,th}$, and over the cell length *L*. For this purpose, a linear gradient between the two temperature levels for the inhomogeneous set-ups and the same time constants for the heating and cooling processes for the transient set-ups are assumed.

$$T_{EAT} = \frac{1}{t_{\mathrm{cyc,th}} \cdot L} \int_0^{t_{\mathrm{cyc,th}}} \int_0^{L} T(t,l) dl dt \tag{5.2}$$

With this temperature value, the measurement data is fitted with an empirical approach of two exponential functions representing the high-temperature degradation and the low-temperature degradation, as proposed by Waldmann et al. [118].

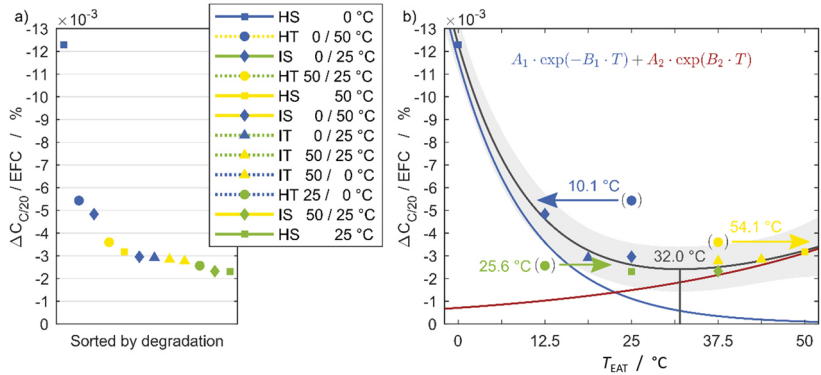

Figure 23. a) Experimental set-ups sorted by degradation and b) temperature-dependent ageing function for the capacity fade per EFC composed of two exponential functions [287] (license CC BY 4.0).

The capacity fade per EFC depending on temperature is shown in Figure 23 for all set-ups. Each set-up is included by one marker. To facilitate the assignment, they are sorted by degradation in Figure 23 a). The two exponential functions are shown in red and blue, while the overall ageing function is depicted in black with the confidence interval of 95 % in grey. Its minimum indicates the optimum temperature, which is 32 °C regarding capacity. It is in good agreement with most of the measurement points. Only the round markers representing the homogeneous transient conditions do not match the empirical ageing function. The arrows emanating from the markers for the HT conditions indicate the potential assignment of the respective ageing state to a new EAT that cannot be directly calculated with Equation 5.2. Instead, it is achieved by

a horizontal displacement of the measured data in either direction until it intersects with the ageing function. The resulting temperature marks the EAT that leads to the same degradation rate for a homogeneous temperature.

Table 4 lists the coefficients of the low- and high-temperature exponential part and gives the coefficient of determination R^2 for all quantities.

Table 4. Increase in slippage of electrode potentials related to the slippage at BoL.

	Low T		High T		
Quantity	A_1/-	B_1/°C^{-1}	A_2/-	B_2/°C^{-1}	R^2
$\Delta C_{C/20}$	0.1159	0.09366	71.05 10^{-4}	0.02962	0.9929
ΔR_{18s}	0.7735	0.08918	3.712 10^{-4}	0.1198	0.9963
ΔR_{ohm}	0.1496	0.08642	29.86 10^{-4}	0.07726	0.9518
ΔR_{pol}	0.8720	0.07913	2.279 10^{-4}	0.1356	0.9953

The bathtub-shaped ageing function in Figure 23 b) shows the capacity degradation as an example. Similar functions can be derived for the impedance quantities: ohmic, polarisation, and pulse resistance. The corresponding graphs can be found in the Appendix. Depending on the quantity, the two exponential functions for the ageing rate at high and low temperatures are differently pronounced. The ohmic resistance is the only one where the high-temperature degradation is equally temperature-dependent as the low-temperature degradation, indicating that high temperatures are particularly harmful to the ohmic resistance. The exponential function representing the ageing at low temperatures is steeper for the other quantities, as it is for the capacity in Figure 23. All these ageing functions are in good accordance with the measurement data except for the HT conditions. For all quantities, they cannot be reproduced by the ageing function.

The results presented above reveal that the temperature level is decisive for ageing behaviour. The ageing progress for cells cycled with an applied temperature gradient follows the respective averaged temperature, which means that inhomogeneities in temperature along the electrodes do not severely impact the ageing. In contrast, temperature changes with time induce a different ageing behaviour regarding capacity fade and impedance rise.

These phenomena are analysed further by determining the transition from the initially accelerated ageing to the more linear part in the capacity fade depending on EFC in Figure 22. This curve is fitted with the combination of an exponential and linear function shown in Equation 5.3. Subsequently, the number of EFC is determined, at which the influence of the exponential term becomes negligible. This is defined with a share of the capacity loss smaller than 0.05 %.

$$\Delta C_{C/20}(EFC) = d \cdot \exp(-e \cdot EFC) + f \cdot EFC + g \tag{5.3}$$

Figure 24 shows the EFC at which the exponential part of the capacity fade becomes negligible for the different boundary conditions depending on EAT. The linear part dominates considerably later at high temperatures. For the cases HS25°C, IS25/50°C and HT25/50°C, the transition never occurs. Possibly, an inverse function similar to the ageing function in Figure 23 would arise, where the shallow section is truncated.

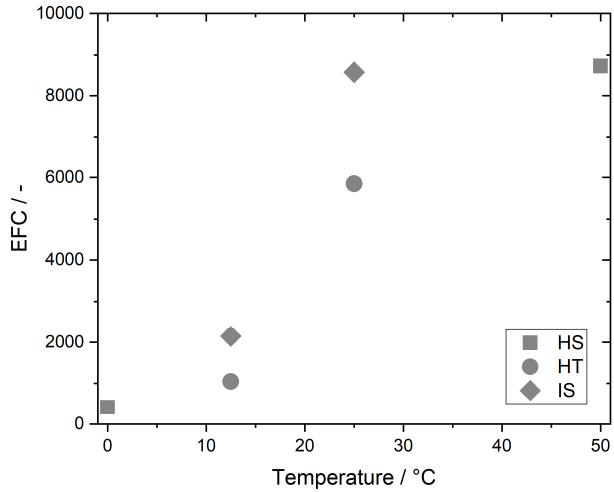

Figure 24. EFC at which the exponential share of capacity fade is negligible depending on EAT of the boundary conditions.

Bloom et al. [125] argue that the parabolic shape at the beginning of the capacity fade characterises a diffusion-limited process and assign this to the SEI

growth at the anode. They assume that enhanced ageing begins at the cathode with the transition to the linear part limited by a surface reaction step. Also, in their experiments, the transition to the linear ageing section does not occur under some conditions. Other authors also anticipate two-step ageing, with LLI occurring first at the anode and LAM [149] or cathode degradation [23] emerging subsequently. Further, it can be noticed that parameter *f* of the linear part, i.e. the slope which contributes to long-term ageing, differs between the boundary conditions irrespective of the onset of the linear region. The values are given in the Appendix. Perhaps, this slope can be correlated with the ageing on the cathode side. This consideration will be further explored during the post-mortem analysis.

5.2 Differential Methods

Before the results of the differential voltage analysis (DVA) and incremental capacity analysis (ICA) are evaluated, the data of two duplicate cells are cross-checked to ensure reliable results and with this justify to further continue with only analysing one cell for each case. All DVA and ICA at BoL are identical, meaning that changes occur only due to ageing at different thermal boundary conditions. Based on the BoL, Figure 25 a) illustrates the balancing of the electrodes and which features of the Kokam full cell can be assigned to either anode or cathode. The green curve depicts the half-cell potential of the cathode, the red one that of the anode, while the blue one represents the sum of both and thus the full cell voltage. In pink, the experimentally determined voltage of the full cell is presented. Figure 25 a) shows the shift of the anode potential at BoL necessary to align anode and cathode for achieving the balancing of the full cell. This shift or slippage increases during ageing and depends on the thermal boundary condition. The coloured vertical lines in Figure 25 b) mark the characteristics of the electrodes to trace changes in the DVA during ageing and assign them to the electrodes. The black circles represent anode characteristics, while the white circles reflect cathode features. Those numbered characteristics are displayed again in the DVA in Figure 26 a) with arrows indicating the peak heights and distances used for the later evaluation.

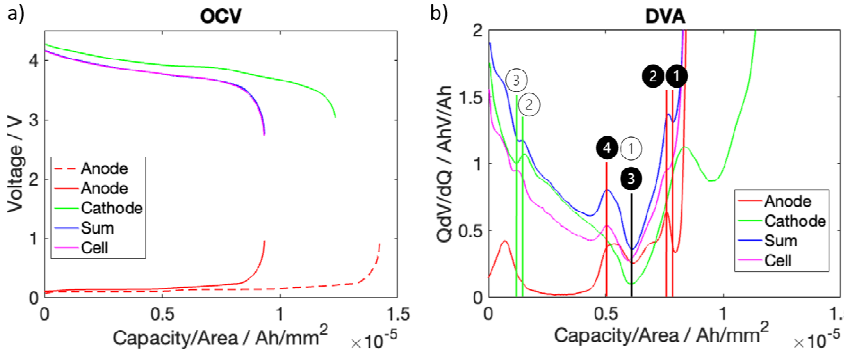

Figure 25. a) OCV of both electrodes with the anode shift to match the experimental voltage of the full cell. b) DVA calculated from the OCV of the electrodes, their sum and the full cell with the respective characteristics assigned to anode and cathode.

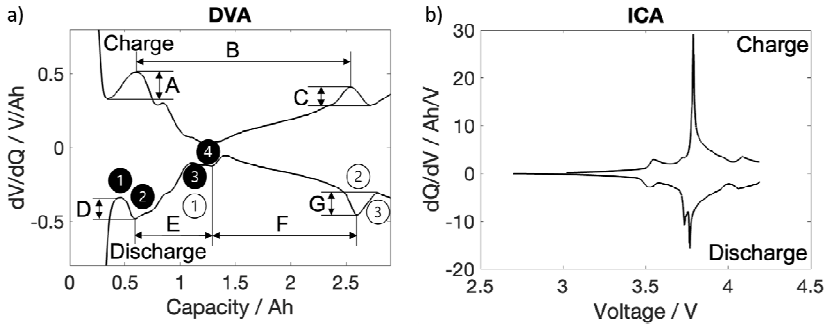

Figure 26. a) DVA for charge and discharge with the characteristics of the anode (black) and cathode (white) and the distances to evaluate the DVA quantitatively. b) ICA for charge and discharge.

In the ICA curve in Figure 26 b), the prominent peak during discharging has two spikes, while only one occurs during discharging. It is not entirely clear whether they originate from the two peaks of the anode or whether the main peaks of the anode and cathodes are superimposed differently during charging and discharging. Since the ICA of anode and cathode do not provide any significant additional value in the interpretation, for the electrodes, only the DVA data is shown and discussed in the following.

Regardless of the thermal boundary conditions, the features in all DVA curves become less distinct as ageing proceeds. However, the extent and speed differ. As the DVA and ICA for charging and discharging do not always exhibit the same changes, both are shown in the following. The evaluation is based on the approximate number of equivalent full cycles. Since the check-up measurements were performed after a certain number of theoretical cycles, they do not match exactly. In addition, the DVA and ICA are not shown for all boundary conditions after the same number of EFC, but only those that are particularly significant.

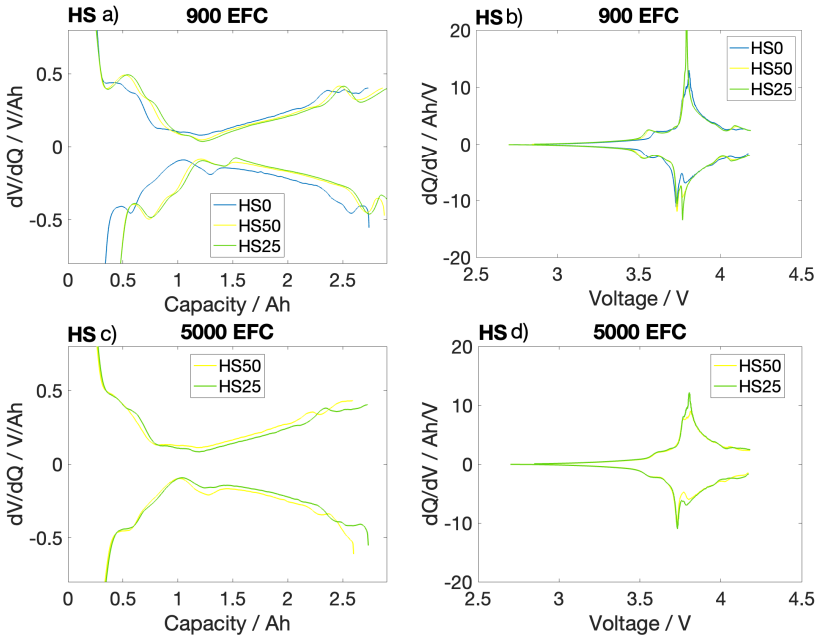

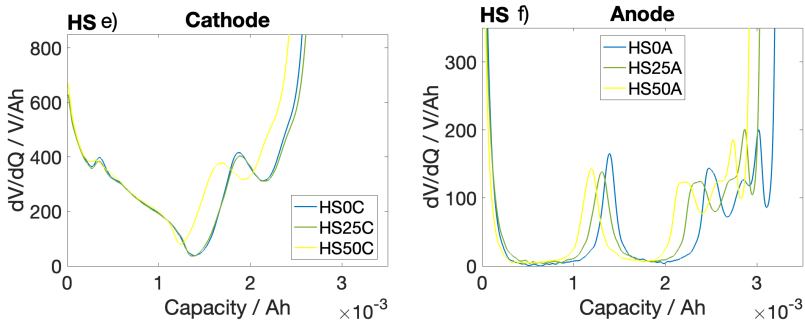

Figure 27. a) DVA and b) ICA of the Kokam full cell after 900 EFC, c) DVA and d) ICA of the Kokam full cell after 5000 EFC, and DVA of the e) cathode and f) anode half-cells of the aged cell at EoL for the homogeneous stationary conditions (HS).

Comparing the DVA of the cells with homogeneous stationary temperature control in Figure 27 a), HS25°C (green), HS50°C (yellow) and HS0°C (blue) are shown for 900 EFC. At higher EFC, there is no data for HS0°C as the charge throughput is very low at this temperature, as can be seen in Figure 22 a). HS25°C and HS50°C are hardly distinguished from each other over many cycles. Only at 5000 EFC, a stronger compression of HS50°C appears from the maximum towards higher capacities. Further, the anode peak (1) (left) decreases significantly, and the cathode minimum (2) (right) flattens to its near disappearance.

The changes at HS0°C already arise at considerably lower EFC. They appear as a complete shift to lower capacities and a reduction of the anode peak (1). In addition, the peak resulting from both anode and cathode broadens, which may be due to a shift in balancing. The cathode contribution to the overall DVA is minor compared to the anode. Similarly to the DVA, both the anode and cathode peaks decrease in size in the ICA in Figure 27 b). The main peak becomes broader for HS25°C and HS50°C while it divides for HS0°C. Possibly, precisely the two peaks that occur during charging are now also visible during discharging.

In the DVA of the electrodes, the features are still highly discernible, as visible in Figure 27 c) and d). This points to LLI as the primary degradation mode. In

the experimental cells, fresh electrolyte is used, and with the lithium anode, lithium is in excess available, which substitutes the lack of lithium in the aged cell. The most remarkable change for the cathode and anode occurs for HS50°C, which becomes apparent as a compression of the curve and suggests LAM additionally.

A comparison of the inhomogeneous temperature control during cycling shows an early onset of ageing at 500 EFC for IS0/25°C in Figure 28 a) and b) with the disappearance of anode peak (1) and reduction of cathode peak (3). This is apparent in both the DVA and ICA. When reaching 5000 EFC in Figure 28 c) and d), IS0/50°C and IS25/50°C exhibit similar transformations and the DVA and ICA of the different temperature gradients have converged to some degree. Although at IS0/25°C, the anode peak (2) has completely vanished, and the main peak in ICA has significantly decreased compared to IS0/50°C and IS25/50°C.

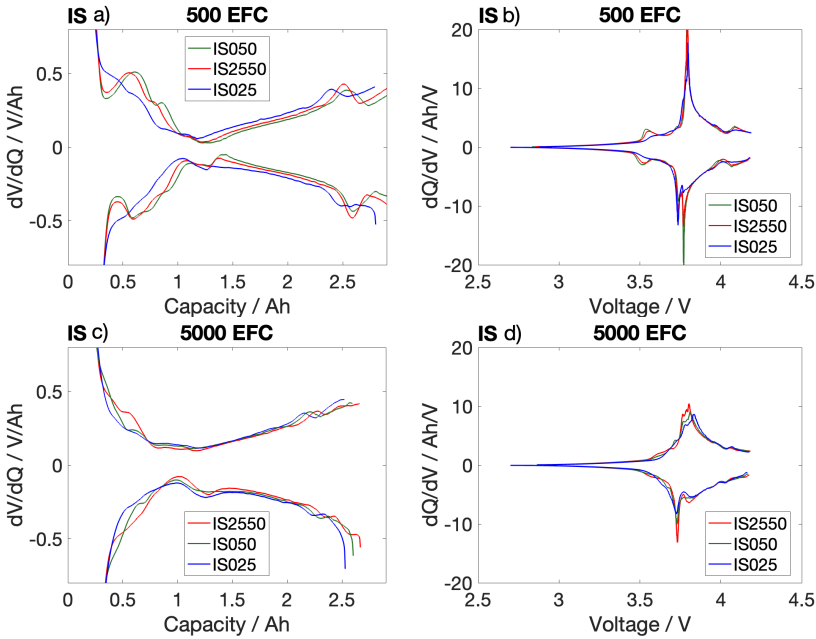

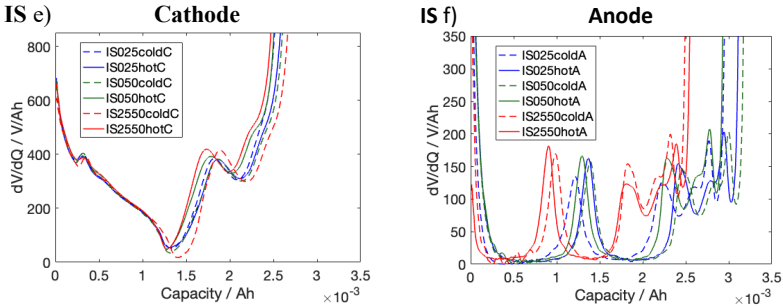

Figure 28. a) DVA and b) ICA of the Kokam full cell after 900 EFC, c) DVA and d) ICA of the Kokam full cell after 5000 EFC, and DVA of the e) cathode and f) anode half-cells of the aged cell at EoL for the inhomogeneous stationary conditions (IS).

The DVA curves of the half-cells in Figure 28 e) and f) reveal differences between the warm and cold sides of the electrodes. In the case of the cathode, a differently pronounced compression of the DVA begins to occur at the minimum. The most considerable difference is between the cold and hot sides of the cell with the temperature gradient between 25 °C and 50 °C. For the anode´s hot side, the solid green (IS0/50°C) and red (IS25/50°C) lines are well apart for the anode characteristics, although both had a temperature of 50 °C during cycling. Similar results are obtained for the DVA curves of the regions cycled at 0 °C with the dashed blue (IS0/25°C) and green (IS0/50 °C) lines as well as the solid blue (IS0/25°C) and dashed red (IS25/50°C) which had 25 °C during cycling. Thus, when looking at the half-cell DVA, no trend can be seen concerning temperature, and no conclusion drawn whether the warm or cold region of the cells is more prone to ageing.

The capacity fade and differential analyses of the full cell do not indicate pronounced ageing for IS25/50°C, but the anode DVA of the warm and the cold side is compressed the most in this case. This indicates increased ageing of the anode active material. This strong variation of the anode DVA could be the reason for the different ageing rates of the inhomogeneous stationary conditions.

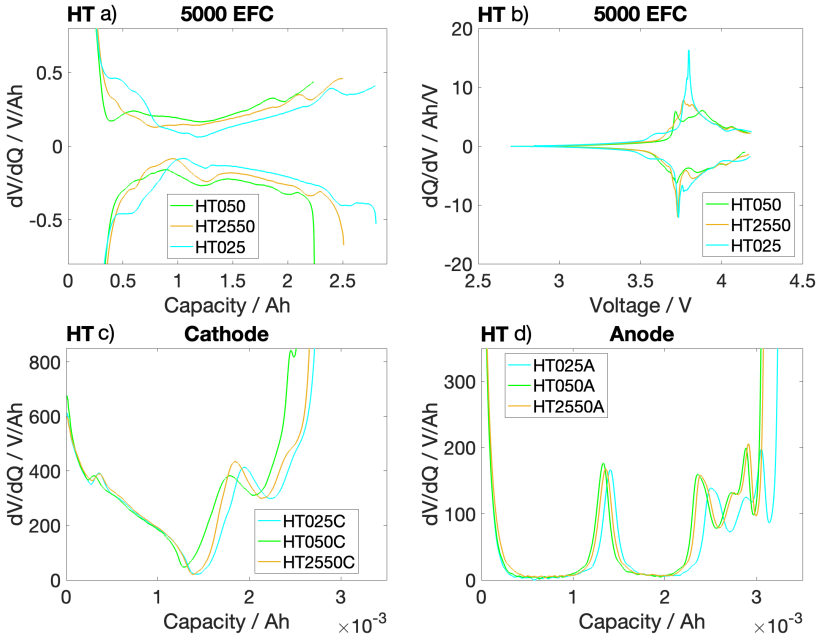

Figure 29. a) DVA and b) ICA of the Kokam full cell during and after cyclic ageing and DVA of the c) cathode and d) anode half-cells of the aged cell at EoL for the homogeneous transient conditions (HT).

The cells cycled with temporal temperature changes have strong changes in DVA and ICA, as can be seen in Figure 29 a) and b), especially for HT0/50°C and HT25/50°C. For both, the anode minimum (2) is no longer discernible at all, and the curve is flatter. The anode peak (1) in DVA and ICA has disappeared for HT0/25°C and combines with the local minimum of the anode (2) to a plateau. The cathode peak on the right is less pronounced but still detectable. The ICA of HT0/25°C is the only one that still resembles the ICA at BoL. The temperature changes at higher temperature levels lead to a broadening of the main peak so that instead, a plateau of several small peaks is formed.

Comparing the different thermal boundary conditions according to their temperature level, there are hardly any changes in DVA and ICA at high temperatures up to 5000 EFC. Whereas at low temperatures, significant differences

occur much earlier. The changes for high temperatures can be attributed to variation in the characteristic curve of the cathode half-cell. The severest changes are observed for HS50°C and in the warm part of IS25/50°C as shrinkage and a reduction in cathode peak (2).

Table 5. Increase in slippage of electrode potentials related to the slippage at BoL.

Case	Increase in slippage / %
HS 0 °C	55
HS 25 °C	44
HS 50 °C	44
IS 0 C – 25 °C	41
IS 0 C – 50 °C	76
IS 25 °C – 50 °C	-18
HT 0 °C – 25 °C	50
HT 0 °C – 50 °C	85
HT 25 °C – 50 °C	76

The shift in electrode balancing to match the full cell voltage differs for the boundary conditions without developing a temperature related trend. Table 5 gives the changes in slippage relative to the initial balancing at BoL. A significantly increased shift in the electrode potentials is found for the boundary conditions HT0/50°C, HT25/50°C, and IS0/50°C. This suggests a significant contribution of LLI [161, 162].

DVA is further quantitatively examined using the lines introduced above in Figure 26 a). Peaks A and D, peaks C and G, as well as the sections E and F and their sum B, represent the same characteristics for charging and discharging, respectively. In the course of ageing, each pairing behaves analogously. Therefore, only the discharge is analysed in the following, corresponding to the qualitative consideration. The colours in Figure 30 correspond to the colours used in Figure 27 - Figure 29. To better distinguish, the HS conditions are represented by solid lines, the IS conditions by dashed ones and the lines for HT conditions are dash-dotted with additional markers. Length D in Figure 30 a) describes the height of an anode peak, E in Figure 30 b) the distance between two anode peaks, F in Figure 30 c) between an anode and one cathode

peak, while G in Figure 30 d) characterises the height of the cathode peak. The peak height D decreases for all boundary conditions to a different degree until the peak (except at HT0/25°C) is no longer discernible at all. The reduction tends to be more pronounced at low temperature levels. The height G of the cathode peak after 5000 EFC is similar for all cells, but its development depends strongly on the thermal boundary condition during cycling. For IS0/50°C, the peak remains constant over a long time and decreases rapidly from about 1000 EFC. HS25°C and IS25/50°C behave similarly, whereas, with IS0/25°C, a rapid peak reduction appears up to 500 EFC and then it remains almost constant. The other cells are positioned between the two extremes. Looking at lines E and F, HT0/50°C exhibits a massive reduction in both, implying major ageing of the active material. For all cells, the distances mainly change in the later stages of cycling, suggesting that LAM does not significantly influence ageing at the beginning. Only section D, which is assigned to the anode peak, reveals immediate alterations.

Overall, the DVA and ICA of the half-cells still have distinctly defined peaks after ageing, which differ comparatively little from the BoL – quite in contrast to those of the commercial cell. This suggests that the active material itself is mainly undamaged and that during ageing, primarily LLI and a shift in balancing occur as well as potentially inhomogeneities. The flattening slope of the ICA possibly indicates inhomogeneous ageing [167]. This is observed for the homogeneous transient temperature control at higher temperature levels HT0/50°C and HT25/50°C, as well as for all inhomogeneous stationary temperature-controlled cells. When the differently aged characteristics overlap in the DVA, this leads to peak broadening and a less distinct shape. This could explain why the mentioned full cells show severe degradation while the half-cells are still in good condition.

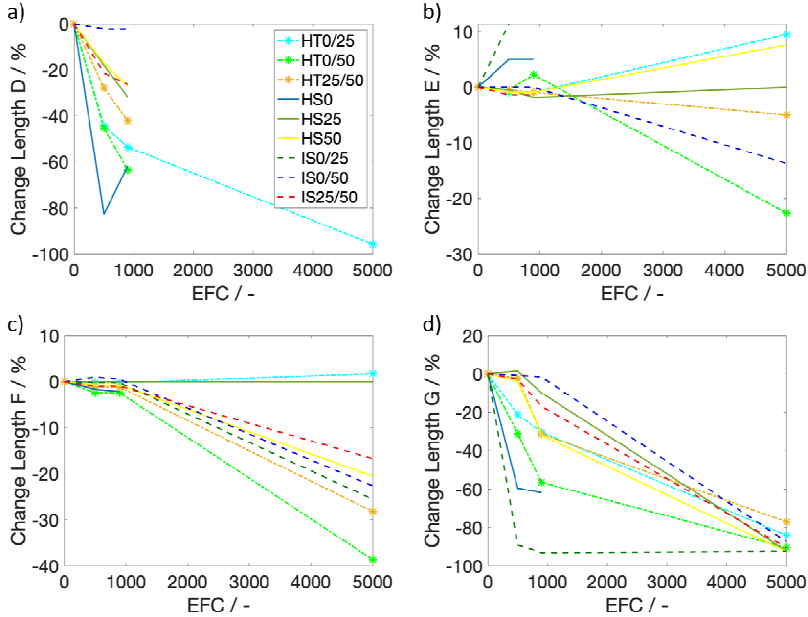

Figure 30. Deviation of the peak heights and sections in DVA during ageing as indicated in Figure 26. a) the anode peak height D, b) the section between two anode peaks, c) the section between anode and cathode peak, and d) the height of the cathode peak.

Furthermore, the electrode balancing and the changes in the differential curves show that LLI is the dominant degradation mode. This is particularly pronounced for low temperatures. Cathode ageing sets in later and occurs more intensely at higher temperatures. LLI is also considered to be the main cause of ageing by other authors [149, 158]. Wu et al. [46] observed the slope of the broad main peak in the DVA to become flatter in a NCA/LCO blend cathode during cycling at 10 °C and attribute this to LLI and degradation of the LCO. In this work, a slightly lower slope is detected for the homogeneous transient boundary conditions HT0/50°C and HT25/50°C. The reason is unknown, but as it does not occur at low temperatures, it might have another cause.

5.3 Interim Conclusion

The results of cyclic ageing with different thermal boundary conditions demonstrate that the optimum operating temperature for minimum capacity fade and rise in resistance is not the same. Overall, it lies above 25 °C, which is generally assumed as optimum and often used as reference. With minimum ageing at the optimum temperature, it accelerates with increasing and decreasing temperature. This correlation can be described by the two superimposed exponential functions of the EAT according to Equation 5.1 and as shown in Figure 23. Based on this representation, it becomes possible to detect that cells with a temperature gradient age integrally according to their average temperature. In contrast, temporal temperature changes provoke a different ageing behaviour, which cannot yet be conclusively explained or mathematically represented. This leads to accelerated ageing for temperature changes in the high (25 °C – 50 °C) and the whole (0 °C – 50 °C) temperature range, while it is reduced for the low temperature range (0 °C – 25 °C). However, the analysis by differential methods suggests that at all thermal boundary conditions predominantly lithium is lost in side reactions. This is in line with findings for a NCA/LCO cell by Wu et al. [46], who attributed the accelerated ageing at temperatures > 25 °C to a hastened SEI growth.

Different contributions to the ageing process are involved, which show distinct temperature dependencies. They are revealed by the transition from a dominant exponential to linear ageing when the capacity fade with increasing EFC is described. Additionally, the evaluation via the differential methods first indicates a loss of active lithium (LLI) before a loss of active material (LAM) is observed, mainly at the cathode. LLI is the main degradation mode, causing a shift in the electrode balancing. This explains the substantially altered curves of DVA and ICA, while the half-cells of both electrodes exhibit comparatively little change. LLI is even more pronounced at low temperature, while at higher temperature, there is also more degradation at the cathode. As shown in Section 4, a cell with an applied temperature gradient behaves regarding OCV and impedance as if it were slightly warmer than its average temperature. Fleckenstein et al. [12] assume a similar effect for ageing. Looking at the diamonds depicting the inhomogeneous stationary temperature control in Figure 23, they

lie not exactly on the black line of the ageing function. However, the deviations are so minimal that it can be assumed at this point that a temperature gradient has no effect on the overall ageing behaviour – regardless of its magnitude. Comparison employing the DVA is difficult because, with the average temperature of the gradients, a direct comparison is only possible for IS0/50°C and HS25°C. Nevertheless, the anode characteristics (1) and (2) exhibit substantial alterations when temperature gradients are applied, and the peak has almost disappeared in all cases in contrast to the cells cycled at homogeneous temperatures. Still, these differences remain insufficient to derive a maximum tolerable temperature difference over the length of a cell.

5.4 Cell and Electrode Scale

So far, the sealed cell was investigated by electrochemical methods. Although it is possible to deduce the dominant degradation modes with DVA and ICA, the underlying mechanisms, either physical or chemical, that provoke ageing cannot be identified. This, however, is possible with a post-mortem analysis. The results of such an analysis for the cells under investigation are presented therefore in the following. In particular, the following methods are used for analysing cell and electrode scale: visual inspection of cell and electrodes, SEM of the electrode surfaces and cross-sections and the determination of thickness and weight. Furthermore, to investigate the ageing effects on the atomic scale, XRD, ICP-OES and XPS are employed.

Visual inspection

None of the cycled cells shows evidence of excessive gas formation. The vacuumed pouch film was tight around the cell stack for all cells. The remarkable features, which are directly noticeable at the cell opening, are presented first, and SEM images are shown. Subsequently, the results of the layer thicknesses and weight are evaluated.

The cell opened at its BoL state reveals slight discolouration at the edge of the separator, and the separator and electrode adhere slightly at the production-related marks. Otherwise, the surface of both electrodes is homogeneously

black to the naked eye, and the humidity of the electrolyte is apparent. For all aged cells, the severest changes occur in the outer layers. Compared to BoL, the cell cycled at homogeneous stationary 25 °C (HS25°C) shows a slightly greyish deposit at the outermost anode layer and a slightly increased discolouration at the separator edges.

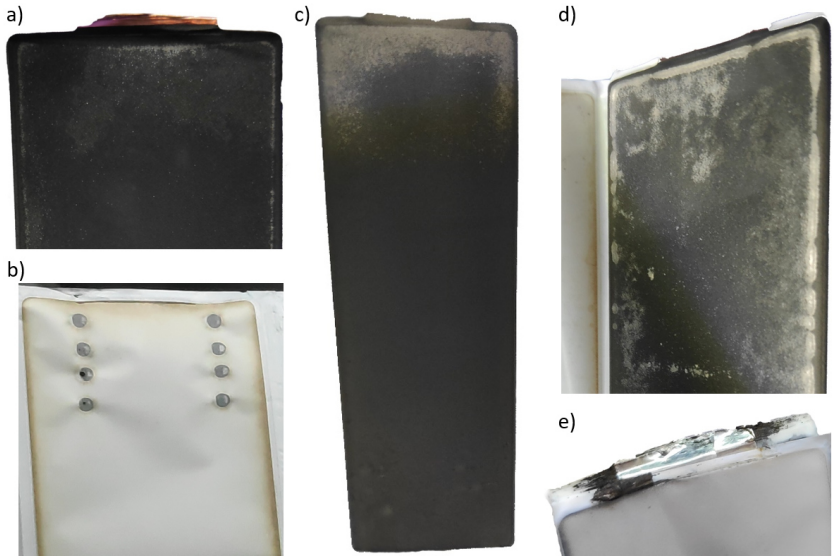

Figure 31. Photographs during cell openings. a) Anode of HS0°C with some plating, b) discoloured separator of HS50°C, c) anode of IS0/50°C with plating in the coldest quarter, d) massive plating on the HT0/50°C anode and e) dead lithium (black material) close to the cathode tab of HT0/50°C.

HS25°C serves as a reference and basis of comparison for the cells aged at other boundary conditions. The most remarkable difference of HS0°C is an irregular blotchy anode surface, with a clear indication of lithium plating close to the anode current collector and the edges where the anode overlaps the cathode (edge effect) as depicted in Figure 31 a). In contrast, the most noticeable change with HS50°C is the strong discolouration of the separator, not only at the edges as in Figure 31 b). For the inhomogeneous cell with a temperature

gradient between 0 °C and 50 °C, Figure 31 c) shows the distinct plating visible on the anode localised at the coldest quarter close to the anode tab. The silvery/grey cover layer is discernable throughout the cell stack. Furthermore, the separator has a greyish colouration comparable to the HS50°C cell. IS0/25°C also exhibits clear plating from the anode tab where the 0 °C were applied during cycling up to the electrode's centre. This large area of partially thick planar plating on the surface potentially lengthens the diffusion paths [44] and thus could explain the comparatively large increase in polarisation resistance. The edge effect is evident, but otherwise, the lithium deposition is randomly distributed on the surface. Compared to the IS0/50 °C, there is much less plating and significantly more compared to HS0°C. Probably, this can be attributed to the higher SoC that are reached due to lower overpotentials for a higher average temperature. The cell with a gradient between 25 °C and 50 °C does not reveal any striking details compared to HS25°C. Assuming a linear temperature profile, the significant lithium plating is limited to the cell area where a temperature between 0 °C and about 12 °C is applied. This finding indicates that temperature effects dominate over increased current density at regions with higher temperatures.

The separator of HT0/50°C with temperature changes between 0 °C and 50 °C seems to be slightly molten between some electrode layers directly at the anode current collector. This would mean that the temperature was close to the melting temperature of PE with ~134 °C at least once during cycling. Moreover, the homogenous transient cells exhibit two phenomena concerning the anode. The first one is again lithium plating on the surface, occurring at HT0/25°C and HT0/50°C. While the anode surface of HT0/25°C is covered homogeneously with small metallic deposits, HT0/50°C in Figure 31 d) shows inhomogeneous patches comparable to HS0°C. Secondly, in HT0/50°C and HT25/50°C, an enormous amount of black friable additional material is found. It is located at the anode side, not on but adhered to the electrode and mainly near the cathode tab. It even grows from between the separator layers, as shown in Figure 31 e), which is observable after removing the pouch foil. In minimal amounts, this also appears in the other cells, either in the separator fold or near the cathode tab. A flame test for material detection via the characteristic emission spectrum shows a red flame colouration, indicating Lithium with the two

main spectral lines at 671 nm [288]. Presumably, the material is dead lithium that deposited rather than intercalated and then reacted with electrolyte to SEI. The localised material close to the cathode tab might be due to nonuniform electrolyte filling [289]. It could also be related to the significantly lower pressure at the edge of the cell stack than between the electrodes. Therefore, mossy lithium can deposit and grow further there. Li et al. [200] provide similar considerations, claiming that lithium is deposited in a mossy morphology when the SEI is elastic. Since a large amount of dead lithium arises only for HT0/50°C and HT25/50°C, temperature changes seem to be critical for this phenomenon. The temperature increase during charging from 0 °C to 50 °C reduces the overpotentials and changes the balance of the rate-determining processes so that lithium plating occurs. Similar observations are reported by Carter et al. [145] for charging at transient temperatures. This can explain the accelerated ageing rate for homogeneous transient thermal boundary conditions noticed for capacity fade in Section 5.1 and the massive loss of lithium inventory indicated by DVA and ICA.

SEM

SEM images of cross-sections and surfaces in Figure 32 show detailed changes for the different thermal conditions. Primary particles of NCA increasingly lose their adhesion at elevated temperature resulting in reduced integrity and finally cracking of secondary particles along the boundaries between the primary particles. This is visible in the cross-sections of the cathode for the HS boundary condition in Figure 32, indicated by yellow circles. After cycling at 0 °C, the primary particles composing the secondary particles are not discernible, just as in the BoL state. The first secondary particles break during cycling at 25 °C, and at 50 °C, the primary particles of each secondary particle are well identifiable, and some are completely broken. This is also evident in the close up of the surface circled in yellow. The particle rupture probably is a consequence of higher mechanical stress caused by phase transformation. At elevated temperatures, the cut-off voltages are reached after a larger charge throughput, and the phase transformation, which occurs mainly at high voltages [290], is completely undergone. Whether the same is valid for LCO can not be revealed by the electrode sections analysed. Furthermore, in the surface

images, there are more deposits visible for increasing cycling temperature. The cathode that was cycled at 50 °C shows darker patches which seem to be flake-like particles (blue arrows). The graphite anode does not exhibit any alteration in the cross-section, so the images are not shown.

However, the inspection of the surface reveals significant modifications. The anode cycled at 0 °C is, in some places, coated with a thick homogeneous layer that looks like it is shrunk on the surface (orange arrows) and is assumed to be one morphology of plated lithium. Otherwise, there is little change in the typical flake structure of graphite in this case. For 25 °C, there are minor changes compared to BoL as the surface layer, probably SEI, blurs the edges of the flakes slightly more. The anode cycled at 50 °C exhibits much more non-uniform surface phenomena. Again, the blurring of the edges is visible together with tiny granular deposits in the first picture attributed to electrolyte degradation and SEI, while in other regions and the second picture, clusters of needle-like crystals appear. Presumably, this constitutes another morphology of lithium plating. These findings suggest that the morphology of plated lithium depends on the cycling temperature. While the deposits tend to be needle-like or granular at high temperatures, they are more planar and homogeneous at low temperatures. This observation is supported by Park et al. [291], who report less dendritic growth for lower temperature and Li et al., who state that for extensive deposition, the morphology is planar [200].

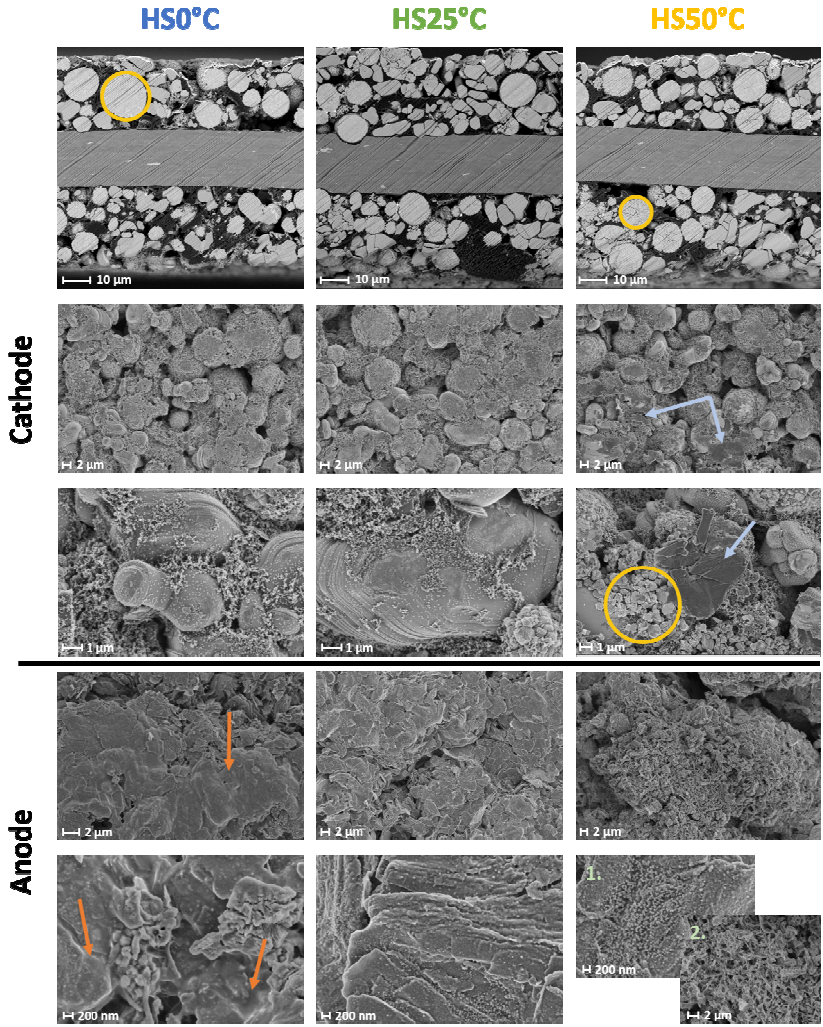

Figure 32. SEM images at EoL of cathode cross-section (first row) and surface (second and third row) and the anode surface (fourth and fifth row) for cycling at homogeneous stationary temperature control at 0 °C (first column), 25 °C (second column), and 50 °C (third column).

Thickness and Weight

Before cell opening, the thickness of the whole cell was measured. The results are shown in Figure 33 a) as a change relative to their initial state at BoL. The squared markers indicate the homogeneous stationary condition, the round markers represent the homogeneous transient condition, while the diamonds mark the inhomogeneous stationary ones. There is a clear tendency with increasing average temperature with a maximum thickness increase of 5 % after cycling at 50 °C. The cells with homogeneous transient temperature control, except HT0/25°C, show the largest growth in thickness at the respective average temperature.

Figure 33 b) shows the change in anode thickness as a function of temperature. The electrode thickness was measured at both the cold and the warm sides for the cells with inhomogeneous temperature control. The thickness at the warm side is indicated with the light grey, while the cold side thickness is dark grey. In general, the anode thickness increases with higher temperatures, exhibiting the same trend as the cell. At the same time, there is no discernible influence of the temperature on the thickness of the cathode layer. Still, the growth between 37 % and 47 % for the anode is much higher than the 1 % - 5 % thickness increase of the whole cell. This is because, on the one hand, the inactive components separator and pouch foil are included, and the cathode thickness hardly changes. On the other hand, the pouch foil ensures a firm tightness squeezing the anodes together elastically. Presumably, the expansion of the anodes leads to the observed increase in cell thickness and, at the same time to higher pressure within the cell.

The thickness changes of the anodes with homogeneous transient temperature control are noticeable, as they are not in line with the other data. The anodes of HT0/50°C and HT25/50°C are slightly thicker, as their average temperature would suggest, while those of HT0/25°C are thinner. This picture is similar to the capacity loss, which is more significant for the first two and less for the last one than expected by the ageing function (cp. Section 5.1, Figure 23). For the other cases, the trend of increasing anode thickness with temperature is evident and almost linear. This is equally true for cells cycled at homogeneous stationary conditions as well as for those cycled with a temperature gradient. The

higher thickness at the cold edge of IS0/25°C might be due to the high amount of thick lithium plating on the surface. Thus, it can be concluded that the anode thickness is determined by the actual local temperature, independent of other conditions elsewhere. Similar results for cycling at homogeneous temperature were obtained by Waldmann et al. [198], although they found an S-shaped correlation of anode thickness and temperature, not a linear one.

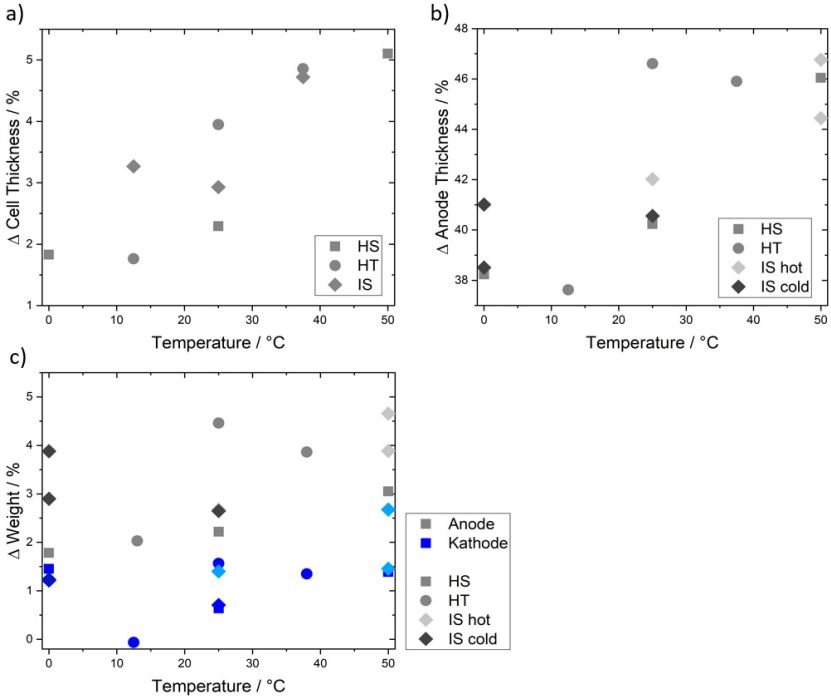

Figure 33. Increase in a) the cell thickness, b) the anode thickness, and c) the weight of anode and cathode depending on temperature for the different thermal boundary conditions during cyclic ageing.

The relative increase in weight in Figure 33 c) resembles the picture of the layer thickness, although it is much lower. There is a higher increase in weight for higher temperatures, but it does not follow the tendency for homogeneous transient conditions. In contrast to the layer thickness, the weight at the edges

with applied temperature gradients does not correspond to that after cycling at respective homogeneous temperatures but is higher. Probably, the pores become partially clogged, and the porosity decreases with ageing.

Presumably, the effects contributing to the increase in thickness and weight are purely temperature-dependent and not depending on current. Side reactions and thus SEI growth are certainly accelerated at high temperatures and contribute partly to the increase in anode thickness. However, since there is no covering layer visible in the SEM micrographs that would indicate an increase of the anode thickness of almost 50%, there are additional mechanisms involved. Assumably, cycling at elevated temperatures leads to increased solvent co-intercalation so that the graphite particles expand over time, leading to the thickness increase.

5.5 Atomic Scale

XRD spectra of the cathodes are analysed to check whether changes in their crystal structure occur during the cycling. In addition, with ICP-OES, the concentration of aluminium, cobalt, nickel, lithium and phosphorus in the anodes is measured. Furthermore, XPS is used for a detailed analysis of the SEI and its constituents.

XRD

XRD reveals that for all thermal boundary conditions, lattice parameter *a* decreases while lattice parameter *c* increases for both NCA and LCO. Except for parameter *a* of LCO at HT0/25°C, which increases slightly. The increase in *c* combined with the decrease in *a* leads to a distortion of the crystal structure where the layers are more widely spaced while the atoms within a layer converge. These alterations are more pronounced in NCA. The expansion along the x-axis indicates less lithium within the structure [218].

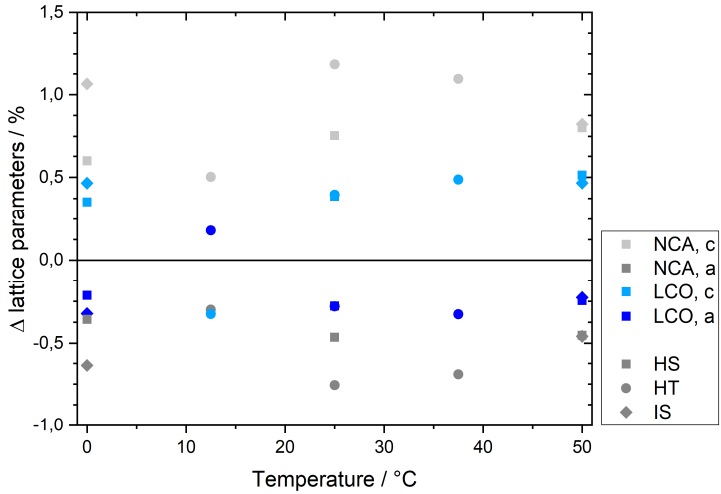

Figure 34. Change in lattice parameters *a* and *c* relative to BoL for NCA and LCO.

At first glance, there is little temperature dependency in the parameter variation in Figure 34. Still, for lattice parameter *c*, the values for cells with homogeneous stationary temperature control increase with rising temperature, which is more pronounced for NCA than for LCO. Temperature gradients have different effects for the warm and cold regions. In the warm region, the change in the lattice parameters is about the same as for homogeneous temperature control, while in the cold area, there are greater differences than with the equivalent homogeneous temperature control. Again, this is more prominent for NCA than for LCO.

Moreover, the homogeneously transient cycled cells once again exhibit a pattern that deviates from their average temperature comparable to that of the layer thickness increase. Thus, HT0/50°C and HT25/50°C have a more significant change in *c*, while it is relatively small for HT0/25°C. Lattice parameter *a* does not indicate a significant temperature dependency, but the homogeneous transient cells show a significantly larger decrease in the lattice parameters for NCA. Besides the change in lattice parameters, a slight shift of the peaks in

one or the other direction can be observed in the spectrum. However, this cannot be correlated with the boundary conditions and is therefore not presented here. No splitting of one or more peaks can be observed as, for example, in Maher et al. [236]. Therefore, it can be assumed that a hexagonal crystal structure is still present after cycling, in which only the c/a ratio has increased, which is supported by literature [120, 133]. In terms of crystal structure, NCA appears to be more prone to these effects than LCO.

ICP-OES

The concentration of aluminium, cobalt, nickel, lithium and phosphorus in the anodes is measured by ICP-OES. Transition metals are present in all samples. Thus, their dissolution has occurred at the cathode during cycling. The temperature dependency shown in Figure 35 a) is not quite as apparent as it is when observing the layer thicknesses. The largest amount is found for cobalt, followed by nickel and aluminium, which corresponds to the order of their stability. The cobalt concentration increases with rising temperature up to 0.19 weight-% for the anode at 50 °C in the cell cycled with a temperature gradient. Aluminium has a higher concentration only at 50 °C, especially for the anode for HS50°C, while there is a slight decrease for nickel.

The trend of increasing lithium concentration at higher temperatures is evident in Figure 35 b). It increases for homogeneous stationary temperature control with rising temperature, and for applied gradients (IS0/50°C) and especially temperature changes (HT0/50°C), it is even further increased.

Similar results are obtained for phosphorus shown in Figure 35 c). The highest concentration of phosphorus is found in the HT0/50°C cell. However, there seems to be no temperature influence below 25 °C, while the concentration increases significantly at 50 °C. The measured values are in the same order of magnitude as they are found in literature [118, 220] but are slightly higher. This can be explained by the long duration of the experiment and the high number of EFC. The weight percentage of lithium is significantly higher but depends strongly on the voltage at cell opening and is therefore difficult to compare.

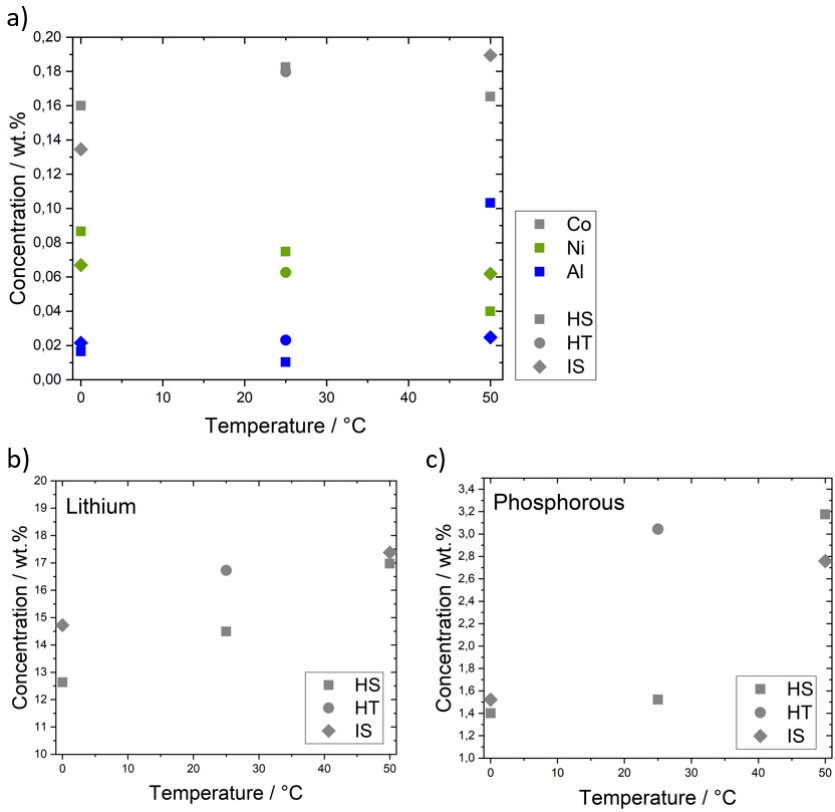

Figure 35. Concentration in weight percentage of a) the (transition) metals, b) lithium, and c) phosphorous in the cycled anode active material.

The results for phosphorous and lithium correlate positively with the temperature dependency of the anode thickness, suggesting that the thickness increase is primarily due to SEI growth after all. This SEI growth is likely accelerated by higher temperatures leading to higher reactions rates and the transition metals incorporating into the SEI and altering it. The relative impact of temperature increase and the presence of transition metals on SEI growth cannot be distinguished. Still, as an increased temperature causes enhanced cross-talk, it is the relevant factor. However, there must be another relationship that explains

the behaviour of homogeneous transient temperature control. Both the film thickness and XRD indicate increased ageing with temperature changes at medium and high temperature levels, which is also confirmed in the weight fractions of phosphorus and lithium from ICP-OES. Nevertheless, no increased fraction of transition metals appears in the anode for these boundary conditions. The change of the lattice parameters in the crystal structure is not directly related to their dissolution.

XPS

XPS is a powerful technique for detailed analysis of the SEI. However, for reliable interpretation of the results, the system must be known as best as possible in its initial state. Since neither the solvent nor the electrolyte additives are known for the commercial cells, BoL samples are examined first. To draw conclusions about the electrolyte, both electrodes are measured with and without a previous washing step as described in Section 3. One peak centred around 531.5 eV in the O(1s) spectrum is characteristic for a mix of O=C and Li_2CO_3, typical components in cells with EC/DMC as solvent. Therefore, the results reveal an electrolyte likely based on EC/DMC with $LiPF_6$ as conducting salt and sulphur additives to stabilise the SEI. In addition, only the electrodes of HI0/50°C are initially examined to determine whether significant differences over the length of the cell exist for the highest temperature difference.

On all electrode samples, survey XPS spectra reveal the presence of six main elements, which are carbon (C1s), oxygen (O1s), fluorine (F1s), phosphorus (P2p), sulphur (S2p), and lithium (Li1s). However, the elements from the cathode active material are not observed on survey spectra, suggesting the presence of a surface layer on the cathode in its BoL state.

According to the XPS results, the surface layer composition at the electrode-electrolyte interface is similar for anode and cathode. Salt, LiF and Li_2CO_3 are present on all samples, so their concentration was chosen as an indicator for the temperature influence. The results are shown in Figure 36. In the anode case in Figure 36 a), a slight decrease of Li_2CO_3 related to more solvent degradation is observed when temperature increases despite its random variation. Yet, this enhanced degradation at a lower temperature is counterintuitive as

increased temperature means accelerated reactions and, therefore, the same products [185] in higher concentrations. Chang et al. [146] gained similar results and assumed a further decomposition of Li_2CO_3. In contrast, there is no significant difference in the amount of Li_2CO_3 on the cathode in Figure 36 c).

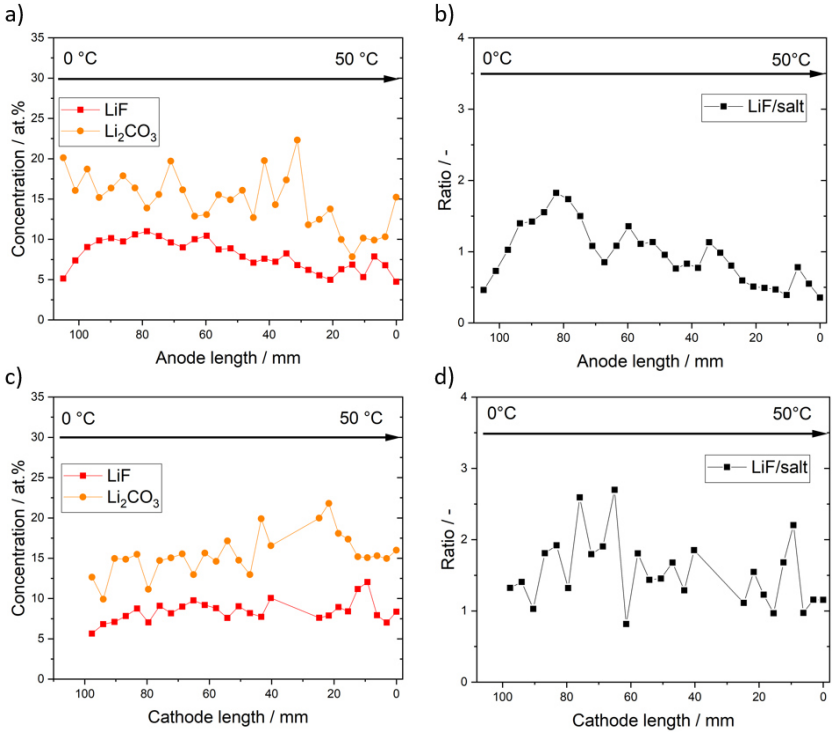

Figure 36. Variation of LiF and Li_2CO_3 on the a) anode and c) cathode and the variation of LiF/salt ratio on the b) anode and d) cathode as a function of temperature.

In DMC with $LiPF_6$ present and at elevated temperatures, Li_2CO_3 degrades to CO_2, LiF, and F_2PO_2Li [292]. On the anode in Figure 36 b), the LiF amount increases with decreasing temperature until the concentration declines at a low temperature until it is almost the same at 0 °C as at 50 °C. One possibility may be an SEI layer that is less stable at colder temperatures, resulting in a continuous re-formation consuming electrolyte. However, the high concentration of

lithium and phosphorus in the warm part of the electrode measured by ICP-OES is contradictory. A significant amount of SEI is probably formed in the bulk of the electrode and is thus not detectable by XPS. There is no clear influence of high temperature on LiF variation on the cathode but a similar decline at low temperatures as on the anode.

The variation of LiF/salt ratio is a good indication for salt degradation. However, it does not correlate with temperature on the cathode in Figure 36 d). The ratio increases with decreasing temperature on the anode in Figure 36 b) until it reaches a maximum at a temperature close to 10 °C when a linear gradient is assumed. At this point, a large proportion of LiF in the fluorine signal is present on the surface of the electrode. After this maximum, there is a sharp decrease in this ratio as the temperature decreases further. These results clearly indicate that at the extreme temperatures of 0 °C and 50 °C, the proportion of salt consumed is low or the crystallisation of the salt reduces its reactivity. However, this study suggests a better reactivity and faster degradation of salt at low temperatures in the range of 0 °C < T < 10 °C. This would mean the degradation is reduced both at higher and lower temperatures, although it is expected to be enhanced at elevated temperatures [206]. If decomposition is indeed most severe at intermediate temperatures, it surely depends on which reaction steps are rate-determining at the different temperatures. One uncertainty in interpreting the XPS results arises from the uneven removal of conductive salt residues and other surface components during the washing step with DMC. When the active material was detached with NMP to construct the experimental cells, it adhered considerably stronger to the warm areas. Thus, the higher conductive salt concentration in the warm part of the electrodes could be explained by increased adhesion and less effective washing with DMC and might have nothing to do with the ageing itself. Similar to the SEM micrographs, there seems to be no severe SEI formation on the anode surface at elevated temperatures. This supports the assumption that the weight and thickness increase originates in the bulk of the electrode. More PVDF is detected in the cold part of the cathode surface, indicating a lower surface layer thickness there. Comparing the reaction products on the electrodes, there is more degradation at the cathode surface.

Additionally, XPS revealed more decomposition products of the sulphur additive at high temperatures on both anode and cathode, indicating a higher degradation of this additive.

Although the results show an influence of temperature on salt degradation, a conclusive interpretation even for the extremely high temperature difference of 50 K over the length of the cell is hardly possible. Therefore, the measurement and interpretation effort is not justified and has not been pursued for the other thermal boundary conditions.

5.6 Interim Conclusion

Post-mortem analysis reveals significant variations on the electrode and atomic scale for the different thermal boundary conditions during cycling. The cell cycled at a homogeneous temperature of 0 °C shows less change than expected, considering that this temperature is most suitable for plating. The cells at a low temperature level benefit from the CC cycling without CV phase since the high SoC, which is critical for plating, is avoided by reaching the voltage limits early. Thus, temperature and voltage effects cannot be separated completely. For example, the particle fracture and reduced cohesion of the NCA secondary particles at 50 °C cycling can be attributed to the higher SoC reached due to the higher temperature.

The influence of temperature gradients on the anode is already obvious at the cell opening. Lithium plating is visible as silverish deposition on the anode surface in the cold part up to about 12 °C. The differences between warm cell regions and cold ones are also apparent in the specific electrode weight and layer thickness. While the layer thickness of the anode with homogeneous temperature control matches that at the corresponding temperature with the gradient applied, the specific weight for the anode cycled under a temperature gradient is generally increased. Still, the tendency of increasing weight with increasing temperature is evident. This is attributed to enhanced SEI growth at higher temperatures and is supported by the increased lithium and phosphorus

concentration at the anode found by ICP-OES. Besides, there is a higher proportion of especially cobalt on the anode side at high temperatures, potentially further accelerating SEI growth and electrolyte decomposition. This is not consistent with the results from XPS and the SEM images of the surface. Both do not show an increased concentration of decomposition products or a severe surface layer formation. Possibly, a greater proportion of the SEI is formed in the bulk of the electrode and is thus not detectable by either XPS or SEM. Unfortunately, the changes in porosity cannot be reliably determined to confirm or disprove this hypothesis. The transition metals on the anode at high temperatures suggest that they promote their dissolution at the cathode. There, the crystal lattice becomes more distorted at elevated temperatures, which is probably due to lower lithium concentrations and indicates a loss of capacity. Additional signs of mechanical degradation appear in the SEM cross-sections, indicating a reduced cohesion of the NCA secondary particles up to particle fracture. NCA is clearly more affected by the mentioned changes than LCO. Both, ICP-OES and XRD show the same results for high and low temperatures whether a temperature gradient was applied or not.

Overall, the results illustrate a distinct temperature dependency of the various ageing mechanisms. With an applied temperature gradient, these occur accordingly inhomogeneously and induce an inhomogeneous ageing behaviour in the cell. However, this is limited to the electrode level and does not affect the cells capacity fade and impedance increase, as shown in Section 5.1. Thus, the hypothesis proposed in Section 5.1 that the slope of the linear part of the ageing trend is due to the ageing on the cathode side is not tenable. Furthermore, the inhomogeneity is provoked by extreme gradients with temperature differences of 25 K and 50 K over the length of the cell. Assumably the statistical distribution of all the mechanisms would diminish the measurable effect if the temperature differences were considerably smaller. However, none of the cells has reached the knee point, from which ageing accelerates dramatically, an effect also known as sudden death. Therefore, it cannot be excluded that despite similar ageing with and without temperature gradients, this transition point is reached earlier in the cells with gradient and inhomogeneous ageing effects. So even with the temperature-dependent alterations during ageing revealed by

the post-mortem analysis, a maximum temperature difference over the length of the cell can not be defined.

Temporal temperature changes provoke a completely different ageing behaviour. This has been observed for capacity fade and impedance increase in Section 5.1 and is consistently confirmed by the methods of post-mortem analysis. At cell opening, HT0/50°C shows the greatest amount of lithium plating and dead lithium, followed by HT25/50°C. In ICP-OES, the amount of lithium and phosphorus is also significantly increased for both cells, and the layer thickness of the anode increases excessively. This is consistent with the results of the differential methods, where a large shift in electrode balancing suggests LLI and both DVA and ICA exhibit strong alteration compared to BoL. The lattice parameters of the cathode also change the most for these two cells. While increased ageing occurs for temperature changes over the entire temperature range or at a high temperature level, it is consistently much milder for HT0/25°C than the average temperature would dictate. The most significant ageing mechanism at cold temperatures is plating. However, this is not limited to these conditions but also occurs at high temperatures. Looking for explanations why temporal temperature changes cause a different ageing behaviour, the thermal expansion coefficients of the components are a natural starting point. These are between 55 µm/K and 66 µm/K for graphite, depending on the degree of intercalation [293]. For NCA and LCO, there is no literature data, but for the whole cell, values range from 1.1 µm/K (LCO/C) [294] to 5.49 µm/K (NMC/C) [295]. These values are large enough to induce mechanical stress inside the cell. Whether these actually contribute cannot be conclusively clarified here. The fact that ageing is accelerated at moderate and high temperatures, but is milder at HT0/25°C, although the expansion coefficients are constant over the entire temperature range, contradicts this hypothesis.

It can be stated that the most relevant ageing mechanisms are LLI at the anode and the loss of adhesion between secondary particles at the cathode. Harlow et al. [162] suggest monocrystals as cathode active material to prevent particle cracking and state that a rapid formation of a stable SEI is a requirement for a long lifetime of the battery cell as it impedes loss of active lithium. The result presented in this Section support this hypothesis.

6 Conclusion

In this work, the impact of temperature inhomogeneities on the performance and lifetime of LIB was assessed experimentally. Literature demonstrates the tremendous impact of temperature on both aspects. However, no conclusions have been reached about the quantitative effect of temperature inhomogeneities or what mechanisms they induce. In modules, the maximum temperature difference is commonly limited to 5 K, although there is no explanation or scientific foundation for this value. In contrast, there is no such value regarding temperature inhomogeneities in individual cells altogether. Therefore, this work provides comprehensive scientific discussions to what extent temperature differences over the length of a battery cell lead to inhomogeneous distributions of impedance, current, heat generation and ageing mechanisms within the cell.

A thorough experimental set-up allows thermal boundary conditions to be applied defined and precisely on the cell surface, including temperature gradients and temporal changes. Based on this, the influence of gradients over the cell length on the voltage behaviour during charging and discharging with different current rates as well as on the internal resistance was determined. Together with a newly developed correlation for the temperature-dependent current distribution, differences in the cell behaviour could be explained. The interaction of C-rate, temperature and the overvoltages that occur is decisive for how the cell behaviour changes when temperature gradients are present. Overall, the temperature significantly influences the resistance and current distribution within a cell, but the integral behaviour does not change substantially.

In addition to cell behaviour in terms of voltage characteristics, ageing under various thermal boundary conditions was considered. It was quantified using capacity fade and impedance rise as indicators. For those quantities, a temperature-dependent ageing function was derived that describes the degradation for the stationary conditions even when temperature gradients are present but is not valid when there are temporal temperature changes. Further evaluation and

a post-mortem analysis revealed the inhomogeneous occurrence of ageing mechanisms on electrode level. The ageing mechanisms clearly depend on temperature and affect both anode and cathode. For this purpose, layer thicknesses were measured, and the electrodes were inspected optically and by SEM. In addition, XRD, XPS and ICP-OES analyses were performed to obtain a complete picture of the ageing mechanisms that cause degradation on cell level.

Now, as this is accomplished, the research questions posed at the beginning of this thesis can be answered.

"How do temperature gradients influence the performance of LIB?"

The performance was analysed by means of voltage, resistance and current. The results presented on the discharge characteristics reveal that temperature gradients do hardly impact the cell's overall behaviour. The LIB behaves as if it was warmer or colder than the average temperature suggests, depending on the current rate. A cell (dis-)charged with a current of C/2, at an average temperature below 20 °C and exposed to temperature gradients, behaves as if it was slightly warmer than its average temperature. However, EIS with no significant heat generation indicates that it is not due to an actual higher average temperature. Therefore, the behaviour can be attributed to an asymmetric weighting of the cell regions with different temperatures. The lower resistance at elevated temperatures leads to higher current densities in this region. Thus, the cell performance is dominated by the properties of the warmer cell regions, and the overall cell behaviour is comparable to that of a cell at a higher average temperature. This is not valid when high currents are applied. Then the high overvoltages limit the current not only in the cold but also in the warm regions of the cell. Therefore, the higher temperature does not dominate the cell's behaviour but only compensates for the smaller current density at low temperatures.

It was demonstrated that temperature and temperature inhomogeneities have a substantial effect on the internal resistance and current distribution, which was quantified. How exactly this influence occurs depends on the temperature level, the temperature differences as well as the overall current. Therefore, a

universal statement on the consequences of temperature gradients compared to a homogeneous average temperature is not possible based on the results of this work. However, it can be concluded that temperature gradients over the length of the cell only marginally affect its overall performance. Thus, despite its high temperature sensitivity, the overall influence of temperature gradients on the performance is not significant enough to require a limitation of temperature differences along the cell stack and the individual electrode layers. Thus, the typical value for the maximum temperature difference of 5 K for modules cannot serve as an orientation for single cell behaviour but is questioned by the results obtained in this thesis.

"How do temperature and heat generation interact?"

In this thesis, correlations were derived that describe the internal resistance and the current solely depending on temperature. Therefore, the temperature-dependent heat generation can be calculated. With a temperature gradient present, the heat generation is distributed, but overall it equals the one at the respective homogeneous average temperature as thermal simulations demonstrated. Against the general assumption of a positive feedback mechanism, the results reveal a declining heat generation for C/2 for increasing temperature and a maximum heat generation at 15 °C for 3C, which is decreasing both for higher and lower temperatures. This means the temperature-dependent heat source term is dominated by resistance, i.e. Joule heating at higher temperatures, while the lower current density is relevant at low temperatures. Via these coherencies, safety aspects are addressed, and no safety-critical concerns associated with temperature gradients can be identified here. It should also be noted that in this consideration, no heat generation of side reactions is taken into account. This would modify the heat generation and probably increase it by an unknown amount, which increases for higher temperatures when the reactions accelerate.

"Does an inhomogeneous temperature distribution lead to locally different ageing effects?"

Yes.

The overall ageing behaviour with capacity fade and impedance increase is not significantly influenced by temperature gradients. Instead, these cells age according to their average temperature. Nevertheless, different ageing mechanisms appear locally on the electrode and particle level. Those effects were analysed and evaluated regarding their homogeneity in a post-mortem analysis. The cells with and without temperature gradient revealed temperature-dependent ageing phenomena. They occurred likewise at the cells cycled at a homogenous temperature and the cell parts with the respective temperature when a gradient was applied. At cold temperatures, mainly lithium plating occurred, while high temperatures induce increased SEI formation and solvent co-intercalation in the bulk of the anode. Both lead to LLI, which is the main degradation mode for all investigated thermal boundary conditions during cycling. The cathode is more susceptible to ageing at high temperatures, which enhance transition metal dissolution and distort the crystal lattice. For the huge temperature difference between which the gradient was applied in this work, the temperature dependency was revealed clearly. Still, the statistical distribution of all mechanisms would diminish the measurable effect if the temperature difference was considerably smaller. Temperature gradients over the length of the cell seem to have a minor impact on the overall ageing that is relevant from an application point of view. However, none of the cells has reached the knee point, from which ageing accelerates dramatically. Therefore, it cannot be excluded that despite similar ageing with and without temperature gradients, this transition point is reached earlier in the cells with gradient and inhomogeneous ageing effects. So even with the temperature-dependent alterations during ageing revealed by the post-mortem analysis, a maximum temperature difference over the length of the cell can not be defined.

And what about temporal temperature changes?

Temporal temperature changes during cycling clearly initiate a different behaviour than homogeneous temperature or temperature gradients. The changes over the complete temperature range (HT0/50°C) and those on the high temperature level (HT25/50°C) accelerated all ageing effects investigated here, leading to a faster capacity fade and impedance increase represented in corre-

lation to EAT. Astonishing was the massive amount of dead lithium found beside the anode sheet close to the cathode tab. In contrast, cells exposed to temperature changes between 0 °C and 25 °C showed, together with the homogeneous stationary condition (HS25°C), the least degradation.

Other authors [145, 146] likewise observe accelerated ageing under electrical load combined with a transient temperature. However, potential explanations for this behaviour are not provided.

And what now?

The results presented in this thesis allay all concerns regarding a potential effect of temperature differences reducing performance and capacity during operation, deteriorating lifetime or even leading to safety-critical conditions. Instead, temperature gradients over the cell length hardly impact its overall behaviour, and only on electrode and particle level an inhomogeneity in ageing mechanisms is observed. However, there is one indication in literature on the effect of surface and tab cooling on ageing, suggesting that the direction of the gradient is important [141]. This difference may also exist in performance behaviour and must be reflected when evaluating these results. In further studies, the impact of temperature gradients across the cell thickness and the individual layers, as well as over modules or packs, should be focused on to gain a deeper understanding of temperature inhomogeneities and to verify whether a maximum temperature difference exists for those cases. Additionally, transient temperatures need to be addressed in more detail to elaborate on the ageing mechanisms that induce the clearly observed accelerated degradation.

References

[1] ‘Klimaschutzplan 2050 - Klimaschutzpolitische Grundsätze und Ziele der Bundesregierung’. Bundesministerium für Umwelt, Naturschutz und nukleare Sicherheit (BMU), 2016.

[2] B. Scrosati, J. Garche, and W. Tillmetz, *Advances in Battery Technologies for Electric Vehicles*. 2015. doi: 10.1016/B978-1-78242-377-5.00010-8.

[3] R. Korthauer, *Lithium-ion batteries: Basics and applications*. Springer, 2018. doi: 10.1007/978-3-662-53071-9.

[4] G. J. Offer, T. S. O´Connor, and M. De Marco, ‘Opportunities for Disruptive Advances through Engineering for Next Generation Energy Storage’. 2020. doi: 10.5281/zenodo.3931338.

[5] ‘Global EV Outlook 2020’, International Energy Agency, 2020.

[6] M. Li, J. Lu, Z. Chen, and K. Amine, ‘30 Years of Lithium-Ion Batteries’, *Adv. Mater.*, vol. 30, no. 33, p. 1800561, Aug. 2018, doi: 10.1002/adma.201800561.

[7] J. C. Burns *et al.*, ‘Predicting and Extending the Lifetime of Li-Ion Batteries’, *Journal of The Electrochemical Society*, vol. 160, no. 9, pp. A1451–A1456, 2013, doi: 10.1149/2.060309jes.

[8] United States Council for Automotive Research LLC, ‘USCAR: Energy Storage System Goals’. http://uscar.org/guest/article_view.php?articles_id=85 (accessed Jul. 12, 2021).

[9] G. Offer, Y. Patel, A. Hales, L. B. Diaz, and M. Marzook, ‘Cool metric for lithium-ion batteries could spur progress’, *Nature*, vol. 582, pp. 485–487, 2020, doi: 10.1038/d41586-020-01813-8.

[10] G. Xia, L. Cao, and G. Bi, ‘A review on battery thermal management in electric vehicle application’, *Journal of Power Sources*, vol. 367, pp. 90–105, 2017, doi: 10.1016/j.jpowsour.2017.09.046.

[11] A. Pesaran, S. Santhanagopalan, and G.-H. Kim, ‘Addressing the impact of temperature extremes on large format li-ion batteries for vehicle applications’, presented at the 30th International Battery Seminar, Ft. Lauderdale, Florida, 2013.

[12] M. Fleckenstein, O. Bohlen, and B. Bäker, ‘Aging Effect of Temperature Gradients in Li-ion Cells Experimental and Simulative Investigations and the Consequences on Thermal Battery

Management', *WEVJ*, vol. 5, no. 2, pp. 322–333, Jun. 2012, doi: 10.3390/wevj5020322.

[13] T. Waldmann *et al.*, 'Influence of Cell Design on Temperatures and Temperature Gradients in Lithium-Ion Cells: An In Operando Study', *Journal of The Electrochemical Society*, vol. 162, no. 6, pp. A921–A927, 2015, doi: 10.1149/2.0561506jes.

[14] T. M. Bandhauer, S. Garimella, and T. F. Fuller, 'A Critical Review of Thermal Issues in Lithium-Ion Batteries', *J. Electrochem. Soc.*, vol. 158, no. 3, p. R1, 2011, doi: 10.1149/1.3515880.

[15] M. R. Palacín, 'Understanding ageing in Li-ion batteries: A chemical issue', *Chemical Society Reviews*, vol. 47, no. 13, pp. 4924–4933, 2018, doi: 10.1039/c7cs00889a.

[16] M. Klein, S. Tong, and J. W. Park, 'In-plane nonuniform temperature effects on the performance of a large-format lithium-ion pouch cell', *Applied Energy*, vol. 165, pp. 639–647, Mar. 2016, doi: 10.1016/j.apenergy.2015.11.090.

[17] K. P. Birke, Ed., *Modern battery engineering: a comprehensive introduction*. New Jersey: World Scientific, 2019.

[18] D. Berndt and D. Spahrbier, *Batteries*. Weinheim, Germany: Wiley-VCH Verlag GmbH & Co. KGaA, 2001. doi: 10.1002/14356007.a03_343.

[19] J. Dahn and G. M. Ehrlich, 'Section A: Lithium-ion Batteries', McGraw-Hill Education. [Online]. Available: 10.1038/nenergy.2016.119

[20] M. Junker, S. Bihn, and D. U. Sauer, 'Analyse von neuen Zell-Technologien und deren Auswirkungen auf das Gesamtsystem Batteriepack', *Forschungsvereinigung Automobiltechnik*, vol. 337, 2020.

[21] E. Antolini, 'LiCoO2: formation, structure, lithium and oxygen nonstoichiometry, electrochemical behaviour and transport properties', *Solid State Ionics*, vol. 170, no. 3–4, pp. 159–171, May 2004, doi: 10.1016/j.ssi.2004.04.003.

[22] R. Hausbrand *et al.*, 'Fundamental degradation mechanisms of layered oxide Li-ion battery cathode materials: Methodology, insights and novel approaches', *Materials Science and Engineering B: Solid-State Materials for Advanced Technology*, vol. 192, no. C, 2015, doi: 10.1016/j.mseb.2014.11.014.

[23] W. M. Dose, C. Xu, C. P. Grey, and M. F. L. De Volder, 'Effect of Anode Slippage on Cathode Cutoff Potential and Degradation Mechanisms in Ni-Rich Li-Ion Batteries', *Cell Reports Physical*

Science, vol. 1, no. 11, p. 100253, Nov. 2020, doi: 10.1016/j.xcrp.2020.100253.

[24] K. G. Gallagher, D. W. Dees, A. N. Jansen, D. P. Abraham, and S.-H. Kang, 'A Volume Averaged Approach to the Numerical Modeling of Phase-Transition Intercalation Electrodes Presented for Li $_x$ C $_6$', *J. Electrochem. Soc.*, vol. 159, no. 12, pp. A2029–A2037, 2012, doi: 10.1149/2.015301jes.

[25] J. Schmalstieg, 'Physikalisch-elektrochemische Simulation von Lithium-Ionen-Batterien', RWTH Aachen University, Aachen, 2017.

[26] K. Xu, 'Nonaqueous Liquid Electrolytes for Lithium-Based Rechargeable Batteries', *Chem. Rev.*, vol. 104, no. 10, pp. 4303–4418, Oct. 2004, doi: 10.1021/cr030203g.

[27] J. P. Schmidt, 'Verfahren zur Charakterisierung und Modellierung von Lithium-Ionen Zellen', KIT Scientific Publishing, 2013.

[28] I. Bloom *et al.*, 'Differential voltage analyses of high-power lithium-ion cells 1. Technique and application', *Journal of Power Sources*, vol. 139, no. 1–2, pp. 295–303, Jan. 2005, doi: 10.1016/j.jpowsour.2004.07.021.

[29] M. Dubarry, A. Devie, and B. Y. Liaw, 'The Value of Battery Diagnostics and Prognostics', *Journal of Energy and Power Sources*, vol. 1, no. 5, pp. 242–249, 2014.

[30] K. Honkura, H. Honbo, Y. Koishikawa, and T. Horiba, 'State Analysis of Lithium-Ion Batteries Using Discharge Curves', *ECS Transactions*, vol. 13, no. 19, pp. 61–73, 2008, doi: 10.1149/1.3018750.

[31] X. Feng *et al.*, 'A reliable approach of differentiating discrete sampled-data for battery diagnosis', *eTransportation*, vol. 3, p. 16, 2020, doi: 10.1016/j.etran.2020.100051.

[32] Gamry Instruments, 'Basics of Electrochemical Impedance Spectroscopy', Gamry, Application Note, 2010. doi: 10.1152/ajpregu.00432.2003.

[33] D. Andre, M. Meiler, K. Steiner, C. Wimmer, T. Soczka-Guth, and D. U. Sauer, 'Characterization of high-power lithium-ion batteries by electrochemical impedance spectroscopy. I. Experimental investigation', *Journal of Power Sources*, vol. 196, no. 12, pp. 5334–5341, 2011, doi: 10.1016/j.jpowsour.2010.12.102.

[34] T. Osaka, D. Mukoyama, and H. Nara, 'Review—Development of Diagnostic Process for Commercially Available Batteries, Especially Lithium Ion Battery, by Electrochemical Impedance Spectroscopy',

Journal of The Electrochemical Society, vol. 162, no. 14, pp. A2529–A2537, 2015, doi: 10.1149/2.0141514jes.

[35] H. Göhr, 'About Contributions of Certain Electrode Processes to the Impedance', *Benutzerhandbuch Zahner IM6*, 1999.

[36] S. Gantenbein, M. Weiss, and E. Ivers-Tiffée, 'Impedance based time-domain modeling of lithium-ion batteries: Part I', *Journal of Power Sources*, vol. 379, pp. 317–327, 2018, doi: 10.1016/j.jpowsour.2018.01.043.

[37] E. Barsoukov and J. R. Macdonald, *Impedance Spectroscopy*. 2005. [Online]. Available: http://doi.wiley.com/10.1002/0471716243

[38] B. A. Boukamp, 'A Linear Kronig-Kramers Transform Test for Immittance Data Validation', *J. Electrochem. Soc.*, vol. 142, no. 6, pp. 1885–1894, Jun. 1995, doi: 10.1149/1.2044210.

[39] C. F. Bohren, 'What did Kramers and Kronig do and how did they do it?', *Eur. J. Phys.*, vol. 31, no. 3, pp. 573–577, May 2010, doi: 10.1088/0143-0807/31/3/014.

[40] M. Schönleber, D. Klotz, and E. Ivers-Tiffée, 'A Method for Improving the Robustness of linear Kramers-Kronig Validity Tests', *Electrochimica Acta*, vol. 131, pp. 20–27, Jun. 2014, doi: 10.1016/j.electacta.2014.01.034.

[41] D. Andre, M. Meiler, K. Steiner, H. Walz, T. Soczka-Guth, and D. U. Sauer, 'Characterization of high-power lithium-ion batteries by electrochemical impedance spectroscopy. II: Modelling', *Journal of Power Sources*, vol. 196, no. 12, pp. 5349–5356, 2011, doi: 10.1016/j.jpowsour.2010.07.071.

[42] S. Cooper, 'Introduction to Electrochemical Impedance Spectroscopy (EIS: Maths and Theory)', presented at the Electrochemistry Network, Imperial College London, Feb. 18, 2021. Accessed: Mar. 11, 2021. [Online]. Available: https://www.youtube.com/watch?v=5puDQjCl2pk

[43] C. Pastor-Fernández, K. Uddin, G. H. Chouchelamane, W. D. Widanage, and J. Marco, 'A Comparison between Electrochemical Impedance Spectroscopy and Incremental Capacity-Differential Voltage as Li-ion Diagnostic Techniques to Identify and Quantify the Effects of Degradation Modes within Battery Management Systems', *Journal of Power Sources*, vol. 360, pp. 301–318, 2017, doi: 10.1016/j.jpowsour.2017.03.042.

[44] B. Stiaszny, J. C. Ziegler, E. E. Krauß, J. P. Schmidt, and E. Ivers-Tiffée, 'Electrochemical characterization and post-mortem analysis of aged LiMn 2O4-NMC/graphite lithium ion batteries part I: Cycle

aging', *Journal of Power Sources*, vol. 251, pp. 439–450, 2014, doi: 10.1016/j.jpowsour.2013.11.080.

[45] B. Stiaszny, J. C. Ziegler, E. E. Krauß, M. Zhang, J. P. Schmidt, and E. Ivers-Tiffée, 'Electrochemical characterization and post-mortem analysis of aged LiMn 2O4-NMC/graphite lithium ion batteries part II: Calendar aging', *Journal of Power Sources*, vol. 258, pp. 61–75, 2014, doi: 10.1016/j.jpowsour.2014.02.019.

[46] Y. Wu, P. Keil, S. F. Schuster, and A. Jossen, 'Impact of Temperature and Discharge Rate on the Aging of a LiCoO2/LiNiCoAl Lithium-Ion Pouch Cell', *J. Electrochem. Soc.*, vol. 164, no. 7, pp. A1438–A1445, 2017, doi: 10.1149/2.0401707jes.

[47] J. Li, E. Murphy, J. Winnick, and P. A. Kohl, 'Studies on the cycle life of commercial lithium ion batteries during rapid charge–discharge cycling', *Journal of Power Sources*, vol. 102, no. 1–2, pp. 294–301, Dec. 2001, doi: 10.1016/S0378-7753(01)00821-7.

[48] Y. Troxler *et al.*, 'The effect of thermal gradients on the performance of lithium-ion batteries', *Journal of Power Sources*, vol. 247, pp. 1018–1025, 2014, doi: 10.1016/j.jpowsour.2013.06.084.

[49] N. S. Spinner, C. T. Love, S. L. Rose-Pehrsson, and S. G. Tuttle, 'Expanding the Operational Limits of the Single-Point Impedance Diagnostic for Internal Temperature Monitoring of Lithium-ion Batteries', *Electrochimica Acta*, vol. 174, pp. 488–493, Aug. 2015, doi: 10.1016/j.electacta.2015.06.003.

[50] J. P. Schmidt, S. Arnold, A. Loges, D. Werner, T. Wetzel, and E. Ivers-Tiffée, 'Measurement of the internal cell temperature via impedance: Evaluation and application of a new method', *Journal of Power Sources*, vol. 243, pp. 110–117, Dec. 2013, doi: 10.1016/j.jpowsour.2013.06.013.

[51] J. G. Zhu, Z. C. Sun, X. Z. Wei, and H. F. Dai, 'A new lithium-ion battery internal temperature on-line estimate method based on electrochemical impedance spectroscopy measurement', *Journal of Power Sources*, vol. 274, pp. 990–1004, Jan. 2015, doi: 10.1016/j.jpowsour.2014.10.182.

[52] R. R. Richardson, P. T. Ireland, and D. A. Howey, 'Battery internal temperature estimation by combined impedance and surface temperature measurement', *Journal of Power Sources*, vol. 265, pp. 254–261, Nov. 2014, doi: 10.1016/j.jpowsour.2014.04.129.

[53] L. H. J. Raijmakers, D. L. Danilov, J. P. M. van Lammeren, M. J. G. Lammers, and P. H. L. Notten, 'Sensorless battery temperature measurements based on electrochemical impedance spectroscopy',

Journal of Power Sources, vol. 247, pp. 539–544, Feb. 2014, doi: 10.1016/j.jpowsour.2013.09.005.

[54] H. P. G. J. Beelen, L. H. J. Raijmakers, M. C. F. Donkers, P. H. L. Notten, and H. J. Bergveld, 'A comparison and accuracy analysis of impedance-based temperature estimation methods for Li-ion batteries', *Applied Energy*, vol. 175, pp. 128–140, Aug. 2016, doi: 10.1016/j.apenergy.2016.04.103.

[55] H. P. G. J. Beelen, K. Shivakumar, L. H. J. Raijmakers, M. C. F. Donkers, and H. J. Bergveld, 'Towards impedance-based temperature estimation for Li-ion battery packs', *International Journal of Energy Research*, vol. 44, 2020, doi: 10.1002/er.5107.

[56] O. US EPA, 'EPA US06 or Supplemental Federal Test Procedures (SFTP)', *US EPA*, Dec. 22, 2015. https://www.epa.gov/emission-standards-reference-guide/epa-us06-or-supplemental-federal-test-procedures-sftp (accessed May 20, 2021).

[57] D. Bernardi, E. Pawlikowski, and J. Newman, 'A General Energy Balance for Battery Systems', *J. Electrochem. Soc.*, vol. 132, no. 1, pp. 5–12, Jan. 1985, doi: 10.1149/1.2113792.

[58] M. Alipour, C. Ziebert, F. V. Conte, and R. Kizilel, 'A Review on Temperature-Dependent Electrochemical Properties, Aging, and Performance of Lithium-Ion Cells', *Batteries*, vol. 6, no. 3, Jun. 2020, doi: 10.3390/batteries6030035.

[59] AVID Technology, '#52 | Interview - Dr Greg Offer, Imperial College London, Battery Technology', Jun. 17, 2020. Accessed: Feb. 19, 2021. [Online]. Available: https://www.youtube.com/watch?v=6873r_D6ZAM

[60] S. Arrhenius, 'Über die Reaktionsgeschwindigkeit bei der Inversion von Rohrzucker durch Säuren', *Zeitschrift für Physikalische Chemie*, vol. 4, p. 226, 1889, doi: papers2://publication/uuid/C41B4C56-D5FD-416F-BFB5-841B515B52AC.

[61] A. Jossen and W. Weydanz, *Moderne Akkumulatoren richtig einsetzen*, 2. überarbeitete Auflage, Unverändert zur 2. Auflage vom Februar 2019. Göttingen: MatrixMedia, 2021.

[62] T. L. Kulova, A. M. Skundin, E. A. Nizhnikovskii, and A. V. Fesenko, 'Temperature effect on the lithium diffusion rate in graphite', *Russ J Electrochem*, vol. 42, no. 3, pp. 259–262, Mar. 2006, doi: 10.1134/S1023193506030086.

[63] P. Porion, Y. R. Dougassa, C. Tessier, L. El Ouatani, J. Jacquemin, and M. Anouti, 'Comparative study on transport properties for LiFAP and LiPF6 in alkyl-carbonates as electrolytes through conductivity,

viscosity and NMR self-diffusion measurements', *Electrochimica Acta*, vol. 114, pp. 95–104, Dec. 2013, doi: 10.1016/j.electacta.2013.10.015.

[64] S. S. Zhang, K. Xu, and T. R. Jow, 'The low temperature performance of Li-ion batteries', *Journal of Power Sources*, vol. 115, no. 1, pp. 137–140, Mar. 2003, doi: 10.1016/S0378-7753(02)00618-3.

[65] C.-K. Huang, J. S. Sakamoto, J. Wolfenstine, and S. Surampudi, 'The Limits of Low-Temperature Performance of Li-Ion Cells', *Journal of The Electrochemical Society*, vol. 147, no. 8, pp. 2893–2896, 2000.

[66] A. Tomaszewska *et al.*, 'Lithium-ion battery fast charging: A review', *eTransportation*, vol. 1, p. 100011, Aug. 2019, doi: 10.1016/j.etran.2019.100011.

[67] C. Xu *et al.*, 'Bulk fatigue induced by surface reconstruction in layered Ni-rich cathodes for Li-ion batteries', *Nat. Mater.*, vol. 20, no. 1, pp. 84–92, Jan. 2021, doi: 10.1038/s41563-020-0767-8.

[68] D. Werner, S. Paarmann, A. Wiebelt, and T. Wetzel, 'Inhomogeneous Temperature Distribution Affecting the Cyclic Aging of Li-Ion Cells. Part I: Experimental Investigation', *Batteries*, vol. 6, no. 1, Feb. 2020, doi: 10.3390/batteries6010013.

[69] T. Grandjean, A. Barai, E. Hosseinzadeh, Y. Guo, A. McGordon, and J. Marco, 'Large format lithium ion pouch cell full thermal characterisation for improved electric vehicle thermal management', *Journal of Power Sources*, vol. 359, pp. 215–225, Aug. 2017, doi: 10.1016/j.jpowsour.2017.05.016.

[70] C. Heubner, M. Schneider, C. Lämmel, U. Langklotz, and A. Michaelis, 'In-operando temperature measurement across the interfaces of a lithium-ion battery cell', *Electrochimica Acta*, vol. 113, pp. 730–734, 2013, doi: 10.1016/j.electacta.2013.08.091.

[71] C. Heubner, M. Schneider, C. Lämmel, and A. Michaelis, 'Local heat generation in a single stack lithium ion battery cell', *Electrochimica Acta*, vol. 186, pp. 404–412, 2015, doi: 10.1016/j.electacta.2015.10.182.

[72] R. Srinivasan, 'The five modes of heat generation in a Li-ion cell under discharge', *Journal of Power Sources*, 2014.

[73] D.-C. Lee, J.-J. Lee, J.-S. Kim, S. Cho, and C.-W. Kim, 'Thermal behaviors analysis of 55 Ah large-format lithium-ion pouch cells with different cell aspect ratios, tab locations, and C-rates', *Applied*

Thermal Engineering, vol. 175, p. 115422, 2020, doi: 10.1016/j.applthermaleng.2020.115422.

[74] V. V. Viswanathan *et al.*, 'Effect of entropy change of lithium intercalation in cathodes and anodes on Li-ion battery thermal management', *Journal of Power Sources*, vol. 195, no. 11, pp. 3720–3729, Jun. 2010, doi: 10.1016/j.jpowsour.2009.11.103.

[75] C. Veth, D. Dragicevic, R. Pfister, S. Arakkan, and C. Merten, '3D Electro-Thermal Model Approach for the Prediction of Internal State Values in Large-Format Lithium Ion Cells and Its Validation', *J. Electrochem. Soc.*, vol. 161, no. 14, pp. A1943–A1952, 2014, doi: 10.1149/2.1201412jes.

[76] M. Fleckenstein, O. Bohlen, M. A. Roscher, and B. Bäker, 'Current density and state of charge inhomogeneities in Li-ion battery cells with LiFePO4 as cathode material due to temperature gradients', *Journal of Power Sources*, vol. 196, no. 10, pp. 4769–4778, May 2011, doi: 10.1016/j.jpowsour.2011.01.043.

[77] O. Schmidt, M. Thomitzek, F. Röder, S. Thiede, C. Herrmann, and U. Krewer, 'Modeling the Impact of Manufacturing Uncertainties on Lithium-Ion Batteries', *J. Electrochem. Soc.*, vol. 167, no. 6, p. 060501, Mar. 2020, doi: 10.1149/1945-7111/ab798a.

[78] L. Chang, 'Correlations of cell-to-cell parameter variations on current and state-of-charge distributions within parallel-connected lithium-ion cells', *Journal of Power Sources*, vol. 437, p. 10, 2019.

[79] T. Bruen and J. Marco, 'Modelling and experimental evaluation of parallel connected lithium ion cells for an electric vehicle battery system', *Journal of Power Sources*, vol. 310, p. 11, 2016.

[80] S. Kamalisiahroudi, J. Huang, Z. Li, and J. Zhang, 'Study of Temperature Difference and Current Distribution in Parallel-Connected Cells at Low Temperature', vol. 8, no. 10, 2014.

[81] M. H. Hofmann *et al.*, 'Dynamics of current distribution within battery cells connected in parallel', *Journal of Energy Storage*, vol. 20, pp. 120–133, Dec. 2018, doi: 10.1016/j.est.2018.08.013.

[82] A. Fill, S. Koch, A. Pott, and K.-P. Birke, 'Current distribution of parallel-connected cells in dependence of cell resistance, capacity and number of parallel cells', *Journal of Power Sources*, vol. 407, pp. 147–152, Dec. 2018, doi: 10.1016/j.jpowsour.2018.10.061.

[83] M. P. Klein and J. W. Park, 'Current Distribution Measurements in Parallel-Connected Lithium-Ion Cylindrical Cells under Non-

Uniform Temperature Conditions', *J. Electrochem. Soc.*, vol. 164, no. 9, pp. A1893–A1906, 2017, doi: 10.1149/2.0011709jes.

[84] G. M. Cavalheiro, T. Iriyama, G. J. Nelson, S. Huang, and G. Zhang, 'Effects of Nonuniform Temperature Distribution on Degradation of Lithium-Ion Batteries', *Journal of Electrochemical Energy Conversion and Storage*, vol. 17, 2020.

[85] G. Zhang, C. E. Shaffer, C.-Y. Wang, and C. D. Rahn, 'In-Situ Measurement of Current Distribution in a Li-Ion Cell', *J. Electrochem. Soc.*, vol. 160, no. 4, pp. A610–A615, 2013, doi: 10.1149/2.046304jes.

[86] G. Zhang, C. E. Shaffer, C.-Y. Wang, and C. D. Rahn, 'Effects of Non-Uniform Current Distribution on Energy Density of Li-Ion Cells', *Journal of The Electrochemical Society*, 2013.

[87] S. Klink, W. Schuhmann, and F. L. Mantia, 'Vertical Distribution of Overpotentials and Irreversible Charge Losses in Lithium Ion Battery Electrodes', *ChemSusChem*, vol. 7, 2014.

[88] S. V. Erhard *et al.*, 'Simulation and Measurement of the Current Density Distribution in Lithium-Ion Batteries by a Multi-Tab Cell Approach', *Journal of The Electrochemical Society*, vol. 164, no. 1, pp. A6324–A6333, 2017, doi: 10.1149/2.0551701jes.

[89] Y. Zhang, R. Zhao, J. Dubie, T. Jahns, and L. Juang, 'Investigation of current sharing and heat dissipation in parallel-connected lithium-ion battery packs', in *IEEE Energy Conversion Congress and Exposition (ECCE)*, Milwaukee, 2016.

[90] P. J. Osswald, 'Temperature dependency of state of charge inhomogeneities and their equalization in cylindrical lithium-ion cells', *Journal of Power Sources*, vol. 329, 2016.

[91] A. Mistry, C. Fear, R. Carter, C. T. Love, and P. P. Mukherjee, 'Electrolyte Confinement Alters Lithium Electrodeposition', *ACS Energy Lett.*, vol. 4, no. 1, pp. 156–162, Jan. 2019, doi: 10.1021/acsenergylett.8b02003.

[92] H.-H. Huang, H.-Y. Chen, K.-C. Liao, H.-T. Young, C.-F. Lee, and J.-Y. Tien, 'Thermal-electrochemical coupled simulations for cell-to-cell imbalances in lithium-iron-phosphate based battery packs', *Applied Thermal Engineering*, vol. 123, pp. 584–591, Aug. 2017, doi: 10.1016/j.applthermaleng.2017.05.105.

[93] U. S. Kim, J. Yi, C. B. Shin, T. Han, and S. Park, 'Modelling the thermal behaviour of a lithium-ion battery during charge', *Journal of*

Power Sources, vol. 196, no. 11, pp. 5115–5121, Jun. 2011, doi: 10.1016/j.jpowsour.2011.01.103.

[94] B. Wu, Z. Li, and J. Zhang, 'Thermal Design for the Pouch-Type Large-Format Lithium-Ion Batteries: I. Thermo-Electrical Modeling and Origins of Temperature Non-Uniformity', *J. Electrochem. Soc.*, vol. 162, no. 1, pp. A181–A191, 2015, doi: 10.1149/2.0831501jes.

[95] L. Aiello *et al.*, 'In Situ Measurement of Orthotropic Thermal Conductivity on Commercial Pouch Lithium-Ion Batteries with Thermoelectric Device', *Batteries*, vol. 6, no. 10, 2020.

[96] D. Werner, A. Loges, D. J. Becker, and T. Wetzel, 'Thermal conductivity of Li-ion batteries and their electrode configurations – A novel combination of modelling and experimental approach', *Journal of Power Sources*, vol. 364, pp. 72–83, Oct. 2017, doi: 10.1016/j.jpowsour.2017.07.105.

[97] Y. Zhao, Y. Patel, T. Zhang, and G. J. Offer, 'Modeling the Effects of Thermal Gradients Induced by Tab and Surface Cooling on Lithium Ion Cell Performance', *J. Electrochem. Soc.*, vol. 165, no. 13, pp. A3169–A3178, 2018, doi: 10.1149/2.0901813jes.

[98] N. Yang, X. Zhang, G. Li, A. Cai, and Y. Xu, 'Effects of Temperature Differences Among Cells on the Discharging Characteristics of Lithium-Ion Battery Packs with Series/Parallel Configurations during Constant Power Discharge', *Energy Technol.*, vol. 6, no. 6, pp. 1067–1079, Jun. 2018, doi: 10.1002/ente.201700650.

[99] C. Veth, D. Dragicevic, and C. Merten, 'Thermal characterizations of a large-format lithium ion cell focused on high current discharges', *Journal of Power Sources*, vol. 267, pp. 760–769, 2014, doi: 10.1016/j.jpowsour.2014.05.139.

[100] N. Yang, X. Zhang, B. Shang, and G. Li, 'Unbalanced discharging and aging due to temperature differences among the cells in a lithium-ion battery pack with parallel combination', *Journal of Power Sources*, vol. 306, pp. 733–741, Feb. 2016, doi: 10.1016/j.jpowsour.2015.12.079.

[101] M. Lewerenz, A. Marongiu, A. Warnecke, and D. U. Sauer, 'Differential voltage analysis as a tool for analyzing inhomogeneous aging: A case study for LiFePO4|Graphite cylindrical cells', *Journal of Power Sources*, vol. 368, pp. 57–67, 2017, doi: 10.1016/j.jpowsour.2017.09.059.

[102] Y. Cai, M. Cancian, M. D'Arpino, and G. Rizzoni, 'A generalized equivalent circuit model for large-scale battery packs with cell-to-cell

variation', in *2019 IEEE National Aerospace and Electronics Conference (NAECON)*, Dayton, OH, USA, Jul. 2019, pp. 24–30. doi: 10.1109/NAECON46414.2019.9057803.

[103] R. Gogoana, M. B. Pinson, M. Z. Bazant, and S. E. Sarma, 'Internal resistance matching for parallel-connected lithium-ion cells and impacts on battery pack cycle life', *Journal of Power Sources*, vol. 252, pp. 8–13, Apr. 2014, doi: 10.1016/j.jpowsour.2013.11.101.

[104] X. Liu, W. Ai, M. Naylor Marlow, Y. Patel, and B. Wu, 'The effect of cell-to-cell variations and thermal gradients on the performance and degradation of lithium-ion battery packs', *Applied Energy*, vol. 248, no. April, pp. 489–499, 2019, doi: 10.1016/j.apenergy.2019.04.108.

[105] X. Gong, R. Xiong, and C. C. Mi, 'Study of the Characteristics of Battery Packs in Electric Vehicles With Parallel-Connected Lithium-Ion Battery Cells', *IEEE Trans. on Ind. Applicat.*, vol. 51, no. 2, pp. 1872–1879, Mar. 2015, doi: 10.1109/TIA.2014.2345951.

[106] M. Baumann, L. Wildfeuer, S. Rohr, and M. Lienkamp, 'Parameter variations within Li-Ion battery packs – Theoretical investigations and experimental quantification', *Journal of Energy Storage*, vol. 18, pp. 295–307, Aug. 2018, doi: 10.1016/j.est.2018.04.031.

[107] R. Carter *et al.*, 'Directionality of thermal gradients in lithium-ion batteries dictates diverging degradation modes', *Cell Reports Physical Science*, p. 100351, Feb. 2021, doi: 10.1016/j.xcrp.2021.100351.

[108] M. Ecker *et al.*, 'Development of a lifetime prediction model for lithium-ion batteries based on extended accelerated aging test data', *Journal of Power Sources*, vol. 215, pp. 248–257, 2012, doi: 10.1016/j.jpowsour.2012.05.012.

[109] S. Käbitz *et al.*, 'Cycle and calendar life study of a graphite|LiNi1/3Mn1/3Co1/3O2 Li-ion high energy system. Part A: Full cell characterization', *Journal of Power Sources*, vol. 239, pp. 572–583, 2013, doi: 10.1016/j.jpowsour.2013.03.045.

[110] J. Schmalstieg, S. Käbitz, M. Ecker, and D. U. Sauer, 'A holistic aging model for Li(NiMnCo)O2 based 18650 lithium-ion batteries',

Journal of Power Sources, vol. 257, pp. 325–334, Jul. 2014, doi: 10.1016/j.jpowsour.2014.02.012.

[111] M. Ecker *et al.*, 'Calendar and cycle life study of Li(NiMnCo)O2-based 18650 lithium-ion batteries', *Journal of Power Sources*, vol. 248, pp. 839–851, 2014, doi: 10.1016/j.jpowsour.2013.09.143.

[112] I. Baghdadi, O. Briat, J.-Y. Delétage, P. Gyan, and J.-M. Vinassa, 'Lithium battery aging model based on Dakin´s degradation approach', *Journal of Power Sources*, vol. 325, pp. 273–285, 2016, doi: 10.1016/j.jpowsour.2016.06.036.

[113] P. Keil, 'Aging of Lithium-Ion Batteries in Electric Vehicles', Technische Universität München, München, 2017.

[114] E. Redondo-Iglesias, P. Venet, and S. Pelissier, 'Modelling Lithium-Ion Battery Ageing in Electric Vehicle Applications — Calendar and Cycling Ageing Combination Effects', *Batteries*, vol. 6, no. 14, 2020, doi: 10.3390/batteries6010014.

[115] S. L. Hahn, M. Storch, R. Swaminathan, B. Obry, J. Bandlow, and K. P. Birke, 'Quantitative validation of calendar aging models for lithium-ion batteries', *Journal of Power Sources*, vol. 400, pp. 402–414, 2018, doi: 10.1016/j.jpowsour.2018.08.019.

[116] M. Dubarry, N. Qin, and P. Brooker, 'Calendar aging of commercial Li-ion cells of different chemistries – A review', *Current Opinion in Electrochemistry*, vol. 9, pp. 106–113, 2018, doi: 10.1016/j.coelec.2018.05.023.

[117] D. Aurbach, B. Markovsky, A. Rodkin, M. Cojocaru, E. Levi, and H. J. Kim, 'An analysis of rechargeable lithium-ion batteries after prolonged cycling', *Electrochimica Acta*, vol. 47, no. 12, pp. 1899–1911, 2002, doi: 10.1016/S0013-4686(02)00013-0.

[118] T. Waldmann, M. Wilka, M. Kasper, M. Fleischhammer, and M. Wohlfahrt-Mehrens, 'Temperature dependent ageing mechanisms in Lithium-ion batteries – A Post-Mortem study', *Journal of Power Sources*, vol. 262, pp. 129–135, Sep. 2014, doi: 10.1016/j.jpowsour.2014.03.112.

[119] R. B. Wright *et al.*, 'Calendar- and cycle-life studies of advanced technology development program generation 1 lithium-ion batteries', *Journal of Power Sources*, vol. 110, no. 2, pp. 445–470, 2002, doi: 10.1016/S0378-7753(02)00210-0.

[120] P. Ramadass, B. Haran, R. White, and B. N. Popov, 'Capacity fade of Sony 18650 cells cycled at elevated temperatures: Part II. Capacity

fade analysis', *Journal of Power Sources*, vol. 112, no. 2, pp. 614–620, 2002, doi: 10.1016/S0378-7753(02)00473-1.

[121] K. Kleiner, P. Jakes, S. Scharner, V. Liebau, and H. Ehrenberg, 'Changes of the balancing between anode and cathode due to fatigue in commercial lithium-ion cells', *Journal of Power Sources*, vol. 317, pp. 25–34, 2016, doi: 10.1016/j.jpowsour.2016.03.049.

[122] M. Schimpe, M. E. von Kuepach, M. Naumann, H. C. Hesse, K. Smith, and A. Jossen, 'Comprehensive Modeling of Temperature-Dependent Degradation Mechanisms in Lithium Iron Phosphate Batteries', *Journal of The Electrochemical Society*, vol. 165, no. 2, pp. A181–A193, 2018, doi: 10.1149/2.1181714jes.

[123] K. Jalkanen, J. Karppinen, L. Skogström, T. Laurila, M. Nisula, and K. Vuorilehto, 'Cycle aging of commercial NMC/graphite pouch cells at different temperatures', *Applied Energy*, vol. 154, pp. 160–172, Sep. 2015, doi: 10.1016/j.apenergy.2015.04.110.

[124] Y. Preger *et al.*, 'Degradation of Commercial Lithium-Ion Cells as a Function of Chemistry and Cycling Conditions', *J. Electrochem. Soc.*, vol. 167, no. 12, p. 120532, Sep. 2020, doi: 10.1149/1945-7111/abae37.

[125] I. Bloom *et al.*, 'Effect of cathode composition on capacity fade, impedance rise and power fade in high-power, lithium-ion cells', *Journal of Power Sources*, vol. 124, no. 2, pp. 538–550, Nov. 2003, doi: 10.1016/S0378-7753(03)00806-1.

[126] F. Leng, C. Ming Tan, and M. Pecht, 'Effect of Temperature on the Aging rate of Li Ion Battery Operating above Room Temperature', *Scientific Reports*, vol. 5, no. 12967, 2015, doi: 10.1038/srep12967.

[127] M. Ecker, P. S. Sabet, and D. U. Sauer, 'Influence of operational condition on lithium plating for commercial lithium-ion batteries - Electrochemical experiments and post-mortem-analysis', *Applied Energy*, vol. 206, pp. 934–946, 2017, doi: 10.1016/j.apenergy.2017.08.034.

[128] T. Waldmann *et al.*, 'Interplay of Operational Parameters on Lithium Deposition in Lithium-Ion Cells: Systematic Measurements with Reconstructed 3-Electrode Pouch Full Cells', *J. Electrochem. Soc.*, vol. 163, no. 7, pp. A1232–A1238, 2016, doi: 10.1149/2.0591607jes.

[129] A. Friesen, X. Mönnighoff, M. Börner, J. Haetge, F. M. Schappacher, and M. Winter, 'Influence of temperature on the aging behavior of 18650-type lithium ion cells: A comprehensive approach combining electrochemical characterization and post-mortem analysis', *Journal*

of Power Sources, vol. 342, pp. 88–97, 2017, doi: 10.1016/j.jpowsour.2016.12.040.

[130] S. F. Schuster *et al.*, 'Nonlinear aging characteristics of lithium-ion cells under different operational conditions', *Journal of Energy Storage*, vol. 1, no. 1, pp. 44–53, 2015, doi: 10.1016/j.est.2015.05.003.

[131] W. Liu, C. Delacourt, C. Forgez, and S. Pelissier, 'Study of graphite/NCA Li-ion cell degradation during accelerated aging tests — Data analysis of the SIMSTOCK project', in *2011 IEEE Vehicle Power and Propulsion Conference*, Sep. 2011, pp. 1–6. doi: 10.1109/VPPC.2011.6043110.

[132] M. S. D. Darma *et al.*, 'The influence of cycling temperature and cycling rate on the phase specific degradation of a positive electrode in lithium ion batteries: A post mortem analysis', *Journal of Power Sources*, vol. 327, pp. 714–725, 2016, doi: 10.1016/j.jpowsour.2016.07.115.

[133] S. Watanabe, M. Kinoshita, T. Hosokawa, K. Morigaki, and K. Nakura, 'Capacity fade of LiAlyNi1-x-yCoxO 2 cathode for lithium-ion batteries during accelerated calendar and cycle life tests (surface analysis of LiAlyNi1-x-yCo xO2 cathode after cycle tests in restricted depth of discharge ranges)', *Journal of Power Sources*, vol. 258, pp. 210–217, 2014, doi: 10.1016/j.jpowsour.2014.02.018.

[134] M. Lewerenz and D. U. Sauer, 'Evaluation of cyclic aging tests of prismatic automotive LiNiMnCoO2-Graphite cells considering influence of homogeneity and anode overhang', *Journal of Energy Storage*, vol. 18, no. May, pp. 421–434, 2018, doi: 10.1016/j.est.2018.06.003.

[135] G. Ning, B. Haran, and B. N. Popov, 'Capacity fade study of lithium-ion batteries cycled at high discharge rates', *Journal of Power Sources*, vol. 117, no. 1–2, pp. 160–169, May 2003, doi: 10.1016/S0378-7753(03)00029-6.

[136] A. S. Mussa, 'Fast-charging to a partial state of charge in lithium-ion batteries: A comparative ageing study', *Journal of Energy Storage*, vol. 13, 2017.

[137] Y. Ruan, X. Song, Y. Fu, C. Song, and V. Battaglia, 'Structural evolution and capacity degradation mechanism of LiNi0.6Mn0.2Co0.2O2 cathode materials', *Journal of Power*

Sources, vol. 400, pp. 539–548, Oct. 2018, doi: 10.1016/j.jpowsour.2018.08.056.

[138] L. Su *et al.*, 'Identifying main factors of capacity fading in lithium ion cells using orthogonal design of experiments', *Applied Energy*, vol. 163, pp. 201–210, 2016, doi: 10.1016/j.apenergy.2015.11.014.

[139] J. de Hoog *et al.*, 'Combined cycling and calendar capacity fade modeling of a Nickel-Manganese-Cobalt Oxide Cell with real-life profile validation', *Applied Energy*, vol. 200, pp. 47–61, 2017, doi: 10.1016/j.apenergy.2017.05.018.

[140] M. Lewerenz, J. Münnix, J. Schmalstieg, S. Käbitz, M. Knips, and D. U. Sauer, 'Systematic aging of commercial LiFePO4|Graphite cylindrical cells including a theory explaining rise of capacity during aging', *Journal of Power Sources*, vol. 345, pp. 254–263, 2017, doi: 10.1016/j.jpowsour.2017.01.133.

[141] I. A. Hunt, Y. Zhao, Y. Patel, and J. Offer, 'Surface Cooling Causes Accelerated Degradation Compared to Tab Cooling for Lithium-Ion Pouch Cells', *J. Electrochem. Soc.*, vol. 163, no. 9, pp. A1846–A1852, 2016, doi: 10.1149/2.0361609jes.

[142] R. Carter and C. T. Love, 'Modulation of Lithium Plating in Li-Ion Batteries with External Thermal Gradient', *ACS Applied Materials and Interfaces*, vol. 10, p. 26328−26334, 2018.

[143] R. W. Atkinson, R. Carter, and C. T. Love, 'Operational strategy to stabilize lithium metal anodes by applied thermal gradient', *Energy Storage Materials*, vol. 22, pp. 18–28, 2019.

[144] K. L. Gering *et al.*, 'Investigation of path dependence in commercial lithium-ion cells chosen for plug-in hybrid vehicle duty cycle protocols', *Journal of Power Sources*, vol. 196, no. 7, pp. 3395–3403, 2011, doi: 10.1016/j.jpowsour.2010.05.058.

[145] R. Carter, E. J. Klein, T. A. Kingston, and C. T. Love, 'Detection of Lithium Plating During Thermally Transient Charging of Li-Ion Batteries', *Front. Energy Res.*, vol. 7, p. 144, Dec. 2019, doi: 10.3389/fenrg.2019.00144.

[146] W. Chang, C. Bommier, T. Fair, J. Yeung, S. Patil, and D. Steingart, 'Understanding Adverse Effects of Temperature Shifts on Li-Ion Batteries: An Operando Acoustic Study', *J. Electrochem. Soc.*, vol. 167, no. 9, p. 090503, 2020, doi: 10.1149/1945-7111/ab6c56.

[147] C. Pastor-Fernández, T. F. Yu, W. D. Widanage, and J. Marco, 'Critical review of non-invasive diagnosis techniques for quantification of degradation modes in lithium-ion batteries',

Renewable and Sustainable Energy Reviews, vol. 109, no. March, pp. 138–159, 2019, doi: 10.1016/j.rser.2019.03.060.

[148] M. Dubarry, C. Truchot, and B. Y. Liaw, 'Synthesize battery degradation modes via a diagnostic and prognostic model', *Journal of Power Sources*, vol. 219, pp. 204–216, Dec. 2012, doi: 10.1016/j.jpowsour.2012.07.016.

[149] M. Dubarry *et al.*, 'Evaluation of commercial lithium-ion cells based on composite positive electrode for plug-in hybrid electric vehicle applications. Part II. Degradation mechanism under 2C cycle aging', *Journal of Power Sources*, vol. 196, no. 23, pp. 10336–10343, Dec. 2011, doi: 10.1016/j.jpowsour.2011.08.078.

[150] M. Dubarry, V. Svoboda, R. Hwu, and B. Yann Liaw, 'Incremental Capacity Analysis and Close-to-Equilibrium OCV Measurements to Quantify Capacity Fade in Commercial Rechargeable Lithium Batteries', *Electrochem. Solid-State Lett.*, vol. 9, no. 10, p. A454, 2006, doi: 10.1149/1.2221767.

[151] M. Dubarry and B. Y. Liaw, 'Identify capacity fading mechanism in a commercial LiFePO4 cell', *Journal of Power Sources*, vol. 194, no. 1, pp. 541–549, Oct. 2009, doi: 10.1016/j.jpowsour.2009.05.036.

[152] M. Dubarry *et al.*, 'Identifying battery aging mechanisms in large format Li ion cells', *Journal of Power Sources*, vol. 196, no. 7, pp. 3420–3425, Apr. 2011, doi: 10.1016/j.jpowsour.2010.07.029.

[153] I. Bloom, J. Christophersen, and K. Gering, 'Differential voltage analyses of high-power lithium-ion cells 2. Application', *Journal of Power Sources*, vol. 139, no. 1–2, pp. 304–313, Jan. 2005, doi: 10.1016/j.jpowsour.2004.07.022.

[154] I. Bloom, J. P. Christophersen, D. P. Abraham, and K. L. Gering, 'Differential voltage analyses of high-power lithium-ion cells 3. Another anode phenomenon', *Journal of Power Sources*, vol. 157, no. 1, pp. 537–542, Jun. 2006, doi: 10.1016/j.jpowsour.2005.07.054.

[155] I. Bloom, L. K. Walker, J. K. Basco, D. P. Abraham, J. P. Christophersen, and C. D. Ho, 'Differential voltage analyses of high-power lithium-ion cells 4. Cells containing NMC', *Journal of Power Sources*, vol. 195, no. 3, pp. 877–882, Feb. 2010, doi: 10.1016/j.jpowsour.2009.08.019.

[156] Y. Wu, 'Non-Invasive Aging Detection Methods of Lithium-Ion Batteries', p. 138.

[157] J. Wang *et al.*, 'Degradation of lithium ion batteries employing graphite negatives and nickel–cobalt–manganese oxide + spinel manganese oxide positives: Part 1, aging mechanisms and life

estimation', *Journal of Power Sources*, vol. 269, pp. 937–948, Dec. 2014, doi: 10.1016/j.jpowsour.2014.07.030.

[158] E. Sarasketa-Zabala, F. Aguesse, I. Villarreal, L. M. Rodriguez-Martinez, C. M. López, and P. Kubiak, 'Understanding lithium inventory loss and sudden performance fade in cylindrical cells during cycling with deep-discharge steps', *Journal of Physical Chemistry C*, vol. 119, no. 2, pp. 896–906, 2015, doi: 10.1021/jp510071d.

[159] M. E. Goldammer, 'Investigation of degradation mechanisms in lithium-ion batteries by incremental open-circuit-voltage characterization and impedance spectra', *IEEE Vehicle and Propulsion Conference*, 2020.

[160] S. Lee, J. B. Siegel, A. G. Stefanopoulou, J.-W. Lee, and T.-K. Lee, 'Electrode State of Health Estimation for Lithium Ion Batteries Considering Half-cell Potential Change Due to Aging', *Journal of The Electrochemical Society*, vol. 167, no. 9, p. 090531, 2020, doi: 10.1149/1945-7111/ab8c83.

[161] I. D. Campbell, M. Marzook, M. Marinescu, and G. J. Offer, 'How Observable Is Lithium Plating? Differential Voltage Analysis to Identify and Quantify Lithium Plating Following Fast Charging of Cold Lithium-Ion Batteries', *J. Electrochem. Soc.*, vol. 166, no. 4, pp. A725–A739, 2019, doi: 10.1149/2.0821904jes.

[162] J. E. Harlow *et al.*, 'A Wide Range of Testing Results on an Excellent Lithium-Ion Cell Chemistry to be used as Benchmarks for New Battery Technologies', *J. Electrochem. Soc.*, vol. 166, no. 13, pp. A3031–A3044, 2019, doi: 10.1149/2.0981913jes.

[163] P. Keil and A. Jossen, 'Calendar Aging of NCA Lithium-Ion Batteries Investigated by Differential Voltage Analysis and Coulomb Tracking', *Journal of the Electrochemical Society*, vol. 164, no. 1, pp. A6066–A6074, 2017, doi: 10.1149/2.0091701jes.

[164] I. Zilberman, S. Ludwig, M. Schiller, and A. Jossen, 'Online aging determination in lithium-ion battery module with forced temperature gradient', *Journal of Energy Storage*, vol. 28, no. 101170, 2020, doi: 10.1016/j.est.2019.101170.

[165] M. Lewerenz, G. Fuchs, L. Becker, and D. U. Sauer, 'Irreversible calendar aging and quantification of the reversible capacity loss caused by anode overhang', *Journal of Energy Storage*, vol. 18, pp. 149–159, 2018, doi: 10.1016/j.est.2018.04.029.

[166] J. P. Fath *et al.*, 'Quantification of aging mechanisms and inhomogeneity in cycled lithium-ion cells by differential voltage

analysis', *Journal of Energy Storage*, vol. 25, p. 100813, Oct. 2019, doi: 10.1016/j.est.2019.100813.

[167] T. C. Bach *et al.*, 'Nonlinear aging of cylindrical lithium-ion cells linked to heterogeneous compression', *Journal of Energy Storage*, vol. 5, pp. 212–223, 2016, doi: 10.1016/j.est.2016.01.003.

[168] C. R. Birkl, M. R. Roberts, E. McTurk, P. G. Bruce, and D. A. Howey, 'Degradation diagnostics for lithium ion cells', *Journal of Power Sources*, vol. 341, pp. 373–386, Feb. 2017, doi: 10.1016/j.jpowsour.2016.12.011.

[169] A. Barré, B. Deguilhem, S. Grolleau, M. Gérard, F. Suard, and D. Riu, 'A review on lithium-ion battery ageing mechanisms and estimations for automotive applications', *Journal of Power Sources*, vol. 241, pp. 680–689, 2013, doi: 10.1016/j.jpowsour.2013.05.040 Review.

[170] X. Han *et al.*, 'A review on the key issues of the lithium ion battery degradation among the whole life cycle', *eTransportation*, vol. 1, p. 100005, Aug. 2019, doi: 10.1016/j.etran.2019.100005.

[171] J. Vetter *et al.*, 'Ageing mechanisms in lithium-ion batteries', *Journal of Power Sources*, vol. 147, no. 1–2, pp. 269–281, 2005, doi: 10.1016/j.jpowsour.2005.01.006.

[172] T. Waldmann *et al.*, 'Review—Post-Mortem Analysis of Aged Lithium-Ion Batteries: Disassembly Methodology and Physico-Chemical Analysis Techniques', *Journal of The Electrochemical Society*, vol. 163, no. 10, pp. A2149–A2164, 2016, doi: 10.1149/2.1211609jes.

[173] C. Schlasza, P. Ostertag, D. Chrenko, R. Kriesten, and D. Bouquain, 'Review on the aging mechanisms in Li-ion batteries for electric vehicles based on the FMEA method', *2014 IEEE Transportation Electrification Conference and Expo (ITEC)*, 2014, doi: 10.1109/ITEC.2014.6861811.

[174] J. S. Edge *et al.*, 'Lithium ion battery degradation: what you need to know', *Phys. Chem. Chem. Phys.*, vol. 23, no. 14, pp. 8200–8221, 2021, doi: 10.1039/D1CP00359C.

[175] V. Agubra and J. Fergus, 'Lithium ion battery anode aging mechanisms', *Materials*, vol. 6, no. 4, pp. 1310–1325, 2013, doi: 10.3390/ma6041310.

[176] P. N. Ross, 'Catalysis and interfacial chemistry in lithium batteries: A surface science approach', *Catalysis Letters*, vol. 144, no. 8, pp. 1370–1376, 2014, doi: 10.1007/s10562-014-1287-4.

[177] Z. Ahmad, V. Venturi, H. Hafiz, and V. Viswanathan, ‘Interfaces in Solid Electrolyte Interphase- Implications for Lithium-Ion Batteries’, *The Journal of Physical Chemistry*, 2021, doi: 10.1021/acs.jpcc.1c00867.

[178] V. Winkler, ‘Oberflächenanalytische Charakterisierung der SEI auf Graphit-Anodenschichten in Lithium-Ionen-Batterien’, Albert-Ludwigs-Universität Freiburg, Freiburg, 2016. [Online]. Available: https://www.freidok.uni-freiburg.de/data/10734

[179] P. Verma, P. Maire, and P. Novák, ‘A review of the features and analyses of the solid electrolyte interphase in Li-ion batteries’, *Electrochimica Acta*, vol. 55, no. 22, pp. 6332–6341, 2010, doi: 10.1016/j.electacta.2010.05.072.

[180] E. Peled, ‘The Electrochemical-Behavior of Alkali and Alkaline-Earth Metals in Non-Aqueous Battery Systems - the Solid Electrolyte Interphase Model’, *Journal of the Electrochemical Society*, vol. 126, no. 12, pp. 2047–2051, 1979, doi: 10.1149/1.2128859.

[181] E. Y. Jung *et al.*, ‘Experimental study on solid electrolyte interphase of graphite electrode in Li-ion battery by surface analysis technique’, *Molecular Crystals and Liquid Crystals*, vol. 663, no. 1, pp. 158–167, 2018, doi: 10.1080/15421406.2018.1470709.

[182] M. Broussely *et al.*, ‘Main aging mechanisms in Li ion batteries’, *Journal of Power Sources*, vol. 146, no. 1–2, pp. 90–96, 2005, doi: 10.1016/j.jpowsour.2005.03.172.

[183] E. Peled and H. Yamin, ‘The Passivating Layer on Lithium in Lithium Tetrachloroalumnate Thionyl Chloride Solutions’, in *Proceedings of the 28th Power Sources Symposium*, Atlantic City, 1978, pp. 237–241.

[184] M. Klett *et al.*, ‘Uneven film formation across depth of porous graphite electrodes in cycled commercial li-ion batteries’, *Journal of Physical Chemistry C*, vol. 119, no. 1, pp. 90–100, 2015, doi: 10.1021/jp509665e.

[185] F. German *et al.*, ‘Influence of temperature and upper cut-off voltage on the formation of lithium-ion cells’, *Journal of Power Sources*, vol. 264, pp. 100–107, 2014, doi: 10.1016/j.jpowsour.2014.04.071.

[186] I. V. Veryovkin, C. E. Tripa, A. V. Zinovev, S. V. Baryshev, Y. Li, and D. P. Abraham, ‘TOF SIMS characterization of SEI layer on battery electrodes’, *Nuclear Instruments and Methods in Physics*

Research, Section B: Beam Interactions with Materials and Atoms, vol. 332, pp. 368–372, 2014, doi: 10.1016/j.nimb.2014.02.098.

[187] D. Aurbach, M. D. Levi, E. Levi, and A. Schechter, 'Failure and Stabilization Mechanisms of Graphite Electrodes', *J. Phys. Chem. B*, vol. 101, no. 12, pp. 2195–2206, Mar. 1997, doi: 10.1021/jp962815t.

[188] E. Peled, D. Golodnitsky, C. Menachem, and D. Bar-Tow, 'An Advanced Tool for the Selection of Electrolyte Components for Rechargeable Lithium Batteries', *J. Electrochem. Soc.*, vol. 145, no. 10, pp. 3482–3486, Oct. 1998, doi: 10.1149/1.1838831.

[189] A. V. Churikov, 'Transfer mechanism in solid-electrolyte layers on lithium: influence of temperature and polarization', *Electrochimica Acta*, vol. 46, no. 15, pp. 2415–2426, Apr. 2001, doi: 10.1016/S0013-4686(01)00439-X.

[190] S. S. Zhang, K. Xu, and T. R. Jow, 'Electrochemical impedance study on the low temperature of Li-ion batteries', *Electrochimica Acta*, vol. 49, no. 7, pp. 1057–1061, Mar. 2004, doi: 10.1016/j.electacta.2003.10.016.

[191] H. H. Lee, C. C. Wan, and Y. Y. Wang, 'Thermal Stability of the Solid Electrolyte Interface on Carbon Electrodes of Lithium Batteries', *J. Electrochem. Soc.*, vol. 151, no. 4, p. A542, 2004, doi: 10.1149/1.1647568.

[192] J. T. Li *et al.*, 'XPS and ToF-SIMS study of Sn-Co alloy thin films as anode for lithium ion battery', *Journal of Power Sources*, vol. 195, no. 24, pp. 8251–8257, 2010, doi: 10.1016/j.jpowsour.2010.07.043.

[193] M. N. Richard and J. R. Dahn, 'Accelerating Rate Calorimetry Study on the Thermal Stability of Lithium Intercalated Graphite in Electrolyte', *Journal of The Electrochemical Society*, p. 11, 1999.

[194] D. P. Abraham, J. L. Knuth, D. W. Dees, I. Bloom, and J. P. Christophersen, 'Performance degradation of high-power lithium-ion cells-Electrochemistry of harvested electrodes', *Journal of Power Sources*, vol. 170, no. 2, pp. 465–475, 2007, doi: 10.1016/j.jpowsour.2007.03.071.

[195] Z. Zhuo *et al.*, 'Breathing and oscillating growth of solid-electrolyte-interphase upon electrochemical cycling', *Chemical Communications*, vol. 54, no. 7, pp. 814–817, 2018, doi: 10.1039/c7cc07082a.

[196] I. Laresgoiti, S. Käbitz, M. Ecker, and D. U. Sauer, 'Modeling mechanical degradation in lithium ion batteries during cycling: Solid

electrolyte interphase fracture', *Journal of Power Sources*, vol. 300, pp. 112–122, 2015, doi: 10.1016/j.jpowsour.2015.09.033.

[197] H. Jannesari, M. D. Emami, and C. Ziegler, 'Effect of electrolyte transport properties and variations in the morphological parameters on the variation of side reaction rate across the anode electrode and the aging of lithium ion batteries', *Journal of Power Sources*, vol. 196, no. 22, pp. 9654–9664, Nov. 2011, doi: 10.1016/j.jpowsour.2011.07.026.

[198] N. Ghanbari, T. Waldmann, M. Kasper, P. Axmann, and M. Wohlfahrt-Mehrens, 'Inhomogeneous Degradation of Graphite Anodes in Li-Ion Cells A Postmortem Study Using Glow Discharge Optical Emission Spectroscopy (GD-OES)', *The Journal of Physical Chemistry*, vol. 120, 2016, doi: 10.1021/acs.jpcc.6b07117.

[199] M. Petzl and M. A. Danzer, 'Nondestructive detection, characterization, and quantification of lithium plating in commercial lithium-ion batteries', *Journal of Power Sources*, vol. 254, pp. 80–87, May 2014, doi: 10.1016/j.jpowsour.2013.12.060.

[200] Z. Li, J. Huang, B. Yann Liaw, V. Metzler, and J. Zhang, 'A review of lithium deposition in lithium-ion and lithium metal secondary batteries', *Journal of Power Sources*, vol. 254, pp. 168–182, May 2014, doi: 10.1016/j.jpowsour.2013.12.099.

[201] C. Fear, M. Parmananda, V. Kabra, R. Carter, C. T. Love, and P. P. Mukherjee, 'Mechanistic Underpinnings of Thermal Gradient Induced Inhomogeneity in Lithium Plating', *Energy Storage Materials*, vol. 35, pp. 500–511, 2021, doi: 10.1016/j.ensm.2020.11.029.

[202] X.-G. Yang, S. Ge, T. Liu, Y. Leng, and C.-Y. Wang, 'A look into the voltage plateau signal for detection and quantification of lithium plating in lithium-ion cells', *Journal of Power Sources*, vol. 395, pp. 251–261, Aug. 2018, doi: 10.1016/j.jpowsour.2018.05.073.

[203] K. Takahashi and V. Srinivasan, 'Examination of Graphite Particle Cracking as a Failure Mode in Lithium-Ion Batteries: A Model-Experimental Study', *J. Electrochem. Soc.*, vol. 162, no. 4, pp. A635–A645, 2015, doi: 10.1149/2.0281504jes.

[204] J. Purewal, J. Wang, J. Graetz, S. Soukiazian, H. Tataria, and M. W. Verbrugge, 'Degradation of lithium ion batteries employing graphite negatives and nickel–cobalt–manganese oxide + spinel manganese oxide positives: Part 2, chemical–mechanical degradation model',

Journal of Power Sources, vol. 272, pp. 1154–1161, Dec. 2014, doi: 10.1016/j.jpowsour.2014.07.028.

[205] S. Mohan, Y. Kim, J. B. Siegel, N. A. Samad, and A. G. Stefanopoulou, 'A Phenomenological Model of Bulk Force in a Li-Ion Battery Pack and Its Application to State of Charge Estimation', *J. Electrochem. Soc.*, vol. 161, no. 14, pp. A2222–A2231, 2014, doi: 10.1149/2.0841414jes.

[206] M. Lang *et al.*, 'Post mortem analysis of fatigue mechanisms in LiNi0.8Co0.15Al0.05O2– LiNi0.5Co0.2Mn0.3O2–LiMn2O4/graphite lithium ion batteries', *Journal of Power Sources*, vol. 326, pp. 397–409, 2016, doi: 10.1016/j.jpowsour.2016.07.010.

[207] J. O. Besenhard, M. Winter, J. Yang, and W. Biberacher, 'Filming mechanism of lithium-carbon anodes in organic and inorganic electrolytes', *Journal of Power Sources*, vol. 54, no. 2, pp. 228–231, Apr. 1995, doi: 10.1016/0378-7753(94)02073-C.

[208] D. Aurbach, 'Electrode–solution interactions in Li-ion batteries: a short summary and new insights', *Journal of Power Sources*, vol. 119–121, pp. 497–503, Jun. 2003, doi: 10.1016/S0378-7753(03)00273-8.

[209] D. Goers, M. E. Spahr, A. Leone, W. Märkle, and P. Novák, 'The influence of the local current density on the electrochemical exfoliation of graphite in lithium-ion battery negative electrodes', *Electrochimica Acta*, vol. 56, no. 11, pp. 3799–3808, Apr. 2011, doi: 10.1016/j.electacta.2011.02.046.

[210] S. Gorse, B. Kugler, T. Samtleben, T. Waldmann, G. Schneider, and V. Knoblauch, 'An Explanation of the Ageing Mechanism of Li-Ion Batteries by Metallographic and Material Analysis', vol. 51, 2014, doi: 10.3139/147.110325.

[211] W. Ai, L. Kraft, J. Sturm, A. Jossen, and B. Wu, 'Electrochemical Thermal-Mechanical Modelling of Stress Inhomogeneity in Lithium-Ion Pouch Cells', *J. Electrochem. Soc.*, vol. 167, no. 1, p. 013512, 2020, doi: 10.1149/2.0122001JES.

[212] J. Cannarella and C. B. Arnold, 'Stress evolution and capacity fade in constrained lithium-ion pouch cells', *Journal of Power Sources*, vol. 245, pp. 745–751, Jan. 2014, doi: 10.1016/j.jpowsour.2013.06.165.

[213] M. J. Mühlbauer *et al.*, 'Inhomogeneous distribution of lithium and electrolyte in aged Li-ion cylindrical cells', *California Digital Library*, 2020, doi: 10.1016/j.jpowsour.2020.228690.

[214] S. Fang, D. Jackson, M. L. Dreibelbis, T. F. Kuech, and R. J. Hamers, 'Anode-originated SEI migration contributes to formation of cathode-

electrolyte interphase layer', *Journal of Power Sources*, vol. 373, pp. 184–192, Jan. 2018, doi: 10.1016/j.jpowsour.2017.09.050.

[215] M. Wohlfahrt-Mehrens, C. Vogler, and J. Garche, 'Aging mechanisms of lithium cathode materials', *Journal of Power Sources*, vol. 127, no. 1–2, pp. 58–64, Mar. 2004, doi: 10.1016/j.jpowsour.2003.09.034.

[216] M. Kerlau, M. Marcinek, V. Srinivasan, and R. M. Kostecki, 'Studies of local degradation phenomena in composite cathodes for lithium-ion batteries', *Electrochimica Acta*, vol. 52, no. 17, pp. 5422–5429, May 2007, doi: 10.1016/j.electacta.2007.02.085.

[217] H. Liu *et al.*, 'Three-dimensional investigation of cycling-induced microstructural changes in lithium-ion battery cathodes using focused ion beam/scanning electron microscopy', *Journal of Power Sources*, vol. 306, pp. 300–308, 2016, doi: 10.1016/j.jpowsour.2015.11.108.

[218] H. Wang and J. F. Whitacre, 'Inhomogeneous aging of cathode materials in commercial 18650 lithium ion battery cells', *Journal of Energy Storage*, vol. 35, p. 102244, Mar. 2021, doi: 10.1016/j.est.2021.102244.

[219] H. Kobayashi, M. Shikano, S. Koike, H. Sakaebe, and K. Tatsumi, 'Investigation of positive electrodes after cycle testing of high-power Li-ion battery cells. I. An approach to the power fading mechanism using XANES', *Journal of Power Sources*, vol. 174, no. 2, pp. 380–386, 2007, doi: 10.1016/j.jpowsour.2007.06.134.

[220] J. A. Gilbert, I. A. Shkrob, and D. P. Abraham, 'Transition Metal Dissolution, Ion Migration, Electrocatalytic Reduction and Capacity Loss in Lithium-Ion Full Cells', *J. Electrochem. Soc.*, vol. 164, no. 2, pp. A389–A399, 2017, doi: 10.1149/2.1111702jes.

[221] S. Nowak and M. Winter, 'Review—Chemical Analysis for a Better Understanding of Aging and Degradation Mechanisms of Non-Aqueous Electrolytes for Lithium Ion Batteries: Method Development, Application and Lessons Learned', *Journal of The Electrochemical Society*, vol. 162, no. 14, pp. A2500–A2508, 2015, doi: 10.1149/2.0121514jes.

[222] C. Peabody and C. B. Arnold, 'The role of mechanically induced separator creep in lithium-ion battery capacity fade', *Journal of*

Power Sources, vol. 196, pp. 8147–8153, 2011, doi: 10.1016/j.jpowsour.2011.05.023.

[223] A. Rodräguez, 'Synthetische Kunststoffe', in *DOMININGHAUS - Kunststoffe*, 7th ed., Springer Berlin Heidelberg, 2008.

[224] M. Zhao *et al.*, 'Electrochemical Stability of Copper in Lithium-Ion Battery Electrolytes', *Journal of Electrochemical Society*, vol. 147, no. 8, pp. 2874–2879, 2000.

[225] K. Rumpf, A. Rheinfeld, M. Schindler, J. Keil, T. Schua, and A. Jossen, 'Influence of Cell-to-Cell Variations on the Inhomogeneity of Lithium-Ion Battery Modules', *J. Electrochem. Soc.*, vol. 165, no. 11, pp. A2587–A2607, 2018, doi: 10.1149/2.0111811jes.

[226] D. Beck, P. Dechent, M. Junker, D. U. Sauer, and M. Dubarry, 'Inhomogeneities and Cell-to-Cell Variations in Lithium-Ion Batteries, a Review', *Energies*, vol. 14, no. 11, p. 3276, Jun. 2021, doi: 10.3390/en14113276.

[227] N. Williard, B. Sood, M. Osterman, and M. Pecht, 'Disassembly methodology for conducting failure analysis on lithium-ion batteries', *Journal of Materials Science: Materials in Electronics*, vol. 22, no. 3, pp. 1616–1630, 2011, doi: 10.1007/s10854-011-0452-4.

[228] M. Lewerenz, A. Warnecke, and D. U. Sauer, 'Post-mortem analysis on LiFePO4|Graphite cells describing the evolution & composition of covering layer on anode and their impact on cell performance', *Journal of Power Sources*, vol. 369, pp. 122–132, 2017, doi: 10.1016/j.jpowsour.2017.10.003.

[229] L. Somerville, J. Bareño, P. A. Jennings, A. McGordon, C. Lyness, and I. Bloom, 'The Effect of Pre-Analysis Washing on the Surface Film of Graphite Electrodes', *Electrochimica Acta*, vol. 206, pp. 70–76, 2016, doi: 10.1016/j.electacta.2016.04.133.

[230] A. U. Schmid, M. Kurka, and K. P. Birke, 'Reproducibility of Li-ion cell reassembling processes and their influence on coin cell aging', *Journal of Energy Storage*, vol. 24, no. April, 2019, doi: 10.1016/j.est.2019.04.006.

[231] J. Sieg *et al.*, 'Local degradation and differential voltage analysis of aged lithium-ion pouch cells', *Journal of Energy Storage*, vol. 30, no. February, p. 101582, 2020, doi: 10.1016/j.est.2020.101582.

[232] M. Ecker, T. K. D. Tran, P. Dechent, S. Käbitz, A. Warnecke, and D. U. Sauer, 'Parameterization of a Physico-Chemical Model of a Lithium-Ion Battery: I. Determination of Parameters', *Journal of the*

Electrochemical Society, vol. 162, no. 9, pp. A1836–A1848, 2015, doi: 10.1149/2.0551509jes.

[233] J. R. Dahn, 'Can one learn as much about lithium-ion battery failure using a micrometer as with a synchrotron?', presented at the Advanced Battery Power, Essen/online, Apr. 28, 2021.

[234] R. E. Dinnebier and S. J. L. Billinge, 'Principles of Powder Diffraction', in *Powder Diffraction*, R. E. Dinnebier and S. J. L. Billinge, Eds. Cambridge: Royal Society of Chemistry, 2008, pp. 1–19. doi: 10.1039/9781847558237-00001.

[235] L. Spieß, G. Teichert, R. Schwarzer, H. Behnken, and C. Genzel, *Moderne Röntgenbeugung*. 2019. doi: 10.1007/978-3-8348-8232-5.

[236] K. Maher and R. Yazami, 'A study of lithium ion batteries cycle aging by thermodynamics techniques', *Journal of Power Sources*, vol. 247, pp. 527–533, Feb. 2014, doi: 10.1016/j.jpowsour.2013.08.053.

[237] L. David *et al.*, 'High-Voltage Performance of Ni-Rich NCA Cathodes: Linking Operating Voltage with Cathode Degradation', *ChemElectroChem*, vol. 6, no. 22, pp. 5571–5580, Nov. 2019, doi: 10.1002/celc.201901338.

[238] M. Gey, *Instrumentelle Analytik und Bioanalytik*. Berlin, Heidelberg: Springer Berlin Heidelberg, 2008. doi: 10.1007/978-3-540-73804-6.

[239] P. C. Uden, Ed., *Element-Specific Chromatographic Detection by Atomic Emission Spectroscopy*, vol. 479. Washington, DC: American Chemical Society, 1992. doi: 10.1021/bk-1992-0479.

[240] T. Waldmann, N. Ghanbari, M. Kasper, and M. Wohlfahrt-Mehrens, 'Correlations between Electrochemical Data and Results from Post-Mortem Analysis of Aged Lithium-Ion Batteries', *Journal of The Electrochemical Society*, vol. 162, no. 8, pp. A1500–A1505, 2015, doi: 10.1149/2.0411508jes.

[241] Y. Kobayashi, T. Kobayashi, K. Shono, Y. Ohno, Y. Mita, and H. Miyashiro, 'Decrease in Capacity in Mn-Based/Graphite Commercial Lithium-Ion Batteries', *Journal of The Electrochemical Society*, vol. 160, no. 8, pp. A1181–A1186, 2013, doi: 10.1149/2.071308jes.

[242] J. I. Goldstein, D. E. Newbury, J. R. Michael, N. W. M. Ritchie, J. H. J. Scott, and D. C. Joy, *Scanning Electron Microscopy and X-Ray Microanalysis*. New York, NY: Springer New York, 2018. doi: 10.1007/978-1-4939-6676-9.

[243] M. Lu, H. Cheng, and Y. Yang, 'A comparison of solid electrolyte interphase (SEI) on the artificial graphite anode of the aged and

cycled commercial lithium ion cells', *Electrochimica Acta*, vol. 53, no. 9, pp. 3539–3546, 2008, doi: 10.1016/j.electacta.2007.09.062.

[244] W. Liu *et al.*, 'Electrochemical and X-ray photospectroscopy studies of polytetrafluoroethylene and polyvinylidene fluoride in Li/C batteries', *Journal of Power Sources*, vol. 68, no. 2, pp. 344–347, 1997, doi: 10.1016/S0378-7753(97)02637-2.

[245] J. C. Vickerman and I. S. Gilmore, *Surface Analysis - The Principal Techniques*. Wiley, 2009. doi: 10.1002/9780470721582.

[246] K. N. Wood and G. Teeter, 'XPS on Li-Battery-Related Compounds: Analysis of Inorganic SEI Phases and a Methodology for Charge Correction', *ACS Applied Energy Materials*, vol. 1, no. 9, pp. 4493–4504, 2018, doi: 10.1021/acsaem.8b00406.

[247] J.-B. Gieu, C. Courrèges, L. El Ouatani, C. Tessier, and H. Martinez, 'Temperature effects on Li 4 Ti 5 O 12 electrode/electrolyte interfaces at the first cycle: A X-ray Photoelectron Spectroscopy and Scanning Auger Microscopy study', *Journal of Power Sources*, vol. 318, pp. 291–301, Jun. 2016, doi: 10.1016/j.jpowsour.2016.04.007.

[248] S. Leroy *et al.*, 'Surface film formation on a graphite electrode in Li-ion batteries: AFM and XPS study', *Surf. Interface Anal.*, vol. 37, no. 10, pp. 773–781, Oct. 2005, doi: 10.1002/sia.2072.

[249] A. Samba, N. Omar, H. Gualous, O. Capron, P. Van Den Bossche, and J. Van Mierlo, 'Impact of tab location on large format lithium-ion pouch cell based on fully coupled tree-dimensional electrochemical-thermal modeling', *Electrochimica Acta*, vol. 147, pp. 319–329, 2014, doi: 10.1016/j.electacta.2014.08.115.

[250] W. Song, M. Chen, F. Bai, S. Lin, Y. Chen, and Z. Feng, 'Non-uniform effect on the thermal and aging performance of Lithium-ion pouch battery', *Applied Thermal Engineering*, vol. 128, pp. 1165–1174, 2018, doi: 10.1016/j.applthermaleng.2017.09.090.

[251] O. Queisser, L. Cloos, F. Boehm, D. Oehler, and T. Wetzel, 'Impact of the Level of Homogenization in 3D Thermal Simulation on the Internal Temperature Distribution of Li-Ion Battery Cells', *Energy Technology*, vol. 2000915, 2021, doi: 10.1002/ente.202000915.

[252] Z. Veszelka, O. Queisser, M. Gontscharow, T. Wetzel, and W. Dörfler, 'Impact of Numerical Methods in Thermal Modeling of Li-Ion Batteries on Temperature Distribution and Computation Time',

Energy Technology, vol. 2000906, 2021, doi: 10.1002/ente.202000906.
[253] ‘Temperiergeräte | °LAUDA’. https://www.lauda.de/de/temperiergeraete (accessed May 14, 2021).
[254] BaSyTec GmbH, ‘products | BaSyTec’. https://basytec.de/products/ (accessed May 14, 2021).
[255] ZAHNER-Elektrik GmbH & CoKG, ‘ZAHNER-Elektrik GmbH & CoKG - Germany • Highend Data Acquisition Systems for Electrochemical Applications | Electrochemical Workstation’. http://zahner.de/products/electrochemical-workstation.html (accessed May 14, 2021).
[256] T. Goosmann, ‘Lin-KK Tool’, Feb. 17, 2021. https://www.iam.kit.edu/et/Lin-KK.php (accessed Jun. 02, 2021).
[257] ‘WT300E Digitale Leistungsmessgeräte | Yokogawa Test & Measurement Corporation’. https://tmi.yokogawa.com/de/solutions/products/power-analyzers/digital-power-meter-wt300e/ (accessed May 14, 2021).
[258] S. J. Harris, D. J. Harris, and C. Li, ‘Failure statistics for commercial lithium ion batteries: A study of 24 pouch cells’, *Journal of Power Sources*, vol. 342, pp. 589–597, Feb. 2017, doi: 10.1016/j.jpowsour.2016.12.083.
[259] R. R. Richardson, M. A. Osborne, and D. A. Howey, ‘Gaussian process regression for forecasting battery state of health’, *Journal of Power Sources*, vol. 357, pp. 209–219, Jul. 2017, doi: 10.1016/j.jpowsour.2017.05.004.
[260] Joint Committee for Guides in Metrology, ‘JCGM 100:2008(E)’. https://www.iso.org/sites/JCGM/GUM/JCGM100/C045315e-html/C045315e.html?csnumber=50461 (accessed Jun. 02, 2021).
[261] W. Bangerth, R. Hartmann, and G. Kanschat, ‘deal.II—A general-purpose object-oriented finite element library’, *ACM Trans. Math. Softw.*, vol. 33, no. 4, p. 24, Aug. 2007, doi: 10.1145/1268776.1268779.
[262] G. Alzetta *et al.*, ‘The deal.II library, Version 9.0’, *Journal of Numerical Mathematics*, vol. 26, no. 4, pp. 173–183, Dec. 2018, doi: 10.1515/jnma-2018-0054.
[263] Käfer Messuhrenfabrik GmbH & Co. KG, ‘Thickness Dial Gauges | analogue - Käfer dial gauges and digital dial gauge instruments in Villingen-Schwenningen’. https://www.kaefer-

messuhren.de/index.php/thickness-dial-gauges-mechanical.html (accessed May 14, 2021).
[264] ‘Mitutoyo, Produkt: Digitale Messuhr ID-H, CEE Netzteil’. https://shop.mitutoyo.de/web/mitutoyo/de_DE/mitutoyo/01.04.04A/Digital%20Messuhr%20ID-H%2C%20CEE%20AC-Adapter/$catalogue/mitutoyoData/PR/543-563D/index.xhtml (accessed May 15, 2021).
[265] EL-Cell GmbH, ‘ECC-Std | EL-CELL’, 2021. https://el-cell.com/products/test-cells/standard-test-cells/ecc-std/ (accessed May 14, 2021).
[266] E.-C. GmbH, ‘User Manual ECC-Std’. 2012.
[267] Y. Cui *et al.*, ‘Recovery Strategy and Mechanism of Aged Lithium Ion Batteries after Shallow Depth of Discharge at Elevated Temperature’, *ACS Applied Materials and Interfaces*, vol. 8, no. 8, pp. 5234–5242, 2016, doi: 10.1021/acsami.5b10474.
[268] M. Weiss, ‘Impedanzgestützte Lebensdaueranalyse von Lithium-Ionen Batterie’, KIT Scientific Publishing, 2019.
[269] L. M. V. G. M. und H. E.-L.-S. 17-37 Wetzlar and 35578 Germany ‘Leica EM TIC 3X Slope Cutting & Cross Sectioning’. https://www.leica-microsystems.com/products/sample-preparation-for-electron-microscopy/p/leica-em-tic-3x/, (accessed May 17, 2021).
[270] Bruker, *Battery Research : Characterizing the Future*. John Wiley & Sons Ltd, 2019.
[271] L. Pfeifer, ‘Entwicklung einer Auswerteroutine für XRD-Daten von Kathodenmaterial aus Lithium-Ionen Zellen’. 2020.
[272] R.-Z. Yin, Y.-S. Kim, S.-J. Shin, I. Jung, J.-S. Kim, and S.-K. Jeong, ‘In Situ XRD Investigation and Thermal Properties of Mg Doped LiCoO $_2$ for Lithium Ion Batteries’, *J. Electrochem. Soc.*, vol. 159, no. 3, pp. A253–A258, 2012, doi: 10.1149/2.006203jes.
[273] R. Robert, C. Bünzli, E. J. Berg, and P. Novák, ‘Activation Mechanism of LiNi 0.80Co0.15Al0.05O2 Surface and Bulk Operando Electrochemical, Differential Electrochemical Mass

Spectrometry and X-ray Diffraction Analysis', *ACS Publications*, vol. Chemistry of Materials, 2014, doi: 10.1021/cm503833b.
[274] J. Hannan, 'Thermo Scientific iCAP 7000 Series ICP-OES: Innovative ICP-OES Optical Design', *Technical Note*, vol. 43153.
[275] J. H. Scofield, 'Hartree-Slater subshell photoionization cross-sections at 1254 and 1487 eV', *Journal of Electron Spectroscopy and Related Phenomena*, vol. 8, pp. 129–137, 1976.
[276] N. Kunkel, 'Bestimmung der Mitteltemperatur in Lithium-Ionen Zellen bei Temperaturgradienten mittels Elektrochemischer Impedanzspektroskopie', Master Thesis, Karlsruhe Institute of Technology, Karlsruhe, 2018.
[277] T. T. Lou, W. G. Zhang, H. Y. Guo, and J. S. Wang, 'The Internal Resistance Characteristics of Lithium-Ion Battery Based on HPPC Method', *Advanced Materials Research*, vol. 455–456, pp. 246–251.
[278] S. Paarmann, L. Cloos, J. Technau, and T. Wetzel, 'Measurement of the Temperature Influence on the Current Distribution in Lithium-Ion Batteries', *Energy Technol.*, p. 2000862, Jan. 2021, doi: 10.1002/ente.202000862.
[279] L. Cloos, 'Einfluss der Temperatur auf die Stromverteilung in Lithium-Ionen Zellen'. 2020.
[280] J. Technau, 'Stromdichteverteilung in Lithium-Ionen Zellen bei angelegtem Temperaturgradienten'. 2019.
[281] A. Fill, T. Mader, T. Schmidt, R. Llorente, and K. P. Birke, 'Measuring Test Bench with Adjustable Thermal Connection of Cells to Their Neighbors and a New Model Approach for Parallel-Connected Cells', *Batteries*, vol. 6, no. 2, p. 16, 2020.
[282] E. Hosseinzadeh, J. Marco, and P. Jennings, 'Combined electrical and electrochemical-thermal model of parallel connected large format pouch cells', *Journal of Energy Storage*, vol. 22, pp. 194–207, Apr. 2019, doi: 10.1016/j.est.2019.02.004.
[283] B. Wu, V. Yufit, M. Marinescu, G. J. Offer, R. F. Martinez-Botas, and N. P. Brandon, 'Coupled thermal-electrochemical modelling of uneven heat generation in lithium-ion battery packs', *Journal of Power Sources*, vol. 243, pp. 544–554, 2013, doi: 10.1016/j.jpowsour.2013.05.164.
[284] S. Goutam *et al.*, 'Three-dimensional electro-thermal model of li-ion pouch cell: Analysis and comparison of cell design factors and model

assumptions', *Applied Thermal Engineering*, vol. 126, pp. 796–808, 2017, doi: 10.1016/j.applthermaleng.2017.07.206.

[285] J. Lv *et al.*, 'Performance of LiFePO4 batteries in parallel based on connection topology', *Applied Energy*, vol. 252, p. 113407, Oct. 2019, doi: 10.1016/j.apenergy.2019.113407.

[286] W. D. Widanage, R. Prosser, S. Paarmann, O. Queisser, and M. Shahjalal, 'Estimation of the Entropy Coefficient of Lithium-Ion Batteries Via a Temperature and Open-Circuit Voltage Kernel Function', in *ECS Meeting Abstracts*, May 2020, vol. MA2020-01, p. 107. doi: 10.1149/MA2020-011107mtgabs.

[287] D. Werner, S. Paarmann, A. Wiebelt, and T. Wetzel, 'Inhomogeneous Temperature Distribution Affecting the Cyclic Aging of Li-ion Cells. Part II: Analysis and Correlation', *Batteries*, 2020.

[288] C. Mavroukakis-Karagounis, I. Papadopoulou, M. Papadopoulou, and C. Makedonas, 'Taking flame tests one step forward: the case of a DIY atomic emission spectrophotometer', *Chemistry Teacher International*, Jul. 2019, doi: 10.1515/cti-2018-0013.

[289] A. Mistry, 'Re: Plating issue', May 08, 2021.

[290] K.-J. Park *et al.*, 'Degradation Mechanism of Ni-Enriched NCA Cathode for Lithium Batteries: Are Microcracks Really Critical?', *ACS Energy Lett.*, vol. 4, no. 6, pp. 1394–1400, Jun. 2019, doi: 10.1021/acsenergylett.9b00733.

[291] H. E. Park, C. H. Hong, and W. Y. Yoon, 'The effect of internal resistance on dendritic growth on lithium metal electrodes in the lithium secondary batteries', *Journal of Power Sources*, vol. 178, no. 2, pp. 765–768, Apr. 2008, doi: 10.1016/j.jpowsour.2007.12.081.

[292] B. S. Parimalam, A. D. MacIntosh, R. Kadam, and B. L. Lucht, 'Decomposition Reactions of Anode Solid Electrolyte Interphase (SEI) Components with LiPF6', *Journal of Physical Chemistry C*, vol. 121, no. 41, pp. 22733–22738, 2017, doi: 10.1021/acs.jpcc.7b08433.

[293] C. Bindra, V. A. Nalimova, D. E. Sklovsky, W. A. Kamitakahara, and J. E. Fischer, 'Statics and dynamics of interlayer interactions in the dense high-pressure graphite compound LiC 2', *Physical Review B*, vol. 57, no. 9, pp. 5182–5190, 1998, doi: 10.1103/PhysRevB.57.5182.

[294] B. Rieger, S. V. Erhard, K. Rumpf, and A. Jossen, 'A New Method to Model the Thickness Change of a Commercial Pouch Cell during

Discharge', *J. Electrochem. Soc.*, vol. 163, no. 8, pp. A1566–A1575, 2016, doi: 10.1149/2.0441608jes.

[295] Y. Zhao, F. B. Spingler, Y. Patel, G. J. Offer, and A. Jossen, 'Localized Swelling Inhomogeneity Detection in Lithium Ion Cells Using Multi-Dimensional Laser Scanning', *Journal of The Electrochemical Society*, vol. 166, no. 2, pp. A27–A34, 2019, doi: 10.1149/2.0011902jes.

Appendix

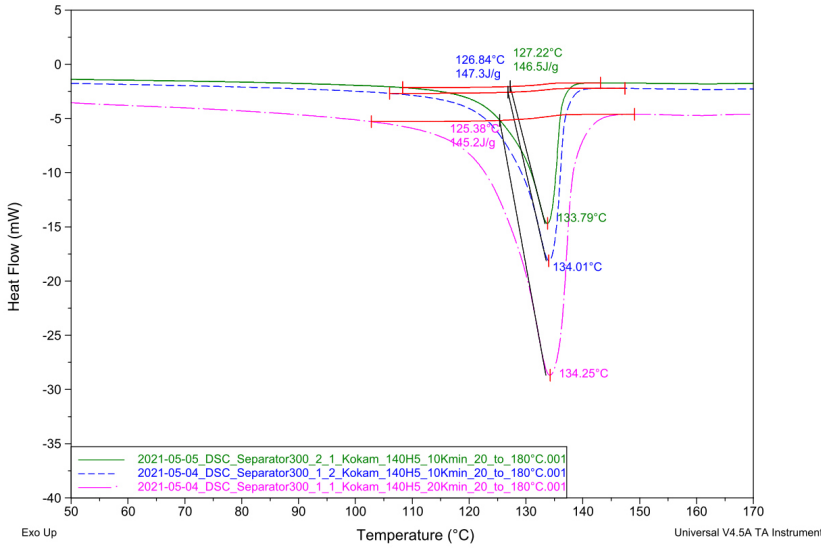

Figure 37.A. Determination of the melting point of the separator via differential scanning calorimetry (DSC).

Current Distribution

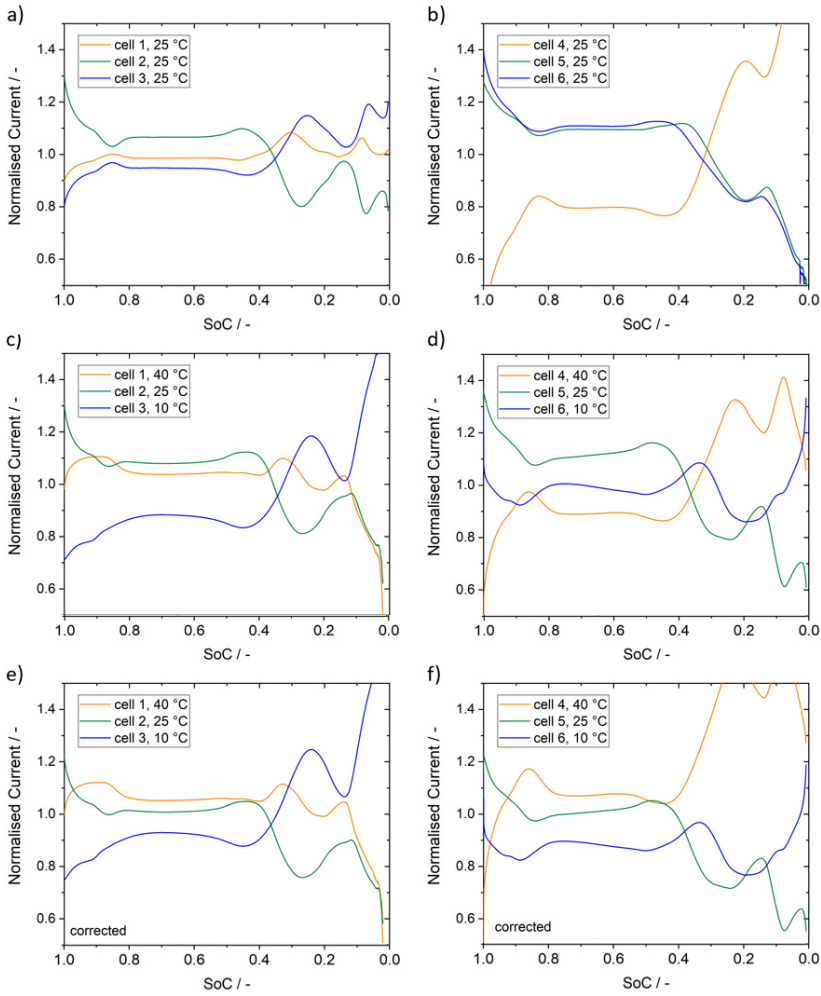

Figure 38.A. Normalised discharge current in the parallel connection at a mean temperature of 25 °C for a)/b) a homogeneous temperature, c)/d) a maximum temperature difference of 40 K, and e)/f) a maximum temperature of 40 K with applied correction for two cell sets. With the correction, the measurement data of the two cell sets are in good agreement, and the influence of cell to cell variations is eliminated.

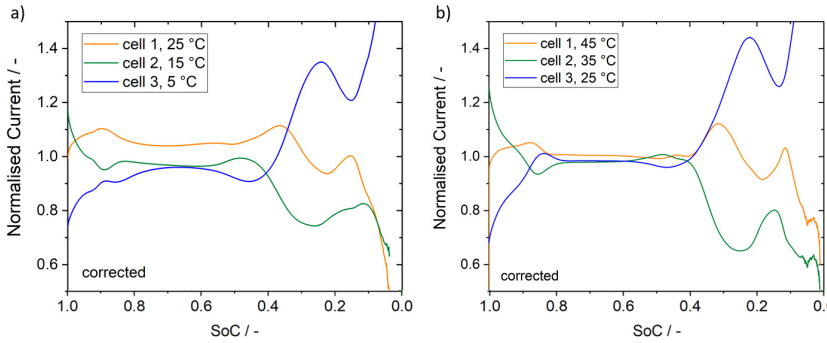

Figure 39.A. Normalised discharge current in the parallel connection at a mean temperature of a) 15 °C and b) 35 °C and a maximum temperature difference of 20 K.

Table 6.A. Coefficients for the exponential equation $\boldsymbol{I_{norm} = a \cdot \exp\left(-\frac{b}{T-c}\right)}$ to adapt the temperature-dependent current distribution at 65 % SoC in Figure 19.

Case during voltage recording	***a* / A**	***b* / K**	***c* / K**
Hom 12.5 °C	1.303	6.975	258.6
Hom 25 °C	1.106	4.786	261.7
Hom 37.5 °C	1.048	4.009	262.2
Inhom 0 °C – 25 °C	1.303	7.872	258.1
Inhom 0 °C – 50 °C	1.15	7.511	255.4
Inhom 12.5 °C – 37.5 °C	1.168	5.781	259.5
Inhom 25 °C – 50 °C	1.063	4.765	260.7
Parallel, Hom 25 °C	1.274	10.47	252.2

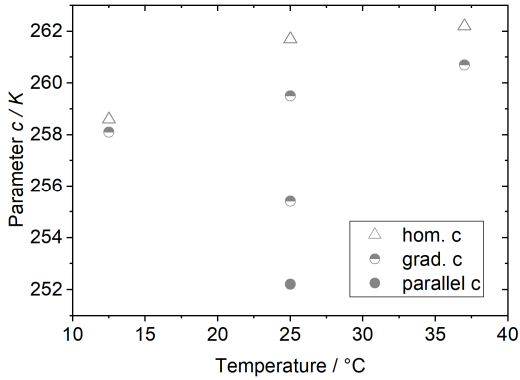

Figure 40.A. Coefficient c of the exponential equation for the temperature-dependent current distribution depending on the average temperature during voltage recording.

Heat generation

$$\dot{Q}(\mathrm{T}) = \left(I_{C/2} \cdot a \cdot \exp\left(-\frac{b}{T-c}\right)\right)^2 \cdot \left(R_{\mathrm{col}} + k \cdot \exp\left(\frac{E_A}{\tilde{R} \cdot T}\right)\right) + \cdots$$
$$I_{C/2} \cdot a \cdot \exp\left(-\frac{b}{T-c}\right) \cdot T \cdot \left(\frac{\partial U_{OCV}}{\partial T}\right)_{50\%}$$

$I_{C/2}$ = 1.5 A; R_{col} = 0.053 mΩ; E_A = 0.5 eV; $\left(\frac{\partial U_{OCV}}{\partial T}\right)_{50\%}$ = 0.173 mV/K

Table 7.A. Coefficients for the temperature-dependent current distribution equation for the different cases during voltage recording at the CC discharge.

Case during voltage recording	a / −	b / K	c / K
2C, Hom 12.5 °C	1.308	6.975	258.6
2C, Hom 25 °C	1.106	4.786	261.7
2C, Hom 37.5 °C	1.048	4.009	262.2
2C, Inhom 0 °C – 25 °C	1.303	7.872	258.1
2C, Inhom 0 °C – 50 °C	1.150	7.511	255.4
2C, Inhom 12.5 °C – 37.5 °C	1.168	5.781	259.5
2C, Inhom 25 °C – 50 °C	1.063	4.765	260.7
3C*, Hom 25 °C	-0.000181	0.13	-21.67

* Polynomial of degree two instead of an exponential equation.

Cyclic Ageing

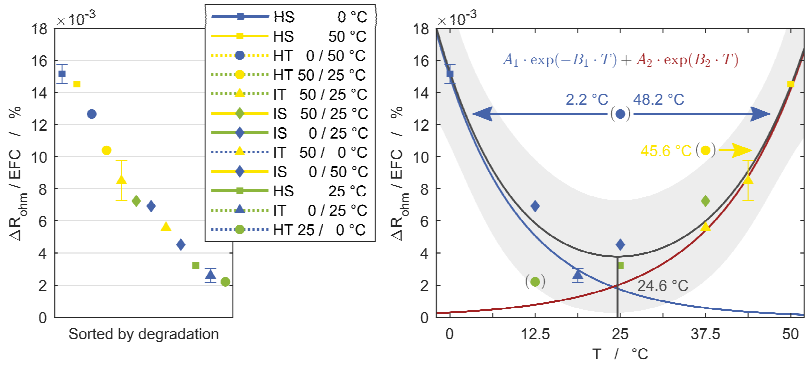

Figure 41.A. a) Experimental set-ups sorted by degradation and b) temperature-dependent ageing function for the increase of the ohmic resistance per EFC composed of two exponential functions [287].

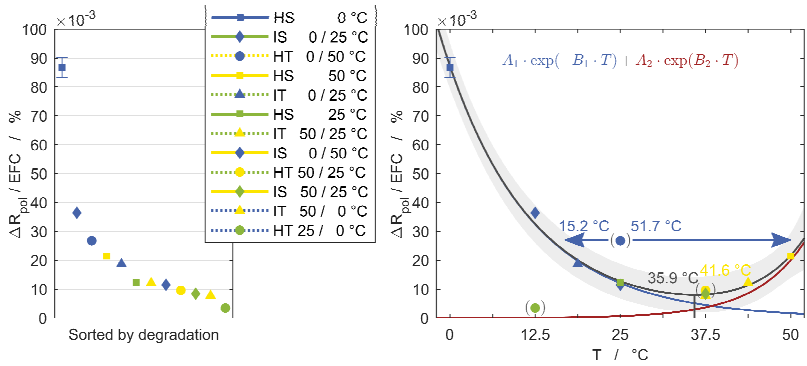

Figure 42.A. a) Experimental set-ups sorted by degradation and b) temperature-dependent ageing function for the increase of the polarisation resistance per EFC composed of two exponential functions [287].

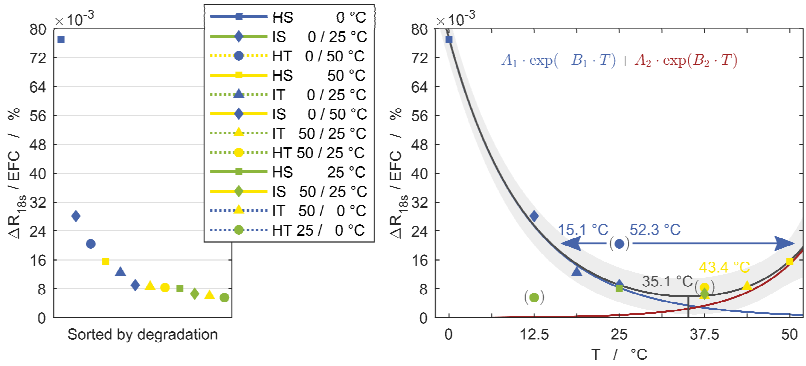

Figure 43.A. a) Experimental set-ups sorted by degradation and b) temperature-dependent ageing function for the pulse resistance per EFC composed of two exponential functions [287].

Fit for the transition from exponential to linear ageing behaviour:

$$\Delta C_{C/20}(EFC) = d \cdot \exp(-e \cdot EFC) + f \cdot EFC + g$$

Thermal Boundary condition	**d / EFC**	**e / T^{-1}**	***f* / T^{-1}**	***g* / EFC**
HS 0 °C	6.011	0.0116	-0.00297	93.99
HS 25 °C	6.298	0.000234	-0.00128	93.21
HS 50 °C	6.112	0.000550	-0.00246	93.14
HT 0/25 °C	4.865	0.00438	-0.0007	95.14
HT 0/50 °C	10.82	0.000920	-0.00297	88.72
HT 25/50 °C	13.32	0.000281	-0.00132	86.33
IS 0/25 °C	5.664	0.00220	-0.00246	92.71
IS 0/50 °C	5.786	0.000553	-0.00137	92.75
IS 25/50 °C	3.505	0.0004325	-0.00155	96.0

Post-mortem

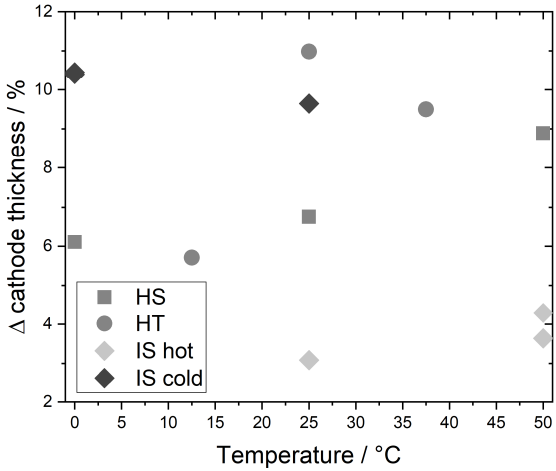

Figure 44.A. Increase of the cathode thickness depending on temperature for the different thermal boundary conditions during cyclic ageing.

Table 8.A. Raw data of the ICP-OES measurements in mg/L in the acidic solution after digestion.

Thermal Boundary condition	Al / mgL^{-1}	Co / mgL^{-1}	Ni / mgL^{-1}	Li / mgL^{-1}	P / mgL^{-1}
HS 0 °C	0.06	0.58	0.31	45.4	5.04
HS 25 °C	0.03	0.61	0.25	48.4	5.08
HS 50 °C	0.36	0.58	0.14	59.4	11.1
HT 0/50 °C .1	0.06	0.63	0.22	58.9	10.7
HT 0/50 °C .2	0.09	0.67	0.23	62.8	11.4
IS 0/50 °C cold	0.07	0.45	0.23	49.5	5.12
IS 0/50 °C hot .1	0.06	0.63	0.22	58.9	10.7
IS 0/50 °C hot .2	0.09	0.67	0.23	62.8	11.4

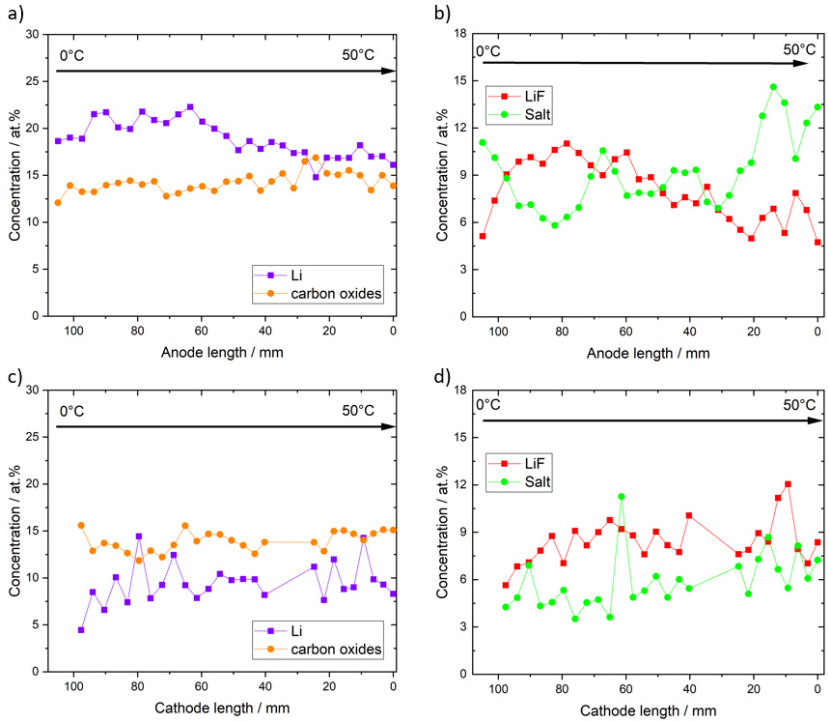

Figure 45.A. Variation of lithium and carbon oxides on the a) anode and c) cathode surface and the variation of LiF and conductive salt on the b) anode and d) cathode surface as a function of temperature measured by XPS.

Table 9.A. Results of XPS for the washed anode with the binding energy of the peak for the respective bonding, the full with at half maximum (FWHM) and the atomic concentration.

Anode washed	Peak Binding Energy / eV	FWHM / eV	at.%
Li1s Scan A	55.8	1.8	23.5
P2p3 POx	133.1	0.7	0.1
P2p3 POxFy	134.7	1.3	0.8

P2p3 LiPF6	136.7	1.0	0.9
S2p3 SOx	168.7	1.3	2.5
C1s sp2	282.5	1.1	0.8
C1s CC/CH	285.2	1.6	17.0
C1s C-O	286.8	1.7	9.1
C1s O-C=O	289.1	1.7	2.9
C1s CO3	290.6	1.5	2.7
O1s LiOH?	530.8	1.5	1.2
O1s Li2CO3/CO2	532.1	1.5	10.3
O1s C-O/POx	533.6	2.1	8.5
F1s Li-F	685.0	1.6	10.8
F1s salt	687.0	2.2	9.0

Table 10.A. Results of XPS for the unwashed anode with the binding energy of the peak for the respective bonding, the full with at half maximum (FWHM) and the atomic concentration.

Anode unwashed	**Peak Binding Energy / eV**	**FWHM / eV**	**at.%**
Li1s Scan A	55.9	1.7	23.1
P2p3 POx	133.4	1.1	0.2
P2p3 POxFy	134.9	1.0	0.7
P2p3 LiPF6	136.9	1.4	2.1
S2p3 SOx	168.8	1.3	2.1
C1s sp2	282.5	0.9	1.0
C1s CC/CH	285.1	1.6	16.8
C1s C-O	286.8	1.8	8.4
C1s O-C=O	289.1	1.7	2.5
C1s CO3	290.5	1.6	2.4
O1s LiOH?	530.7	1.5	0.9
O1s Li2CO3/CO2	532.2	1.6	10.1
O1s C-O/POx	533.7	2.0	6.9
F1s Li-F	685.0	1.5	9.5
F1s salt (PF6-POXFy)	687.0	2.0	13.4

Table 11.A. Results of XPS for the washed cathode with the binding energy of the peak for the respective bonding, the full with at half maximum (FWHM) and the atomic concentration.

Cathode washed	Peak Binding Energy / eV	FWHM / eV	at.%
Li1s lithiated species	56.5	1.4	6.9
Co3p3 A	60.5	3.0	0.1
P2p3 POx	133.5	1.4	0.2
P2p3 POxFy	134.9	0.8	0.3
P2p3 LiPF6	136.9	1.2	0.5
S2p3 S-?	164.1	2.4	0.2
S2p3 Sulfate?	168.8	1.8	1.7
C1s sp2	284.9	1.0	8.2
C1s CC/CH	285.4	1.2	9.1
C1s CH (PVDF)	286.2	1.0	7.8
C1s C-O	287.0	1.6	11.0
C1s O-C=O	288.5	1.5	2.2
C1s CO3	289.7	1.4	2.5
C1s CF2 (PVDF)	290.7	1.0	7.8
C1s CF2-CF2	291.4	1.4	1.7
O1s LiOH/charge?	529.8	1.4	0.4
O1s Li2CO3/CO2	532.8	1.9	8.5
O1s C-O/POx	534.3	2.1	5.7
F1s Li-F	685.5	1.8	4.9
F1s salt (PF6-POXFy)	687.6	1.8	20.3

Table 12.A. Results of XPS for the unwashed cathode with the binding energy of the peak for the respective bonding, the full with at half maximum (FWHM) and the atomic concentration.

Cathode unwashed	Peak Binding Energy / eV	FWHM / eV	at.%
Li1s lithiated species	56.7	1.9	14.9
Co3p3 A	60.5	2.2	0.1
P2p3 POx	133.9	0.5	0.0
P2p3 POxFy	135.3	1.3	0.9
P2p3 LiPF6	137.2	1.4	1.4
S2p3 S-?	164.4	0.5	0.1

S2p3 Sulfate?	169.0	1.4	1.5
C1s sp2	285.1	1.0	8.1
C1s CC/CH	285.7	1.2	5.6
C1s CH (PVDF)	286.2	1.1	5.7
C1s C-O	287.0	1.7	8.1
C1s O-C=O	288.0	1.4	2.1
C1s CO3	289.5	1.7	2.4
C1s CF2 (PVDF)	290.7	1.1	5.7
C1s CF2-CF2	291.6	1.5	1.1
O1s LiOH/charge?	530.1	1.5	0.4
O1s Li2CO3/CO2	532.9	1.9	8.5
O1s C-O/POx	534.4	2.2	6.0
F1s Li-F	685.4	1.6	6.2
F1s salt (PF6-POXFy)	687.5	2.0	21.3

Table 13.A. Results of XPS for the warm part of the anode with the binding energy of the peak for the respective bonding, the full with at half maximum (FWHM) and the atomic concentration.

Anode warm	**Peak Binding Energy / eV**	**FWHM / eV**	**at.%**
Li1s Scan A	55.7	1.5	19.6
P2p3 POx	132.7	1.5	0.3
P2p3 POxFy	134.2	1.5	1.8
P2p3 LiPF6	136.7	1.9	1.1
S2p3 Scan B	163.5	0.6	0.1
S2p3 Scan C	166.8	1.1	0.1
S2p3 Scan A	168.6	1.4	2.3
C1s sp2	282.5	1.6	0.4
C1s CC/CH	285.2	1.6	18.4
C1s C-O	287.0	1.7	10.4
C1s O-C=O	289.2	1.7	3.7
C1s CO3	290.6	1.7	2.6
O1s Li2O	528.7	1.7	0.2
O1s LiOH?	531.1	1.8	3.9
O1s Li2CO3/CO2	532.1	1.6	13.6
O1s C-O/POx	533.6	2.1	9.9
F1s Li-F	685.0	1.6	4.1
F1s salt (PF6-POXFy)	686.9	2.2	7.4

Table 14.A. Results of XPS for the cold part of the anode with the binding energy of the peak for the respective bonding, the full with at half maximum (FWHM) and the atomic concentration.

Anode cold	Peak Binding Energy / eV	FWHM / eV	at.%
Li1s Scan A	55.7	1.7	18.1
P2p3 POx	132.8	1.4	0.3
P2p3 POxFy	134.2	1.5	1.6
P2p3 LiPF6	136.7	1.4	1.3
S2p3 Scan B	163.8	0.7	0.1
S2p3 Scan C	166.7	0.8	0.1
S2p3 Scan A	168.6	1.3	2.3
C1s sp2	282.3	0.6	0.3
C1s CC/CH	285.1	1.7	19.3
C1s C-O	286.9	1.7	10.3
C1s O-C=O	289.2	1.7	4.0
C1s CO3	290.6	1.4	2.1
O1s Li2O	528.7	1.8	0.2
O1s LiOH?	531.0	1.9	2.8
O1s Li2CO3/CO2	532.0	1.7	13.4
O1s C-O/POx	533.6	2.1	9.3
F1s Li-F	685.0	1.7	5.2
F1s salt (PF6-POXFy)	686.9	2.0	9.5

Table 15.A. Results of XPS for the warm part of the cathode with the binding energy of the peak for the respective bonding, the full with at half maximum (FWHM) and the atomic concentration.

Cathode warm	Peak Binding Energy / eV	FWHM / eV	at.%
Li1s lithiated species	55.5	2.1	10.2
Co3p3 A	59.7	1.5	0.1
P2p3 POx	133.6	1.0	1.0
P2p3 POxFy	134.6	0.8	0.8
P2p3 LiPF6	136.1	1.3	0.8
S2p3 S-?	163.5	2.1	0.4
S2p3 Sulfate?	168.0	1.5	1.9
C1s sp2	284.5	1.2	11.3

C1s CC/CH	285.2	1.2	6.3
C1s CH (PVDF)	285.6	1.1	5.1
C1s C-O	286.0	1.2	3.4
C1s C=O	286.8	1.5	9.2
C1s CO2	288.8	1.6	4.6
C1s CF2 (PVDF)	290.1	1.1	5.2
C1s CF2-CF2	290.8	1.0	1.0
O1s LiOH/charge?	529.2	1.5	0.3
O1s C=O/CO2	531.9	1.9	10.9
O1s C-O/POx	533.5	2.2	10.6
F1s Li-F	684.8	1.9	4.4
F1s PVDF-salt	686.9	1.8	12.6

Table 16.A. Results of XPS for the cold part of the cathode with the binding energy of the peak for the respective bonding, the full with at half maximum (FWHM) and the atomic concentration.

Cathode cold	**Peak Binding Energy / eV**	**FWHM / eV**	**at.%**
Li1s lithiated species	55.9	1.9	9.4
Co3p3 A	59.9	3.0	0.1
P2p3 POx	133.0	0.8	0.2
P2p3 POxFy	134.3	1.0	0.8
P2p3 LiPF6	136.2	1.9	0.9
S2p3 S-?	163.6	2.1	0.3
S2p3 Sulfate?	168.2	1.6	1.6
C1s sp2	284.3	1.0	7.7
C1s CC/CH	285.0	1.3	7.0
C1s CH (PVDF)	285.4	1.3	7.9
C1s C-O	286.0	1.3	8.0
C1s C=O	287.0	1.1	4.4
C1s CO2	288.4	1.6	4.0
C1s CF2 (PVDF)	290.1	1.3	7.9
C1s CF2-CF2	291.6	1.1	0.5
O1s LiOH/charge?	529.2	1.8	0.3
O1s C=O/CO2	532.1	1.9	10.1
O1s C-O/POx	533.6	2.2	8.8

F1s Li-F	685.0	1.9	4.5
F1s PVDF-salt	687.0	1.8	15.7

Apparatus and Material

Table 17.A. Specifications of the battery test devices from BaSyTec used in the experiments in this thesis.

BaSyTec	Max. Voltage	Voltage resolution	Max. Current	Current resolution
CTS-LAB	6 V	1 mV	3 A	0.5/1 mA, 50/2.5 µA, 200 nA
XCTS 25A	4.5 V	1 mV	25 A	50 mA

Table 18.A. Devices used for the post-mortem analysis.

Method	Manufacturer	Type
DSC	TA Instruments	DSC Q2000
Ion Beam Milling	Leica Microsystems	Leica EM TIC 3X
ICP-OES	ThermoFisher Scientific	iCAP 7000
REM	ThermoFisher Scientific	FEI Quanta 650
Thickness	Mitutoyo	Digital Indicator ID-H
Weight	Mettler Toledo	XPE206, DeltaRange
XPS	ThermoFisher Scientific	K-alpha spectrometer
XRD	Bruker	D8 Advance

Table 19.A. Materials used during the work for this thesis with purity and supplier.

Material	Purity /Impurity	Supplier
Dimethyl carbonate (DMC)	≥ 99.8 %	Roth
Lithium hexafluorophate (1.0 M $LiPF_6$) in ethylene carbonate (EC) and dimethyl carbonate (DMC), 1:1 (v)	< 15 ppm H_2O < 50 ppm HF	Sigma-Aldrich
Lithium	99.9 %	Sigma-Aldrich
n-Methyl-2-Pyrrolidone (NMP)	≥ 99.8 %	Roth

List of Figures

List of Tables